Detecting Avalanches:

Linking Seasonal Dynamics of Snow-Covered Area to Wet-Snow Avalanche Activity

Master thesis (30 ETCS)

Faculty of Science, University of Bern

handed in by

Flavia Mäder

2020

Supervisors

PD. Dr. Stefan Wunderle

Dr. Alec van Herwijnen

UNIVERSITÄT BERN
OESCHGER CENTRE
CLIMATE CHANGE RESEARCH

SLF

MASTER THESIS

October 2020

Detecting Avalanches

Linking Seasonal Dynamics of Snow-Covered Area to Wet-Snow Avalanche Activity

Author
Flavia Mäder
15-704-893

Supervisors
PD Dr. Stefan Wunderle
Dr. Alec van Herwijnen

"Science never solves a problem without creating ten more."

George Bernard Shaw

UNIVERSITY OF BERN

Abstract

Oeschger Centre for Climate Change Research
Remote Sensing Group, Institute of Geography
WSL-Institute for Snow and Avalanche Research SLF

Master of Climate Sciences with a special qualification in Atmospheric Science

Detecting Avalanches:
Linking Seasonal Dynamics of Snow-Covered Area
to Wet-Snow Avalanche Activity

by Flavia MÄDER

Understanding the dynamics of snow cover parameters in Alpine regions is of great interest. Changes in fractional snow-covered area (fSCA) and snow-water equivalent (SWE) are linked to wet-snow instability and thus to wet-snow avalanche activity. Wet-snow avalanches likely occur in spring, but due to their mostly unknown triggering mechanisms, it is still a challenge to detect the onset of wet-snow avalanche activity cycles (*OWSAAC*) precisely. In this master thesis, we aim contributing to an improvement of snow-cover models by validating the JIM_OSHD (Jules Investigation Model) model with webcam fSCA-data at the Dorfberg site in Davos, Switzerland. For the winter seasons 2015/2016 to 2019/2020 we established a link between fSCA, SWE and wet-snow avalanche activity, and developed a simple model to detect the onset of wet-snow avalanche activity cycles.
Despite the limitations for snow classification in webcam images and resulting data gaps, we showed that webcam fSCA-data, retrieved with three different pixel-intensity based algorithms, could provide an added value to the validation and advancement of the snow cover model JIM_OSHD. The JIM_OSHD model overestimated fSCA especially during early and late winter and reported delayed melt-out dates. Furthermore, the link between JIM_OSHD modelled fSCA, SWE and wet-snow avalanche activity revealed that the *OWSAAC* occurred when fSCA and SWE-data reached their maximum value. To detect this point in time, we trained a simple model with data from the Dorfberg site. We demonstrated that with a percentile range of 0.06% for maximum fSCA and 2.5 to 2.9% for maximum SWE, best quality metrics for detecting the *OWSAAC* were achieved. Although, the false alarm ratio was rather high (62%), the simple model correctly detected the onset for three out of five winter seasons. We suggest to further refine the simple model by including additional parameters that could contribute to a more precise detection of the *OWSAAC*. Together with *OWSAAC*- cascades from lower to higher elevation zones our simple model may assist avalanche forecasters to predict wet-snow avalanche activity.

Acknowledgements

I wish to show my greatest gratitude to my supervisor **Dr. Alec van Herwijnen**, who made it possible to write this thesis at the SLF. He sparked my interest in avalanche research, always had an open ear for my questions, and gave me advice and valuable feedback in no time. Alec tried to make everything possible, from having me in Davos during COVID-19 to now even extending my stay at the avalanche building and prevention group.

Special thanks go also to my advisor **Dr. Stefan Wunderle** from the Remote Sensing Group at the University of Bern. I highly appreciated his kind assistance during my time in Bern, his words of advice, and his confidence in me.

It was a pleasure to work with both of you!

Further I would like to express my deep gratitude to the following people:

- **Céline Portenier**, who kindly introduced me to her snow classification routine, and let me work with it. Furthermore, I want to thank Céline for answering my questions regarding webcam snow classification during the Lockdown, even though she was busy with completing her PhD.
- **Dr. Nora Helbig**, for introducing me to the JIM_OSHD model. Her good inputs and questions made me better understand the complex topic.
- **Stephanie Mayer**, my office mate at the SLF for her valuable inputs, when I was unsure how to proceed, the nice coffee breaks and the laughter in our office. I'm really happy that my stay in B117 is prolonged!
- To my beloved sister **Flurina Mäder**, for her never ending support, encouragement, and the countless hours she has spent helping me sort my thoughts and proof-reading this work!
- **Simon Schudel**, for helping me with QGIS and most importantly for proof-reading this thesis partly during his well-deserved vacation in Iceland.
- **Manuel Meister**, for his efforts to optimise the design of the figures and tables and most importantly for the fantastic cover page layout.
- To my beloved WG flat mates **Sandra, Dodo** and **Simon**. Doing a master thesis during the lockdown was memorable thanks to them and the Apéros on our balcony, cooking nights and ping-pong battles.
- And, of course, to my parents **Babette** and **Jörg Mäder**, for inspiring me to follow my interests and passions. And for supporting me during my studies in Geography in Zurich and Climate Sciences in Bern.

Contents

List of Figures

List of Tables

List of Abbreviations

Acc	**Acc**uracy
ALS	**A**irborne **L**aser **S**canning
AUC	**A**rea **U**nder **C**urve
AVHRR	**A**dvanced **V**ery **H**igh **R**esolution **R**adiometer
DOA	**D**ays **O**f **A**valanches
DN	**D**igital **N**umber
FAR	**F**alse **A**larm **R**atio
FOV	**F**ield **O**f **V**iew
fSCA	fractional **S**now-**C**overed **A**rea
HK	**H**anssen **K**uipers score
HS	**H**eight of **S**now
JIM_OSHD	**J**ules **I**nvestigation **M**odel_**O**perationeller **S**chnee-**H**ydrologischer **D**ienst
LWC	**L**iquid **W**ater **C**ontent
NDSI	**N**ormalized **D**ifferenced **S**now **I**ndex
OWSAAC	**O**nset of **W**et **S**now **A**valanche **A**ctivity **C**ycles
PCA	**P**rincipal **C**omponent **A**nalysis
POD	**P**robability **O**f **D**etection
POFD	**P**robability **O**f **F**alse **D**etection
PRACTISE	**P**hoto **R**ectification **A**nd **C**lassifica**TI**on **S**oftwar**E**
RANSAC	**RAN**dom **SA**mple **C**onsensus
ROC	**R**eceiver **O**perating **C**haracteristic
SCD	**S**now **C**over **D**epletion
SIFT	**S**cale **I**nvariant **F**eature **T**ransform
SLF	WSL-Institut für **S**chnee- und **L**awinen **F**orschung
SURF	**S**peeded-**U**p **R**obust **F**eatures
SWE	**S**now **W**ater **E**quivalent
TLS	**T**errestrial **L**aser **S**canning
UAV	**U**nmanned **A**erial **V**ehicle
VIS	**VI**sible **S**pectroscopy
WSL	Eidgenössische Forschungsanstalt für **W**ald, **S**chnee und **L**andschaft

Chapter 1

Introduction

Monitoring seasonal dynamics of the snow cover in alpine regions is of great interest for scientists, recreationists and the public. Climatologists have shown that the snow cover extent plays a key role in the climate system and is thus an essential climate variable (GCOS, 2020). Furthermore, changes in snow cover affect the biosphere, the hydrosphere and the local economy. A shorter winter season leads to a temporal shift in vegetation growth (Broll et al., 2005), and has an impact on hydrological runoff, water storage and flood issues (Jonas et al., 2009). Since numerous mountain regions depend on winter tourism these changes have negative consequences for the local economy (Rixen et al., 2011).

According to the fourth IPCC Assessment Report (Solomon et al., 2007) the snow cover extent is part of various feedbacks, such as the snow-albedo feedback, that contributes to the global climate sensitivity. Several studies have shown that this feedback is positive (Hall, 2004; Hall et al., 2001; Qu et al., 2007; Thackeray et al., 2016): An increase of surface temperature reduces the extent of snow cover which lowers the global surface albedo. A lower global surface albedo causes an increase in net surface radiation and thereby amplifies the initial surface temperature. As surface temperature is increasing over the past decades, the snow cover extent has decreased, which has significantly changed the earth's energy balance (Hall, 2004). A changing climate may also have impacts on the timing of avalanche activity. For instance, with robust time-series analyses, Pielmeier et al. (2013) showed, that wet-snow avalanche activity has significantly increased during the mid-winter season. This positive trend coincides with the trend of increasing air temperatures in the European Alps, so that adaptions in risk management need to be considered (Pielmeier et al., 2013).

For avalanche research, understanding dynamics in seasonally changing snow cover extent is of great importance. About 50% of the fatalities caused by natural avalanches are due to wet-snow avalanches (Schweizer et al., 2001). In contrast to dry-snow avalanches, the complex triggering mechanisms of wet-snow avalanches have not been studied that well. This is in part due to a lack of observational data and the highly transient wet-snow instabilities that occur within a snowpack (Schweizer et al., 2015, 2003). Not fully understanding the triggering mechanisms makes it difficult to forecast the onset of wet-snow avalanches, e.g. the point in time when many wet-snow avalanches occur for the first time in the season (Baggi et al., 2009; Mitterer et al., 2013). To address this, a number of statistical and physical models have been developed in order to get new insights in wet-snow instabilities.

Baggi et al. (2009), Mitterer et al. (2013), Peitzsch et al. (2012), and Romig et al. (2004) have shown that analysing the liquid water content and the state of the snow cover may be relevant, while air temperature seems to be a rather poor predictor for wet-snow avalanches. For instance, Mitterer et al. (2013) introduced a normalized

Liquid Water Content index (LWC) suggesting that the onset of wet-snow avalanche activity is likely to begin when an average volumetric liquid water content of 3% is reached. They found that the median LWC index increases and coincides well with the onset of wet-snow avalanche activity days, especially when high temperatures and high values of shortwave radiation cause percolation of melt water from the snow surface to the bottom of the snowpack. Also, Wever et al. (2016) argued that a local liquid water content of 5-6% within the snow cover seems to be a reasonable predictor for wet-snow avalanche activity compared to other predictors such as the daily mean air temperature or the daily sum of the positive energy balance. However, defining the end of a period with high wet-snow avalanche activity is still difficult and comes with many uncertainties (Mitterer et al., 2013).

Another promising approach was identified by Helbig et al. (2015b): By using numerical weather prediction data, Helbig et al. (2015b) calculated wet-snow probability maps that are based on a probability density function derived from avalanche occurrence data. Although their model performed well, Helbig et al. (2015b) concluded that the performance of their probability maps could improve, if more information about the snow cover and liquid water content were integrated. Such information can be retrieved from comprehensive numerical snow cover models, for instance from the adapted British Jules Investigation Model JIM_OSHD (Essery et al., 2013a; Magnusson et al., 2015), the French model CROCUS (Brun et al., 1992, 1989) as part of the SAFRAN-SURFEX/IBSA/Crocus-MEPRA model chain (Durand et al., 1999; Lafaysse et al., 2013), or the Swiss snow cover model SNOWPACK (Bartelt et al., 2002; Lehning et al., 2002). Although these models can not yet use numerical weather prediction models to forecast liquid water content, they provide important information about related parameters within the snowpack (Bellaire et al., 2017). These include snow water equivalent (SWE), snow height (HS) and fractional snow-covered area (fSCA) that are related to the liquid water content within the snowpack. Hence, liquid water is present when the snow cover is melting, inducing an increase in SWE, a decrease in HS and thus also a decrease in fSCA. As SWE provides information about future melt water (Wever et al., 2016) and is one of the key parameters describing seasonal dynamics of fSCA (Takala et al., 2011), a decreasing HS stands for compaction and metamorphosis within the snowpack (Bertle, 1966). By relating these parameters, we hypothesize that a coupling of an increase in SWE and a decrease in fSCA thus may act as a precursor for wet-snow avalanche activity.

One of the main challenges in wet-snow avalanche research at present day is to determine the onset of wet-snow avalanche activity cycles. Having reliable information about seasonally changing snow cover and avalanche days, but also parameters related to the snowpack (e.g. SWE and HS), would yield a better understanding of wet-snow avalanches and a more precise detection of the onset of wet-snow avalanche activity cycles. In this study we hypothesize that the onset of wet-snow avalanche activity cycles can be described by deriving a relationship between model retrieved fSCA and SWE. This relation may act as a complement to existing approaches for wet-snow avalanche detection and can assist avalanche forecasters. Furthermore, we argue that webcam retrieved fSCA may act as a useful method for validating existing snow-cover models and products, such as the JIM_OSHD model.

1.1 Research Objectives

This master thesis is comprised of three main parts. First, we determine fSCA on images of a high-resolution webcam facing the *Dorfberg* site in Davos, Switzerland. An image processing workflow, developed by Portenier et al. (2019) is applied to assess seasonal dynamics in fSCA-data. This workflow consists of an automatic snow classification routine with three different snow classification algorithms: We use (i) a blue band algorithm introduced by Salvatori et al. (2011), (ii) a Principle Component Analysis (PCA) algorithm developed by Härer et al. (2013), and (iii) a PCA algorithm with rock thresholding from Härer et al. (2016) as an extension of (ii). Then we analyse and validate the performance of the algorithms (i), (ii), and (iii) for the Dorfberg site

Second, we compare and validate model retrieved fSCA-data with the webcam retrieved fSCA-data. The model retrieved fSCA is based on data provided by the multi-layer model JIM_OSHD that was developed by Essery et al. (2013b) and adapted by Magnusson et al. (2015). Additionally, we compare Unmanned Aerial System retrieved HS-data with JIM_OSHD model retrieved HS-data.

Third, we relate seasonal dynamics in fSCA, SWE and HS from the JIM_OSHD-model to historic wet-snow avalanche activity data from the Dorfberg webcam images. The aim is to thereby identify a tipping point in time when the onset of a wet-snow avalanche activity cycle is most likely to occur. This is extremely relevant as this tipping point can be used for wet-snow avalanche activity forecasting.

Thus, the objectives of this master thesis are the following:

1. To compute the snow-covered area using webcam images from the Dorfberg site with the automatic snow classification workflow proposed by Portenier et al. (2019).
    (a) To analyse the performance of the automatic snow classification workflow by comparing and validating three different snow classification algorithms (i) Salvatori et al. (2011), (ii) Härer et al. (2013), and (iii) Härer et al. (2016).
2. To compare the JIM_OSHD model with snow related parameters.
    (a) To compare fSCA-data derived from the JIM_OSHD model with fSCA-data derived from the webcam images.
    (b) To compare HS-data derived from the JIM_OSHD model with HS-data derived from Unmanned Aerial Vehicles.
3. To link modelled fSCA and SWE-data to avalanche activity and to detect the onset of wet-snow avalanche activity cycles.

With this study, we do not claim to examine the complexity of wet-snow avalanches to its full extent. Entirely understand, model and especially forecast the physical processes responsible for the onset of wet-snow avalanche activity cycles is a demanding task which lies beyond the scope of a master thesis.

Hence, the goal is to improve current snow cover and wet-snow avalanche research by: (1) analysing the performance of different snow classification algorithms for webcam images, (2) comparing webcam retrieved fSCA-data and model retrieved fSCA-data and thus contributing to the validation process of modelled fSCA-data, and (3) discovering and describing links between modelled fSCA-data, SWE-data and the onset of wet-snow avalanches activity.

1.2 Related Work

This chapter provides an introduction to snow models and wet-snow avalanches by taking a closer look at their triggering mechanisms as well as common approaches on the predictability of wet-snow avalanche activity cycles. The second part consists of an overview of the present research of snow cover monitoring, followed by a short examination on frequently used snow classification algorithms for images.

1.2.1 Snow Models

A variety of statistical and physical based snow models exist. Although they are built on similar principles (Magnusson et al., 2015), they can be divided into three different types according to their complexity, computational time, and data requirements: (i) statistical based models, such as temperature-index models used for hydrological and glaciological applications (Huss et al., 2008), (ii) snow-physics models, such as the Swiss SNOWPACK model, used for avalanche forecasting and hydrology (Bartelt et al., 2002; Lehning et al., 2002), and (iii) energy-balance models, such as the Jules Investigation Model (JIM), used for hydrological and land surface applications and weather forecasting (Essery et al., 2013a; Magnusson et al., 2015). In this study we work with data retrieved from the multi-layer energy balance model JIM (Essery et al., 2013a) as it is part of the operational snow and hydrology service of the WSL-Institute for Snow and Avalanche Research SLF (Helbig et al., 2015b; Magnusson et al., 2015).

(i) Statistical based models are used to relate the snowpack energy balance or meteorological conditions to historic wet-snow avalanche events (Romig et al., 2004). These models are used within several studies, i.e. Baggi et al. (2009), Helbig et al. (2015b), Jomelli et al. (2007), Mitterer et al. (2013), Peitzsch et al. (2012), and Wever et al. (2016). Modelling the snow energy balance is a method for regional avalanche forecasting, however, it is computationally costly and is not yet done operationally (Helbig et al., 2015b). Also the thermal state of the snowpack should be considered, as wetting of a previously frozen snowpack can induce instabilities provoking wet-snow avalanching (Armstrong, 1976; Durand et al., 1999; Mitterer et al., 2013; Techel et al., 2009). Mitterer et al. (2013) introduced an index as a combination of air and snow surface temperature to classify avalanche and non-avalanche days. This index performed reasonably, but, as they only considered flat terrain, this approach is less meaningful for mountainous terrain where most avalanches occur.

(ii) The most advanced physical based snowpack models are the French model CROCUS (Brun et al., 1992, 1989) as part of the SAFRAN-SURFEX/IBSA/Crocus-MEPRA model chain (Durand et al., 1999; Lafaysse et al., 2013) and the Swiss snow cover model SNOWPACK (Bartelt et al., 2002; Lehning et al., 2002). Both are used for avalanche warning and operational applications in France and Switzerland.
The one-dimensional physical SNOWPACK model solves the partial differential equations of mass, energy and momentum conservation within the snowpack using a finite-element method. Six numerical procedures are included in SNOWPACK that allow a more accurate and rational description of snow (Bartelt et al., 2002). For investigating wet-snow avalanches the transport and refreezing of melt water in the snowpack are of special interest. This feature is implemented as a one dimensional calculation in SNOWPACK in order to reduce computational effort (Bartelt et al., 2002). However, many problems in snow science are not one-dimensional which is why SNOWPACK and its parameters have been refined in later versions to two and three-dimensions in order to simulate the internal structure of the snowpack in more detail (Bartelt et al.,

2002; Hirashima et al., 2014; Magnusson et al., 2015).
The model SNOWPACK is used for a wide range of purposes: Wever et al. (2015, 2016) investigated whether the occurrence of ponding at layer interfaces inside the snowpack can be related to wet-snow avalanche activity. To do so, they simulated ponding conditions inside the snowpack by complementing the Richards Equation (RE) (Hirashima et al., 2014; Wever et al., 2015) to the SNOWPACK model. With this implementation they found that simulated water accumulations of 5-6% LWC at capillary barriers could be related to wet-snow avalanche activity. Thus, a higher prediction accuracy was achieved with this approach compared to thresholds for daily mean air temperature or the daily sum of the positive snow energy balance (Wever et al., 2016). Furthermore, they showed that the depths of the maximum water accumulation in the simulations correlated with the observed avalanche size.

(iii) Energy balance models play an important role when investigating Alpine regions. These models have high data requirements and are sensitive to complex meteorological processes with strong heterogeneities (Griessinger et al., 2019). To account for that, different approaches exist, e.g. integration of ensembles of meteorological input data (Giorgi, 2006), implementations of bias correction methods (Johnson et al., 2011) or usage of data assimilation (Griessinger et al., 2019). With the application of data assimilation, initial conditions can be estimated by comparing previous model forecasts with newly received observations. Thus, real time observational data, e.g. data of solid precipitation fluxes, are integrated into the modelling process (Kurtz et al., 2017). As Griessinger et al. (2019, 2016) depict in their study, other data types that are assimilated in snow models range from ground-based snow depth and snow-water equivalent measurements (Finger et al., 2015; Jörg-Hess et al., 2015; Magnusson et al., 2015; Slater et al., 2006) to remotely sensed snow-covered area done with microwave radiance (Dechant et al., 2011) over assimilating solid precipitation fluxes. In their work, Griessinger et al. (2019, 2016) have shown the benefits of data assimilation for the JIM framework (Essery et al., 2013a). JIM is an energy balance-based snow melt model which offers three different parametrization options (physical based option, empirical option, and simple option (Magnusson et al., 2015)). These parametrization options are available for seven snow processes to yield optimal snow mass simulations resulting in 1701 possible configurations (Essery et al., 2013a; Magnusson et al., 2015; Moeser et al., 2016). As the JIM model is part of the Operational Snow and Hydrology services of the SLF we refer to it as JIM_OSHD model from now on. Amongst other parameters (Helbig et al., 2018, 2017; Helbig et al., 2015b), it models fSCA, SWE and HS over Switzerland, all of which are used in this study. Verification processes are ongoing (Helbig et al., 2018), which is why webcam retrieved fSCA-data, calculated as part of this work, may contribute significantly to the validation process.

1.2.2 Wet-Snow Avalanches

Avalanches as a type of fast-moving mass movement are a major natural hazard causing natural disasters and occur in most snow-covered mountain regions of the world (Schweizer et al., 2015). A number of avalanche types exist (for more details refer to Schweizer et al. (2015)). In this study we focus on wet-snow avalanches as their prerequisites and triggering mechanisms are still vague and hard to simulate.

Prerequisites and Triggering Mechanisms

Wet-snow avalanches cannot be triggered artificially and release spontaneously, especially in spring. This contrasts with the characteristics of the better known dry-snow avalanches that are likely to be triggered by humans and can be released either artificially or when the snowpack becomes unstable by overloading the weak layers (Schweizer et al., 2001). Considering human-triggered avalanches, Schweizer et al. (2001) analysed that the fatalities caused by wet-snow avalanches are only about 1%. Regarding naturally triggered avalanches, wet-snow avalanches are just as lethal as dry-snow avalanches (Mitterer, 2012; Schweizer et al., 2001). Wet-snow avalanches not only endanger backcountry skiing recreationist athletes, but relevant infrastructure such as roads, railways and communication or electricity lines can also be damaged (Mitterer, 2012).

In their work, Schweizer et al. (2015) summarized the prerequisites and triggering mechanisms for wet-snow avalanche formation: Presence of liquid water (infiltration) favouring loss of strength within the snowpack; a (partially) wet snow cover overloading the snowpack; and a gradual weakening of the snowpack due to warming to 0°C including possible failures of basal layers within the snowpack (Baggi et al., 2009; Fierz et al., 2009; Mitterer et al., 2013; Schweizer et al., 2015). Hence, there should be a decrease in fSCA and HS, and an increase in SWE when wet-snow avalanches are likely to occur. For that, snow depletion curves (SDC) are commonly used to assess the beginning of the melt-season related to snow cover.
Furthermore, Techel et al. (2009) showed that no established procedure exists to assess wet-snow stability as the signs of instability are difficult to foresee. Schweizer et al. (2015) also explained that complex combinations of these mechanisms exist and emphasized the associated uncertainties. These include, the conditions under which liquid water, originating either from rain or melt, is formed. As melt is determined by the energy balance at the snow-air interface, it is crucial to understand the interactions between physical properties of the snow, meteorological influences and site-specific characteristics, i.e. the local topography and related parameters, such as fSCA, SWE and HS.

Wet-snow avalanches generally release when the snow cover extent is reduced, inducing a loss of strength and thus an increase in instability. Hence, by monitoring seasonally changing parameters, such as decreasing fSCA and HS and increasing SWE, this may give valuable information about wet-snow avalanche activity.

Forecasting Wet-Snow Avalanches

The predictability of wet-snow avalanches is still limited since the interaction between liquid water, grain growth, sintering, compaction and loss of strength is highly complex (Bellaire et al., 2017; Mitterer et al., 2014; Mitterer, 2012). Thus, when trying to forecast wet-snow avalanches and their onset, the interaction between these parameters, but also local topography and snowpack layering need to be well understood (Baggi et al., 2009).

There are different approaches to forecast wet-snow avalanche activity: (i) models, including statistical approaches, (ii) indices, and (iii) *in-situ* measurements.

(i) Relying on a physical based snow cover model, Mitterer (2012) modelled the entire energy balance for virtual slopes and calculated the probabilities for avalanche and non-avalanche days. Even though this approach came with good accuracy, modelling

and interpreting the energy balance with regard to forecasting wet-snow avalanches was not always feasible. Additionally, multi-layer models, such as the JIM_OSHD model can provide valuable information about site-specific and seasonally changing parameters (fSCA, SWE and HS) (Magnusson et al., 2015).

(ii) Introducing a liquid water content (LWC) index was another approach proposed by Mitterer et al. (2013). The LWC adequately described the onset and peak of wet-snow avalanche activity. However, with that index it was not possible to accurately determine when the wet-snow avalanche activity period would end and has thus limited validity. In addition to Mitterer et al. (2013), Bellaire et al. (2017) extended the LWC index by including not only measured data from automatic weather stations, but also forecasted data. Also, they adapted the thresholds for the LWC index. With this combination, accumulated errors were removed, and they detected the onset of wet-snow avalanche activity with a probability between 86% and 88% for the winter seasons 2013/2014 to 2015/2016. Still, the LWC approach has limited explanatory power to determine the onset of wet-snow avalanches.

(iii) Based on *in-situ* measurements and observations, Armstrong (1976) and McClung et al. (2006) identified a high correlation between mean daily air temperature and wet-snow avalanche activity. Furthermore, Pielmeier et al. (2013) showed that the number and proportion of wet-snow avalanches in the Alpine mid-winter seasons increased since the late 1980s which coincides with the annual mean temperature anomaly that has increased by 0.04°C per year. In contrast to that, Kattelmann (1985) suggests focussing on the location where water might concentrate within the snowpack and Schweizer et al. (2009) also found that the 3-day sum of precipitation is the strongest forecasting parameter. These studies demonstrate, that depending on the approach and study region, different parameters were considered to be important for detecting and forecasting wet-snow avalanches.

The variety of approaches for forecasting wet-snow avalanche activity shows that a lot of uncertainty and a lack of knowledge exists when it comes to detecting and forecasting wet-snow avalanches, as they are a spatially variable phenomenon.

1.2.3 Monitoring Snow-Covered Area

Common Methods of Snow Cover Monitoring

Approaches to monitor snow cover extent are manifold: Some are based on *in-situ* measurements or models, but remote sensing techniques are also commonly used (Portenier et al., 2019).
In-situ measurements typically consist of point measurements of snow depth. Such measurements are easy to perform, very accurate and well suited for time series and related analyses (Beniston, 2003; Klein et al., 2016; Laternser et al., 2003; Marty, 2008; Scherrer et al., 2004). However, as the spatial scale of *in-situ* measurements is limited, the spatial variability of the snow cover extent is not captured (Portenier et al., 2019).

Furthermore, *in-situ* measurements can complement other techniques, such as laser scanning methods, e.g. Airborne Laser Scanning (ALS) and Terrestrial Laser Scanning (TLS). Also, the point measurements may help validating models and modelled parameters such as fSCA, SWE and HS. However, retrieving measurements in field is time-consuming, costly, and limited in spatial coverage. To add to these downsides,

there is also a bias towards accessibility, larger avalanches, and clear sky conditions where no fog or clouds occur (Herwijnen et al., 2013b; Portenier et al., 2019).

Monitoring snow cover with remote sensing techniques has been done since the beginning of the satellite era in the 1960s. Remote sensing products, such as snow cover maps calculated by Normalized Snow Difference Indices (NDSI) have been established to complement snow cover models (e.g. SNOWPACK, JIM_OSHD) and *in-situ* measurements.
Due to their regular revisit time, satellites provide comprehensive surface information, even in less accessible areas (Hüsler et al., 2012). On a global scale, data from the Advanced Very High Resolution Radiometer (AVHRR) sensor is often used to study snow cover variability and study long-term dynamics in snow cover climatology (Derksen et al., 2000; Foppa et al., 2004; Hüsler et al., 2014; Solberg et al., 2012). On a regional scale, satellite images from National Aeronautics and Space Administration (NASA) and National Oceanic and Atmospheric Administration (NOAA) are used to monitor the snow cover on a daily basis (Cianfarra et al., 2009; Salvatori et al., 2011; Spisni et al., 2011). However, satellite remote sensing products have some limiting factors, such as cloud and fog coverage, contamination, and spatial heterogeneity (Hüsler et al., 2014; Portenier et al., 2019). Hüsler et al. (2014) summarizes several methods to address the issue of cloud coverage, for instance the usage of spatial and temporal cloud gap filling techniques (Hüsler et al., 2014; Parajka et al., 2010), maximum snow cover composites or information from similar sensors (Hall et al., 2019; Parajka et al., 2008). Although, these methods may be helpful to address cloud contamination, snow cover information can become inaccurate and blurred (Hüsler et al., 2014).

Monitoring Fractional Snow-Covered Area with Time-Lapse Photography

An alternative method to monitor the spatial extent of snow-covered area comes with terrestrial time-lapse photography obtained by webcams in Alpine regions. Time-lapse images can be combined with data from models, indices, and *in-situ* measurements (Herwijnen et al., 2013a; Herwijnen et al., 2013b, 2012). Webcams usually view the hillside from below, which is why cloud cover is less of a problem as with satellite based remote sensing. Therefore, time-lapse photography retrieved from webcams is a simple, non-invasive and inexpensive alternative with high temporal and spatial resolution to observe the spatial extent of snow cover over a small area of interest (Aschenwald et al., 2001; Herwijnen et al., 2012). Though the restriction to a small region can be a disadvantage, the high spatial resolution within the webcam-field of view (FOV) as well as the high temporal continuity are a clear advantage of the time-lapse photography compared to satellite remote sensing products (Härer et al., 2016).

Several studies investigated the variability in land cover with time-lapse photography and webcam imagery. In fact, time-lapse photography has been used in cold regions to examine gradually evolving inter- and intra-annual processes of glaciers, ice sheets and snow cover variability (Ahn et al., 2010; Harrison et al., 1992; Hinkler et al., 2002). For instance, this technique has been used to investigate snow cover on different vegetation types (Kepski et al., 2017) in order to automate snow depth measurements (Hedrick et al., 2014). Also, avalanche activity can be investigated with time-lapse photography, especially when it is combined with additional data: Feick et al. (2012) and Herwijnen et al. (2013b, 2012) examined the release of glide snow avalanches and

glide-crack evolution using a combination of time-lapse photography of a hill slope and seismic data of the same area. Time-lapse photography has also been used to investigate the release of wet-snow avalanches by correlating avalanche occurrences with local meteorological data at the Dorfberg and Wannengrat in Davos, Switzerland (Helbig et al., 2015b; Herwijnen et al., 2013b).

These examples illustrate that a combination of time-lapse photography products and additional data is a common and promising method that contributes to a better understanding of the processes involved.

1.2.4 Monitoring Parameters related to Snow-Covered Area

In the past, the assessment of the snow cover stability has been done with single snow profiles giving only limited information on the snow cover of a slope or a region. Recently, ultrasonic (Avanzi et al., 2017) or laser depth sensors (Morin et al., 2012) have been used for monitoring HS. SWE on the other hand can be monitored by using snow pillows (Johnson et al., 2011) or cosmic rays (Morin et al., 2012). However, when it comes to the spatial variability of snow processes, the significance of local measurements has been controversially discussed (Grünewald et al., 2015; Helbig et al., 2017). Non-invasive remote sensing techniques, such as TLS (Grünewald et al., 2015; Jörg-Hess et al., 2015), digital photogrammetry (Bühler et al., 2015), ground penetrating radar (Machguth et al., 2006), time-lapse photography (Farinotti et al., 2010; Parajka et al., 2012) or satellite-based products (Dietz et al., 2012) are considered to be a possible solution to overcome the under-representation of point measurements for the parameters SWE and HS. Since the late 1990s simulated snow profiles have been established and further developed to operational snow cover models (Section 1.2.1) (Durand et al., 1999).
Models are an essential tool for forecasting and simulating changes in parameters related to snow cover stability, such as fSCA, SWE and HS (Helbig et al., 2018; Helbig et al., 2015b). Combining modelled fSCA-data with SWE-data, which describes the amount of water that would result from the complete melt of snow (in mm or kg/m^2), and HS, which depicts the snow height in meters m, may give some indication about wet-snow avalanche activity. These parameters are typically modelled with operational models such as the SNOWPACK or JIM_OSHD model (Essery et al., 2013a; Magnusson et al., 2015).

1.3 Snow Classification of Optical Images

With its brightness and white colour, the snow cover shows distinct spectral properties compared to other land cover types (Hinkler et al., 2002). Therefore commonly used snow classification algorithms make use of the large differences between snow (high reflectance) and other surfaces (lower reflectance) in the visible part of the electromagnetic spectrum (VIS). This characteristic allows to distinguish between snow, vegetation and bare soil surfaces, which is typically done by applying a pixel brightness intensity threshold value.

Various approaches and algorithms exist for the snow classification of optical images. Dozier (1989) developed a Normalized Difference Snow Index (NDSI) based on red, green and blue (RGB) values to derive snow cover maps from satellite products, e.g. Landsat Terrestrial Mapper (Landsat TM) data. Nowadays, this is a standard

method and widely applied (Hall et al., 2001; Hinkler et al., 2002). Other promising approaches include setting criteria and thresholds (Salvatori et al., 2011), statistical analysis (Härer et al., 2013, 2016), supervised and unsupervised classifications (Kepski et al., 2017), or spectral mixture techniques (Salzano et al., 2019). Recently, machine learning algorithms have been trained for image classification (Das, 2017; Hao et al., 2018). However, they require much user input data, are computationally intensive or need the interpreter's expertise (Hall et al., 2001).

In this study we use the snow classification algorithms of Salvatori et al. (2011) based on a threshold setting in the blue band, and the algorithms of (Härer et al., 2013, 2016) where the statistical technique of PCA is applied. These algorithms are simple and computationally efficient, which is a clear advantage when working with large data sets, such as processing time-lapse images of webcams. Salvatori et al. (2011) evaluated the performance of the algorithm by testing the classification method in the Italian Alps and Apennines, where only 1% of the investigated pixels were misinterpreted (Salvatori et al., 2011). In PRACTISE V.1.0. (Photo Rectification And ClassificaTIon SoftwarE) Härer et al. (2013) applied the statistical method of Principal Component Analysis (PCA) to differentiate snow-covered pixels from snow free pixels. In PRACTISE V.2.1. Härer et al. (2016) evolved their approach further by separating the snow cover from sunlit rock surfaces. Both PRACTISE V.1.0 and V.2.1. were tested on the Schneefernerkopf at the Zugspitze in Germany and showed misclassifications of less than 1% of the investigated pixels. The choice of an adequate algorithm for snow classification in optical images is not trivial. For that, validation procedures are necessary in order to compare different snow classification algorithms with ground truth data for specific sites.

After applying a snow classification algorithm, the main challenge is to georectify arbitrary 2D-photographs (e.g. time-lapse photography from webcams) into real world 3D-spaces, when processing a map of spatial snow cover extent. This challenge can be overcome, for instance, by applying the approach of Aschenwald et al. (2001) and Corripio (2004). They had the idea to project a camera image on a 3D-DEM plane for deriving georeferenced maps. While Aschenwald et al. (2001) used ground control points (GCPs) to georectify the orthophoto, Corripio (2004) used an animation and rendering technique established by Watt et al. (1992) where 13 camera parameters had to be set as an input. The newest version of PRACTISE V.2.1. includes a viewshed computation in order to identify the camera location and orientation faster and simpler than before Härer et al. (2016).

1.4 Summary

Wet-snow avalanches are dangerous and difficult to forecast. Although, some progress has been made with respect to understanding basic principles of the processes involved (e.g. loss of strength due to water infiltration and storage at capillary boundary, overlay of wet and weak layers, isothermal warming to 0°C (Baggi et al., 2009)), forecasting wet-snow avalanches and in particular the onset of wet-snow avalanche activity cycles in spring remains challenging.

Thus far, either statistics based snow cover models (e.g. snow energy balance, thermal state of the snowpack (Jomelli et al., 2007; Romig et al., 2004; Wever et al., 2016)), or physical based models (e.g. SNOWPACK, LWC (Bartelt et al., 2002; Lehning

et al., 2002; Mitterer et al., 2013)) have been used to forecast wet-snow avalanches and related parameters. However, since it is known that wet-snow avalanches occur when the snow melts, e.g. when liquid water is present, we hypothesize that wet-snow avalanches can also be detected and forecasted by relating site-specific modelled fSCA, SWE and HS data. This would allow using snow cover models (e.g. JIM_OSHD), that are validated with snow classified webcam images, for wet-snow avalanche prediction.

Chapter 2

Data

2.1 Study Area

In this study we used webcam images of the Dorfberg site located in Davos, Switzerland (Figure 2.1a). The Dorfberg site is a south east facing slope where glide-snow and especially wet-snow avalanches are likely to occur. Due to its vicinity to the SLF, the Dorfberg site has been observed since many years. For instance, Feick et al. (2012), Herwijnen et al. (2012), and Mitterer et al. (2013) started to observe the area using time-lapse photography in 2008. In this study we investigated the winter seasons 2015/2016 to 2019/2020 each from October to June. In order to detect seasonally changing fSCA at the Dorfberg site, a webcam, installed on the third floor of the SLF building about 7 m above ground (coordinates: 2 783 801, 1 187 379, 1560 m a.s.l) was used. It is henceforth referred to as *Dorfberg webcam*. All coordinates in this study are given in the coordinate system CH1903+ LV95. Since 2008 the webcam with a single viewing angle (upward looking) has been monitoring the entire slope of the Dorfberg site which yields in an investigated area of about 2.02 km^2. An overview of the field of view (FOV) is shown in Figure 2.1b. The altitude of the Dorfberg site varies between 1580 m a.s.l. at the physical-meteorological World radiation centre (PMOD/WRC) situated at the lower left of the FOV, up to an altitude of 2536 m a.s.l. at the Salezer Horn. The mean altitude of the Dorfberg site is around 2030 m a.s.l. which is slightly above the alpine tree line.

(A) Location and mapped FOV of the Dorfberg webcam installed at the SLF in Davos, Switzerland. *Map source: geo.admin.ch (2020)*.

(B) Webcam image taken on 18 February 2017 at noon (12 PM).

FIGURE 2.1: Overview of the Dorfberg site and webcam in Davos, Switzerland.

Until the winter season of 2017/2018 the camera was a Nikon Coolpix E5900. From 2018/2019 a Canon EOS 400D DIGITAL was used. The received images, stored with an automatic system, have a resolution of 2592 x 1944 pixels (5.1 Megapixel) for the

Nikon camera, and 3888 x 2592 pixels (10.1 Megapixel) for the Canon camera. Both cameras take images at 24-bit colour depth and in file format JPG. This provides us a quasi-continuous time series for the past five years at the Dorfberg site.

Furthermore, we investigated the Dischma valley which is south-east directed and close to Davos Dorf. In this study we examined the end of the valley, starting from Duerrboden (2004 m a.s.l.) up to the south-east situated Scalettahorn (3067 m a.s.l.) (Figure 2.3). At Duerrboden (2004 m a.s.l.), the SLF installed webcams with six camera viewing angles. These cameras are facing the surrounding hill slopes and are monitoring the avalanche activity since 2015.

2.2 Digital Elevation Model

The georectification process of the snow classified webcam images requires a digital elevation model (DEM). In this study we used the precise DEM *swissALTI3D*, provided by the Swiss Federal Office of Topography (swisstopo, 2018). SwissALTI3D has a spatial resolution of 2x2 m and is in fact a digital terrain model as it describes the surface of Switzerland without any vegetation or buildings. Information is updated every six years and given for every coordinate. Below an elevation of 2000 m a.s.l., the altitude information originates from airborne laser scanning LiDAR data with an accuracy of ±0.5 m, while for elevations above 2000 m a.s.l., high resolution aerial photographs are used, resulting in a lower accuracy of ±1 – 3 m (swisstopo, 2018). swissALTI3D is offered in GEOTIF, ESRI ASCII Grid and ASCII X, Y, Z single space file formats. In this study, we used ASCII X, Y, Z single space, identical to Dizerens (2015).

2.3 Model retrieved fSCA, SWE and HS

In this study we worked with snow melt simulations from the Jules Investigation Model (JIM) (Essery et al., 2013a) for the Dorfberg and Dischma area. As a multi-model frame, JIM uses 1701 process representations combinations (Griessinger et al., 2019) that are based on energy-balance models (Essery et al., 2013a). To find optimal combinations for the process of obtaining daily snow mass and snowpack runoff, different parametrizations are chosen. JIM includes snow albedo parametrization, empirical snow compaction parametrization, turbulent heat exchange, drainage of melt water, fresh snow density parametrization and thermal conductivity parametrization amongst others (Griessinger et al., 2019). For further details we refer to Essery et al. (2013a), Griessinger et al. (2019), Helbig et al. (2015a), and Magnusson et al. (2015). JIM was extended by Helbig et al. (2018, 2015a) with a subgrid-parametrization for fractional snow-covered area focusing on complex topography. In their study, Helbig et al. (2015a) suggest including the standard deviation of snow depth. With this, JIM was modified for the Operational Snow and Hydrology Service (OSHD) of the SLF and referred to it as JIM_OSHD model.

Since 2015 the JIM_OSHD model generates output files for the parameters fSCA, SWE and HS on a daily basis. Each grid cell has a spatial resolution of 1 km^2. For the years 2015 to 2019 the JIM_OSHD model covers Switzerland with 359 x 248 pixels, with a grid origin located in Chambéry (France) at coordinates 2 479 500 / 1 052 500. As the extent of the model was recently increased, the output file is now available for 365 x 272 pixels, originating at coordinates 2 473 500 / 1 052 500 for winter 2019/2020.

TABLE 2.1: JIM_OSHD tiles for the Dorfberg webcam with their mean altitudes and coordinates for orientation.

JIM_OSHD Tile	Mean Altitude [m a.s.l.]	Coordinates (CH1903+/LV95) (lower left of the tile as origin)
p6	2469	2 781 500 / 1 188 500
p7	2074	2 782 500 / 1 188 500
p11	2176	2 781 500 / 1 187 500
p12	1772	2 782 500 / 1 187 500
p13	1558	2 783 500 / 1 187 500

We extracted JIM_OSHD outputs for the investigated areas, resulting in 20 tiles for the Dorfberg site (Figure 2.2), and 36 tiles for the Dischma valley (Figure 2.3). The Dorfberg webcam is located in tile p18 and the viewing angle of the camera includes the tiles p6, p7, p11, p12, and p13. Figure 2.2 gives an overview of the mapped tiles at the Dorfberg site and in Table 2.1 the coordinates and mean altitude of each tile are given. For every tile at the Dorfberg site and Dischma valley we obtained fSCA [0, 1], SWE [mm], and HS [m] for the months October to July during the winter seasons 2015/2016 to 2019/2020.

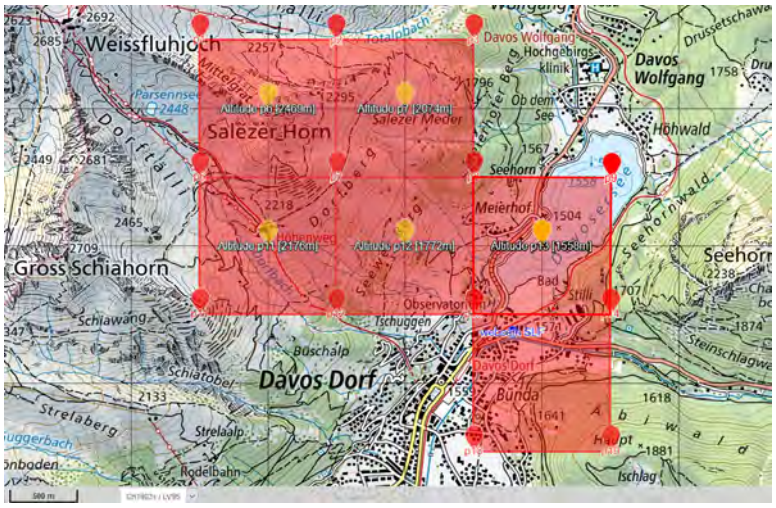

FIGURE 2.2: JIM_OSHD tiles p6, p7, p11, p12, p13 and p18 covering the field of view of the Dorfberg webcam, installed at the SLF in Davos, Switzerland. *Map source: geo.admin.ch (2020).*

2.4 UAV Snow Height

For comparing and evaluating the performance of the JIM_OSHD modelled HS, we used HS data from an Unmanned Aerial Vehicle (UAV) of type eBee+ RTK of SenseFly (Eberhard et al., 2020). These data have a spatial resolution of 0.03 m / pixel for the Dischma area, and were collected on 7 April 2018. Figure 2.3 shows a map of the Dischma area and the area covered by eBee+ of about 3.59 km^2. The data from the

UAV is part of a comprehensive study of Eberhard et al. (2020) analysing different photogrammetric techniques for snow depth mapping.

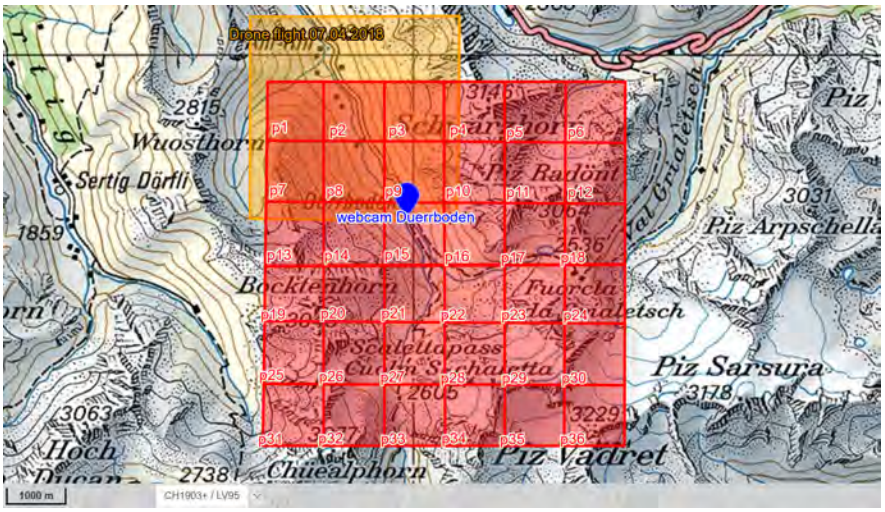

FIGURE 2.3: UAV HS-data from 7 April 2018 covering the Dischma area (orange area). JIM_OSHD tiles (red area) p1 to p36 covering the field of view of the Duerrboden webcam (blue marker) installed in the Dischma valley, Switzerland. JIM_OSHD tiles p1, p2, p3, p7, and p8 are analysed to compare UAV HS-data with JIM_OSHD HS-data. *Map source: geo.admin.ch (2020).*

2.5 Avalanches

The avalanche activity of the Dorfberg has been monitored since 2009. Due to its vicinity to the SLF-institute it is a well-examined site. All avalanches were mapped from webcam images into a GIS system by hand. This was done by using the monoplotting tool developed by Bozzini et al. (2012), which has made the spatial georeferencing of oblique images more approachable. The finalized data set consists of the avalanches seen on the Dorfberg webcam and includes many variables of which we considered the following: *release date, release time, altitude, coordinates of the starting zone,* and the *avalanche type*. For the purpose of this study, we considered all wet-snow avalanches and excluded wet-loose snow avalanches.

In the Dischma valley we also used webcam images from six viewing angles for monitoring the avalanche activity starting in winter season 2015/2016. The images with avalanches were flagged, thus we related the avalanche activity and the onset of wet-snow avalanche activity cycles to the corresponding hill slopes and dates.

Chapter 3

Methods

In this Chapter, we give an overview on the workflow routine for webcam image snow classification and fSCA-data retrieval (Section 3.1, blue box in Figure 3.1). Then, in Section 3.2 we show how we evaluated the validation of the snow classification algorithms (green box in Figure 3.1). In Section 3.3 we compare HS with UAV data (red box in Figure 3.1) and in Section 3.4 (yellow box in Figure 3.1) we define the true onset of wet-snow avalanche activity cycles. We finish this chapter by presenting a simple model to detect the onset of wet-snow avalanche activity cycles (Section 3.5, green box in Figure 3.1). To facilitate the understanding of the workflow, a simplified flowchart is shown in Figure 3.1. An enlarged version of the flowchart, including a detailed description of the processes involved, is shown in Figure A.1 in the Appendix.

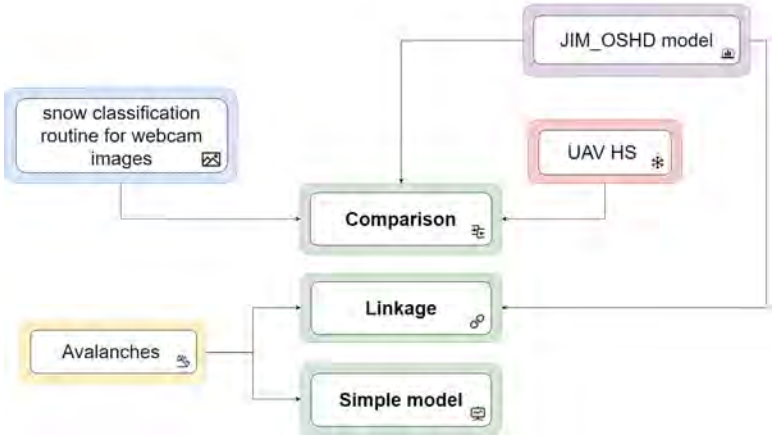

FIGURE 3.1: Flowchart of the working process used in this study. The green boxes refer to the research questions whereas the blue, purple, yellow and red boxes refer to the different Sections in Chapter 3. An enlarged and detailed version is shown in the Appendix (Figure A.1).

3.1 Snow Classification Routine

The aim of an automatic snow cover classification workflow is to identify the snow cover extent shown in a webcam image or any other image, with limited human intervention (Salvatori et al., 2011). Portenier et al. (2019) developed a semi-automatic procedure implemented in Matlab to derive snow maps from publicly available webcam images. For this study we applied, adapted and complemented these procedures for an optimal fSCA-data retrieval for the Dorfberg site.

3.1.1 Input Preparation

Master Image

Choosing an adequate master image that is representative for the investigated site (e.g. a hill slope) is crucial for further processing. At the recommendation of Portenier et al. (2019) we selected a master image at a day with medium to high fSCA (>50%), clear sky conditions to enhance contrast, and a high solar zenith angle to minimize shadows. For the Dorfberg site, we chose an image taken at 8 November 2013, 9 AM, henceforth called *master image* (Figure 3.2a).

(A) (B) (C)

FIGURE 3.2: Master image taken on 8 November 2013 at 9 AM (A). The silhouette is defined by a Sobel edge detection process (B) with a threshold of 0.02 and shown with a red line in (C).

3.1.2 Pre-processing of the Master Image

Based on Portenier et al. (2019) we pre-processed the master image to obtain both the mountain silhouette and the DEM-based viewshed at the end of this step. A Gaussian filter is applied to reduce noise within the image in order to extract the mountain silhouette. This is done by using a Sobel edge detection algorithm, which allows for the detection of distinctive structural features within the master image (Figure 3.2b). Depending on the illumination in the master image, the default edge threshold of 0.02 may need to be adapted. For the Dorfberg images however, it was left unchanged. After the successful derivation of the mountain silhouette (Figure 3.2c), or in other words the horizon, a binary *silhouetteMask* is generated in order to mask out the sky (Figure 3.3b). Since the workflow of Portenier et al. (2019) was unmodified for this part of the procedure, we refer to their study for further details (Dizerens, 2015; Portenier et al., 2019).

Input Mask

The purpose of an input mask is to exclude regions for the snow classification. These regions are composed of artefacts, such as obstacles (roads, buildings, electricity pylons), prominent trees and forest in the vicinity of the camera position. Also, the area close to the camera was masked out. In this case, the input mask for the master image was drawn by hand (Figure 3.3b) and then saved as a 1bit binary image for further processing.

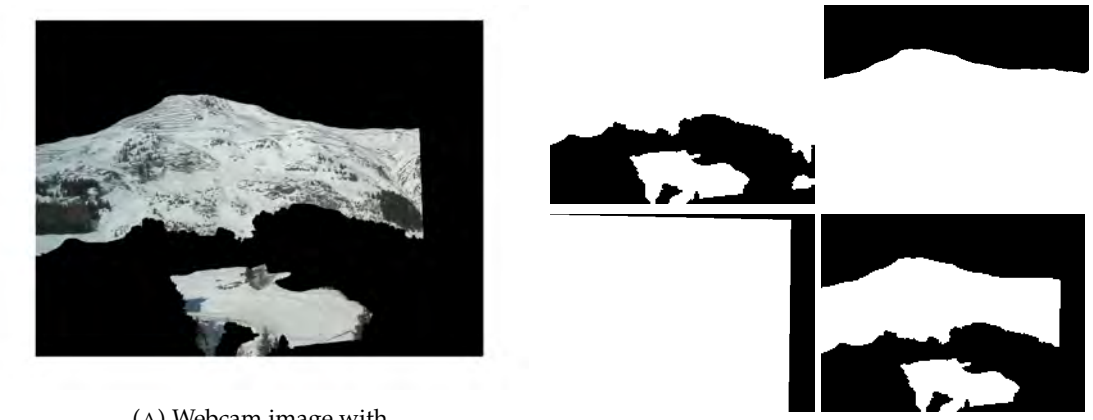

(A) Webcam image with superimposed masks.

(B) In clockwise direction: Input mask, silhouette mask, alignment mask final mask.

FIGURE 3.3: After aligning the webcam image the final mask (B), containing the input mask, silhouette mask, and alignment mask, is superimposed on every webcam image (A) to define the FOV.

3.1.3 Daily Composites of Webcam Images

Preliminary studies (Fedorov et al., 2015; Kepski et al., 2017; Portenier et al., 2019) have shown that most image classification routines perform best during optimal weather and lighting conditions. These conditions are best met if an image is taken on a sunny day, with high contrast and no clouds or fog making the mountain silhouette easy to detect. But even good weather images may suffer from illumination issues, such as shadows originating from neighbouring mountains, obstacles, as well as trees. In order to address these drawbacks, different approaches exist. For instance, Bernard et al. (2013) acquired three images at fixed hours every day and Kepski et al. (2017) worked with webcam images that have been taken between 10 AM and 11 AM. Still, Bernard et al. (2013) and Kepski et al. (2017) had to disregard many of these images, as these were unusable or missing. Alternatively, Dizerens (2015) suggests utilising another colour space (e.g. YUV), increase brightness or apply automatic tone adjustments.

In this study, we use the technique of image compositions. This technique is another simple but effective strategy, that is also used by Fedorov et al. (2015). Image compositions consist of a number of separate images, aggregated into one single image. As fSCA changes only slowly with time, having one image per day is sufficiently accurate and representative when analysing seasonal dynamics of fSCA (Fedorov et al.,

2015). Additionally, reducing the amount of images accelerates the computationally intensive snow classification procedure.

For automation of the image composite retrieval at the Dorfberg site, we first defined the time span in which the images are to be transformed into composites. For the Dorfberg webcam, we decided to neglect the earliest and latest image of the day. The reason for this lies with the low illumination particularly at dawn, which could negatively influence the composition and cause possible snow misclassifications. Hence, each composited image of the Dorfberg camera consists of about eight separate images taken every full hour from 9 AM to 4 PM. Second, we applied the MATLAB-functions "blend" and "join", resulting in a blended overlay image, where the intensities of the input images are scaled jointly and averaged in a single data set. Finally, the composited image was stored in a separate folder for further processing.

FIGURE 3.4: Eight hourly images taken between 9 AM and 4 PM on 2 February 2016 for the Dorfberg site.

FIGURE 3.5: Composited image of the images shown in Figure 3.4.

For illustration, a composited image is shown in Figure 3.4. Eight hourly images of the Dorfberg on 2 February 2016, starting at 9 AM until 4 PM, were merged into one composited image shown in Figure 3.5. In the single images we see changing illumination conditions due to the changing solar angle over the day. These effects are weakened or even eradicated in the composited image shown in Figure 3.5.

3.1.4 Image-to-Image Alignment

Over the years many webcam installations show can distortions in orientation through shaking or reorientation, leading to different fields of view (FOV). In order to address that, each webcam image needs to be aligned and reoriented to its predefined master

image. This is crucial because fSCA-data is defined as a relative measure with a number between 0 and 1, requiring a constant FOV over time. Also, the alignment procedure allows us to reduce computational effort as the same image-to-DEM transformation matrix is used for every webcam image. For the image-to-image alignment process various methods exist. For instance, Fedorov et al. (2015) applied a cross-correlation technique for the alignment process, while Kepski et al. (2017) used the MATLAB Computer Vision toolbox and the Speeded-Up Robust Features (SURF) technique. In this study a Scale-Invariant Feature Transform (SIFT) algorithm is applied. The SIFT algorithm was developed by Lowe (1999) and is considered as a worldwide reference for image alignment and object recognition. As we follow the workflow of Portenier et al. (2019) we included the SIFT implementation from the open source library VLFeat-0.9.20 (Vedaldi et al., 2008).

The SIFT implementation consists of a feature detector and a feature descriptor. SIFT detects a predefined number of features in the input image which then are matched according to their similarity (euclidean distance) to the features detected in the master image. The matching pairs are then used to calculate a homography, which is a projective transformation between two images with the same camera position but with slightly different orientation. As a next step the homography is used to relate and align the input images to the master image. To solve the homography, at least four point-correspondences with each x and y coordinates are required. Since not every matched point of the SIFT algorithm may be correct, the homography is estimated by best matching points. For this, a robust fitting model called RANSAC (RANdom SAmple Consensus) is used. As a result of the alignment process, a homography matrix and an alignment mask are created for every aligned image. We refer to Portenier et al. (2019) for further technical details.

After successfully aligning the input images to the master image, we manually eliminated several images including their alignment mask. These images were not used for further processing as they were misaligned, too jittery, their FOV did not match the required FOV, or the depicted land scene was cloud or fog covered.

Then, we implemented a procedure to ensure a constant FOV over time. For that, we compared the available alignment masks and identified the image section which contained the largest common FOV. Hence, we define

$$\max(\text{FOV}) = \begin{cases} alignmentMask(_{x_i}) & \text{if } index(alignmentMask(_{x_i})) > index(alignmentMask(_{x_i-1})) \\ alignmentMask(_{x_i-1}) & \text{otherwise or if } index(alignmentMask(_{x_i})) < index(alignmentMask(_{x_i-1})) \end{cases} \tag{3.1}$$

Where $max(FOV)$ denotes the alignment mask with the largest common FOV, $index(alignmentMask(x_i))$ denotes the number of masked out pixels (black coloured) for the current webcam image alignment mask, and $index(alignmentMask(x_{\text{i-1}}))$ denotes the number of masked out pixels for the previous webcam image alignment mask. As a result, the current mask x_{i} is defined as the mask with the largest common FOV, when the number of black pixels is greater in the current alignment mask x_{i} compared to the previous alignment mask $x_{\text{i-1}}$. With this procedure we identified the *alignmentMask* dated from 20 April 2018 as the largest common FOV for the Dorfberg site.

As a last step of the alignment procedure, we obtain a *finalMask*,

$$finalMask = silhouetteMask \times inputMask \times alignmentMask \tag{3.2}$$

as a product of all created masks, which is then superimposed on every aligned webcam image.

3.1.5 Automatic Snow Classification Algorithms

In this study we applied three different algorithms for pixel-level snow classification, often quoted in literature. Most snow classification methods are based on the principle of brightness intensity values to classify pixels as snow or no snow (Fedorov et al., 2015). Thus, also the algorithms used in this study, namely Salvatori's blue band thresholding (Salvatori et al., 2011), Härer's Principal Component Analysis (PCA) algorithm (Härer et al., 2013), and Härer's PCA algorithm with rock thresholding (Härer et al., 2016) are based on pixel-brightness snow classification.

Salvatori et al. (2011) developed a Snow-noSnow Software where the blue band frequency distribution in the histogram of a webcam image is analysed. In previous work, Salzano et al. (2008) demonstrated, that the presence of snow in an image induces a bimodal distribution of the blue band component. Let $LM(x, y)$ be the first local minimum of the blue component in the image histogram, and t a snow threshold. All Digital Numbers of the blue component (DN_{blue}) above threshold t are classified as snow-covered pixels. Hence, Fedorov et al. (2015) summarized the approach of Salvatori et al. (2011) as follows,

$$P(x, y) = \begin{cases} t_{snow} = LM(x, y) & \text{if } LM(x, y) \geq t \\ t_{snow} = t & \text{if } LM(x, y) < t \end{cases} \tag{3.3}$$

meaning that, having a first local maximum of the blue component *LM(x,y)* greater than t = *127* sets the snow threshold t_{snow} to the pixel intensity of the value located at the local maximum. Preceding statistical analysis conducted by Salzano et al. (2008) showed that a threshold t, corresponding to snow cover is in most cases $\geq$ 127.
If no local maximum exists, then the snow threshold t_{snow} is automatically set to the predefined snow threshold t_{snow} = *127*. Thus, pixel values with $DN_{blue} \geq t_{snow}$ or $DN_{blue} \geq 127$ are classified as snow (=1), whereas pixel values with $DN_{blue} < t_{snow}$ or $DN_{blue} < 127$ are classified as no snow (=0).

The second and third algorithm used in this study are both based on a snow classification routine developed by Härer et al. (2013, 2016). In their work they extend the blue band algorithm of Salvatori et al. (2011), in order to develop the PCA algorithm of Härer et al., 2013 and the PCA algorithm with rock thresholding (Härer et al., 2016). In this study we apply the algorithms of Härer et al. (2013, 2016) separately, in order to assess their performance individually.

Based on their previously published snow classification routine PRACTISE V.1.0. (Härer et al., 2013), they extended the algorithm to PRACTISE V.2.1. by including additional algorithms that address snow in shadow-affected images. In PRACTISE V.2.1. the blue band algorithm of Salvatori et al. (2011) was first implemented to ensure

correct snow classification in well illuminated areas. Then, as a second step, Härer et al. (2016) included a PCA of the pixel colour space of an image. A PCA orthogonally transforms the axes of an RGB space into a new principal component (PC) space and shifts the centre of the coordinate system to the mean value of the three-dimensional data set (Härer et al., 2013). The axis direction of the first PC (PC_1) explains the largest variance in the given data set, whereas the second principal component (PC_2) is orthogonal to PC_1. PC_2 explains the second largest variance in the data set. The higher the number of PCs the less variance is explained. In PRACTISE V.2.1. PC_1 is not required for further processing, since the information stored in PC_1 is redundant with the information given and analysed by the blue band thresholding of Salvatori et al. (2011). According to Härer et al. (2016) empirical studies have shown that shaded snow pixels yield in higher PC_2 than PC_3 values. As a result, PC_2 and PC_3 are considered to be relevant for distinguishing shaded snow from other surfaces. Hence, pixels are classified as snow-covered if they satisfy the following statement:

$$P(x,y) = \begin{cases} 1 & \textit{if } PC_3 < PC_2 \textit{ and } DN_{blue} \geq t_{snow} \\ 0 & \textit{otherwise} \end{cases} \quad \textit{(adapted from Härer et al. (2016))} \tag{3.4}$$

The third algorithm, PCA with rock thresholding (Härer et al., 2016), extends the blue band algorithm of Salvatori et al. (2011) and the PCA algorithm of Härer et al. (2016). This algorithm separates sunlit rocks from snow as they have similar reflectance properties. It is known that the reflectance values of rock surfaces increase from shorter (blue) to longer (red) wavelengths in the visible spectra (Härer et al., 2016). Hence, the reflectance values of sunlit rocks increase from blue (DN_{blue}) to red (DN_{red}). Therefore, pixels that are not classified as sunlit snow (blue band algorithm of Salvatori et al. (2011)) or shaded snow (PCA algorithm of Härer et al. (2013)) are identified as sunlit rocks if they fulfil,

$$sunlit\_rocks = DN_{red} \geq DN_{blue} \textit{ (adapted from Härer et al. (2016))} \tag{3.5}$$

Hence, only the pixels that do not meet the sunlit rock conditions are classified as snow-covered. The sunlit rocks condition is then combined with the other two algorithms, yielding in a differentiated classification of snow-covered, snow-free, and sunlit rock pixels.

3.1.6 Snow Map Generation

In order to retrieve fSCA-data, corresponding to a real world 3D-space, the snow classified 2D-image needs to be georectified and projected on the terrain. In contrast to Portenier et al. (2019) who estimated the camera location and parameters, that information was given for the Dorfberg site. Thus, the computationally intensive part of georectification was accelerated as the coordinates of the installed camera and elevation above ground were known.

For generating georeferenced snow cover maps out of snow classified webcam images, we use the image-to-DEM registration, proposed by Portenier et al. (2019) that includes a transformation matrix. This matrix is based on a 360° visibility map of the webcam location, and calculated following the viewshed generation module in PRACTISE V.1.0. The transformation matrix relates each pixel of the master image to its real 3D coordinates (Dizerens, 2015). As we aligned each input image to the

master image, this transformation matrix is valid for all images at this site. As a result of this procedure we obtain georeferenced snow maps both in PNG and GEOTIFF format for all snow classification algorithms. The colours indicate whether a grid cell is snow-covered (blue), snow-free (red) or not visible (transparent) from the position of the webcam. Consequently, the retrieved snow map has a spatial resolution of 2x2m, since the map is calculated with the DEM of SwissALTI3D (Section 2.2).

3.1.7 Retrieval of Fractional Snow-Covered Area

After obtaining snow maps for the seasons 2015/2016 to 2019/2020 for the entire slope of the Dorfberg, we derived the fSCA-data. Hence, by counting the number of snow-covered pixels, snow-free pixels and invisible pixels, we calculated fSCA relative to the FOV [0, 1]. We stored the fSCA-data from October to May for each season for all snow classification algorithms in a comprehensive data base.

For the comparison and validation of JIM_OSHD modelled fSCA with webcam retrieved fSCA, we overlaid the generated snow map on the JIM_OSHD grid tiles. The intersecting tiles that cover the Dorfberg area are p6, p7, p11, p12 and p13 (Section 2.3). A batch process implemented in QGIS (QGIS.org, 2020), overlaid and cut the georeferenced snow maps (GEOTIFF format) to the extent of each JIM_OSHD tile. Thus, for each snow map we obtained five separate snow maps with the size of the OSHD tiles, with pixel colours indicating if the area is snow-covered, snow-free or not visible from the webcam. Then, with a pixel counting procedure in Matlab we determined the percentages of JIM_OSHD tile seen by the webcam.

Webcam fSCA-data was only calculated for correctly classified images, i.e. images where the applied algorithm did not show obvious errors. We analysed the retrieved snow map fSCA-data with time and flagged the dates where the fSCA-data deviated substantially from other fSCA-data. After flagging, we assessed the respective snow classified 2D-images individually and decided whether the algorithm performed well or not. For instance, if the algorithm classified the snow-free forest as snow-covered or a large part of snow-covered land surface as snow-free, these were criteria to flag the image. fSCA-data of the incorrectly classified and flagged images were disregarded for further processing. Thus, the number of correctly classified images mirrors how well the three algorithms performed.

3.2 Validation

To evaluate the performance of the snow classification algorithms we validated 13 images in winter season 2013/2014. These images were selected within the stages of early winter, mid-winter, peak winter and late winter according to the SLF bulletin (Zweifel et al., 2016).

Out of the 13 validated images, ten images are chosen under sunny weather conditions with a well illuminated scenery. The remaining three images show a cloud and fog covered scenery in order to evaluate the algorithm performance during poor weather conditions. Identically to the snow classification routine, described in Section 3.1, we aggregated the images into a daily composite image (Section 3.1.3), aligned them to the master image (Section 3.1.1) and ran the automatic snow classification routine for each of the three classification algorithms (Section 3.1.5). Unlike the usual procedure, described in Sections 3.1.6 and 3.1.7, we did not compute a georeferenced snow map,

but only used the classified 2D-webcam images. For validation, we used a random sampling approach within the defined FOV, similar to Fedorov et al. (2015). Within that FOV, 117 randomly distributed pixels were selected and classified as snow-covered (1) or snow-free (0) for each algorithm in a binary way. A snow-covered pixel had a value 1 and a snow-free pixel a value of 0. Then, a ground truth snow classification was created by deciding if the same 117 pixels on the original, non-classified image were snow-covered or snow-free. Figure 3.6 shows the 117 randomly distributed pixels over the snow classified images for all algorithms and the ground truth image for 9 March 2014.

(A) Original image.

(B) Blue band algorithm (Salvatori et al., 2011).

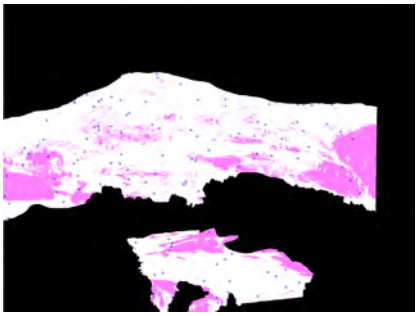

(C) PCA algorithm (Härer et al., 2013).

(D) PCA algorithm rock (Härer et al., 2016).

FIGURE 3.6: Webcam image from 9 March 2014 for the Dorfberg site in Davos. For each of the algorithms the same 117 pixels are chosen for validation (blue circles). The white color shows the snow-covered area, while the pink color represents the snow-free area for each algorithm.

In order to evaluate the validation analysis of the snow classification algorithms, we generated confusion matrices (Table 3.1) for every validation image and algorithm. With the quality metrics Accuracy (Acc), Probability of Detection (POD), and Probability of False Detection (POFD), we evaluated the performance of each algorithm. POD gives information about the proportion of the positive cases (e.g. snow-covered pixels) in the data, that are correctly identified as such. While POFD represents the proportion of negative cases (e.g. snow-free pixels) that are incorrectly classified as positive cases in the data.

TABLE 3.1: Confusion matrix calculated for the validation analysis and in parentheses for the simple model to compare the true and simulated onset of wet-snow avalanche activity ($OWSAAC_{\text{true}}$ and $OWSAAC_{\text{sim}}$).

		observed pixel ($OWSAAC_{true}$)	
		not snow-covered (*no OWSAAC*)	snow-covered ($OWSAAC$)
classified pixel ($OWSAAC_{sim}$)	not snow-covered (*no OWSAAC*)	a: correct non-event	b: missed event
	snow-covered ($OWSAAC$)	c: false alarm	d: correct event

3.3 Snow Height Comparison

For measuring the snow height (HS) distribution, photogrammetric surveys of Unmanned Aerial Vehicles (UAV) are a commonly used tool for validating snow cover models. By partitioning the UAV received HS-data into the JIM_OSHD tiles, we conducted a comparison and validation analysis between the UAV HS-data and the JIM_OSHD HS-data. In this study we analysed six tiles of the JIM_OSHD grid p1, p2, p3, p7, p8, and p9 covering the valley from west to east (Figure 2.3). After cutting the UAV HS-data into these tiles, we calculated the mean and standard deviations of UAV HS for each tile.

3.4 Onset of Wet-Snow Avalanche Activity Cycles

The onset of wet-snow avalanche activity is challenging to detect and predict and has therefore been the subject of many studies (e.g. Bellaire et al. (2017) and Mitterer (2012)). In this work we use the Onset of Wet-Snow Avalanche Activity Cycles (henceforth abbreviated as *OWSAAC*) in order to link it with seasonal dynamics of fSCA and SWE retrieved from the JIM_OSHD model.

Since the avalanche activity is well documented at the Dorfberg site, the *OWSAAC* can be defined. To determine a day i of wet-snow avalanching (DOA_i) we define that a specific number of wet-snow avalanches needs to be reported at a day. We set this threshold to $t_{DOA} \geq 2$, as Schweizer et al. (2020) found that the average number of avalanches per day was 1.3 for dry-snow conditions and 1.8 for wet-snow conditions. Hence, in this study we define DOA_i as following,

$$DOA_i = \begin{cases} 1 & \textit{if } n \geq t_{DAO} \\ 0 & \textit{otherwise} \end{cases} \tag{3.6}$$

where n denotes the observed number of wet-snow avalanches per day.

Second, we define that the true onset of a wet-snow avalanche activity cycle may only begin if at least two consecutive days (*i* and *i+1*) fulfil the condition set for DOA_i. Hence,

$$OWSAAC_{true} = \begin{cases} 1 & if\ DOA_i = 1\ and\ DOA_{i+1} = 1 \\ 0 & otherwise \end{cases} \tag{3.7}$$

However, this approach may be inaccurate, as determine wet-snow avalanche cycles requires information about many other parameters, such as the liquid water content in the snowpack (Mitterer et al., 2013).

For verification, we compared the $OWSAAC_{true}$ of the Dorfberg with the *OWSAAC* dates from the SLF winter reports (Trachsel et al., 2020; Winkler et al., 2019; Zweifel et al., 2019, 2017, 2016). Table 3.2 gives an overview on the defined $OWSAAC_{true}$ for the Dorfberg site, the Dischma area and for entire Switzerland. For the Dorfberg site we used the georeferenced avalanche data set and for the Dischma area we used the flagged webcam images on which avalanches occurred (Section 2.5). Comparing these data with the SLF winter reports comes with limitations, since they refer to the entire Alps.

TABLE 3.2: $OWSAAC_{true}$ for the Dorfberg site, Dischma area, and the Alps in Switzerland.

	Dorfberg p11 *OWSAAC_true* (Source: avalanche data set, SLF)	Dischma p1 to p36 *OWSAAC_true* (Source: webcam images evaluation)	Alps in Switzerland (source: SLF winter reports)
2015/2016	19.03.2016 – 23.03.2016	04.03.2016 - 06.03.2016	21.03.2016
2016/2017	11.03.2017 – 21.03.2017	08.03.2017 - 11.03.2017	08.03.2017 - 10.03.2017
2017/2018	03.04.2018 – 09.04.2018	21.04.2018 - 27.04.2018	05.04.2018 - 08.04.2018
2018/2019	08.04.2019 – 11.04.2019	02.04.2019 - 05.04.2019	15.04.2019
2019/2020	11.03.2020 – 23.03.2020	no data available	11.03.2020

3.5 A Simple Model to Detect the Onset of Wet-Snow Avalanche Activity Cycles

To detect the onset of a wet-snow avalanche cycle, we established a simple model only relying on past fSCA and SWE-data. The simple model enables us to hindcast *OWSAAC* events, i.e. to identify past *OWSAAC* events, but not to forecast, i.e. to predict future *OWSAAC* events, unless we use lower elevation tiles as predictors for higher elevation avalanches.
Both fSCA and SWE-data are retrieved from the JIM_OSHD model as the modelled parameters are more reliable than the webcam retrieved fSCA-data. We trained the simple model on data from the Dorfberg and evaluated its performance with Dorfberg webcam fSCA-data and with JIM_OSHD fSCA-data from the Dischma area.

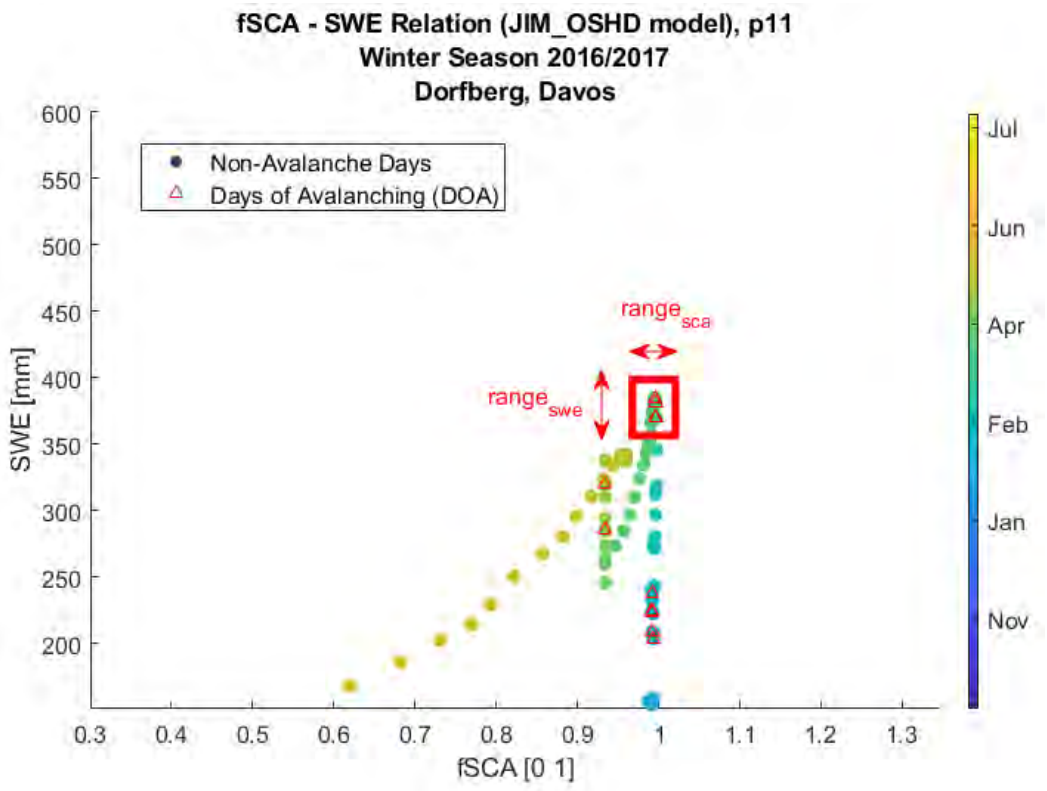

FIGURE 3.7: Zoomed in SCD curve for high fSCA-SWE values in winter season 2016/2017. Days of avalanching (DOA) are marked with red triangles, whereas the red bounding box with a size defined by the $range_{swe}$ and $range_{sca}$, captures the onset of wet-snow avalanche activity cycles ($OWSAAC$).

Wet-snow avalanches release when the snow cover starts to melt. This means that in the time after reaching a maximum value of both fSCA and SWE-data in a winter season, the onset of wet-snow avalanche cycles may take place. With the aim to capture this process, we defined a bounding box around the maximum values of fSCA and SWE in the fSCA-SWE relationship in which the $OWSAAC$ may occur (for illustration see Figure 3.7). Our approach followed three steps: (i) We normalized data of fSCA and SWE, (ii) a range was set for maximal values of fSCA and SWE, and (iii) model performance was evaluated.

(i) We normalized the parameters fSCA and SWE with their maximum value reached throughout each year for the winter seasons 2015/2016 to 2019/2020. Hence, the maximum values of fSCA and SWE for each year were assigned with a value of 1.

(ii) Second, we defined a condition that a simulated $OWSAAC_{sim}$ needs to fulfil:

$$OWSAAC_{sim} = \begin{cases} 1 & if \;\; fSCA_i > (1 - range_{sca}) \; and \;\; SWE_i > (1 - range_{swe}) \\ 0 & otherwise \end{cases} \tag{3.8}$$

where $fSCA_i$ and SWE_i are JIM_OSHD modelled fSCA and SWE-data of an arbitrary day i within the investigated winter seasons. Hence, if $fSCA_i$ and SWE_i are within a predefined percentile range ($range_{\mathrm{sca}}$ and $range_{\mathrm{swe}}$) of the maximum fSCA and SWE

values, day_i is considered to be a day where the $OWSAAC_{\text{sim}}$ may begin.
We defined $range_{\text{sca}}$ as a possible value between 0.0005 and 0.002 with an incremental step of 0.00001, and $range_{\text{swe}}$ as a possible value between 0.02 and 0.08 with an incremental step of 0.001. The decision to model $OWSAAC$ of the Dorfberg site with these ranges was made after a detailed analysis of the fSCA-SWE plots where the true wet-snow avalanche activity cycle onset was shown (Figure 3.7). Thus, these combinations resulted in 9211 runs that simulated the $OWSAAC$. For each combined $range_{sca}$ and $range_{swe}$, the $OWSAAC_{\text{sim}}$ was defined according to the conditions set in Equation 3.8.

(iii) Out of 9211 predefined percentile range combinations we proof all the data from the Dorfberg to find the best model. To evaluate model performance and retrieve the best combination of $range_{sca}$ and $range_{swe}$, we compared the simulated onset, $OWSAAC_{\text{sim}}$ with the true onset, $OWSAAC_{\text{true}}$. The performance of the model was evaluated by confusion matrices (Table 3.1), calculated for every $range_{sca}$ and $range_{swe}$. According to Mitterer et al. (2013) we considered the following measures and scores in order to identify best model:

$$\text{False Alarm Ratio, } FAR = \frac{c}{c+d}, \quad \text{best score} = 0 \tag{3.9}$$

$$\text{Probability of Detection, } POD = \frac{d}{b+d}, \quad \text{best score} = 1 \tag{3.10}$$

$$\text{Probability of False Detection, } POFD = \frac{c}{a+c}, \quad \text{best score} = 0 \tag{3.11}$$

$$\text{Hanssen Kuipers Score, } HK = \frac{d}{b+d} - \frac{c}{a+c}, \quad \text{best score} = 1 \tag{3.12}$$

$$\text{Accuracy, } Acc = \frac{a+d}{a+b+c+d}, \quad \text{best score} = 1 \tag{3.13}$$

As POD and POFD can be used for calculating the Receiver Operating Characteristic (ROC) curve and the Hanssen Kuipers score and the accuracy include all cells of the confusion matrix, we focus on these measures and scores. We want to mention that there are many other measures and scores that could be evaluated (Mitterer et al., 2013). However, choosing the relevant measures is not trivial and depends also on the purpose of the model that is evaluated.

Chapter 4

Results

In this Chapter, we show results of the different snow classification algorithms (Section 4.1) and report on the validation analysis (Section 4.1.2). Then, we present results of the comparison between JIM_OSHD model performance with webcam fSCA and UAV HS: First, we show differences and similarities between webcam fSCA-data and JIM_OSHD fSCA-data (Section 4.2.1). Therein, we focus on the elevation dependence of fSCA and melt-out dates (Section 4.2.2). Second in Section 4.2.3, we display the results of the comparison between UAV HS and JIM_OSHD HS.
In Section 4.3, we show characteristic snow cover depletion curves that link webcam and JIM_OSHD fSCA-data with JIM_OSHD SWE-data and wet-snow avalanche activity. Finally, we present results of our simple model to determine the onset of wet-snow avalanche activity cycles (Section 4.3.1).

4.1 Snow Cover Classification of Webcam Images

4.1.1 Visual Assessment

The number of correctly classified webcam images and thus snow maps, used for fSCA-data retrieval, varied depending on the snow classification algorithm. In Section 3.1.7 we defined correctly classified webcam images as images where the applied algorithm did not show obvious errors in pixel-wise classification. Obvious errors include, for instance, images where large parts of snow-covered area was not classified as snow-covered, or snow-free vegetation was classified as snow-covered.

TABLE 4.1: Time period and number of correctly classified webcam images separated by the three snow classification algorithms within the investigated winter seasons 2015/2016 to 2019/2020. Webcam images were available for every day during the months October to July.

Winter Season	Salvatori et al. (2011)	Härer et al. (2013)	Härer et al. (2016)
2015/2016	96	17	18
2016/2017	82	27	27
2017/2018	66	18	17
2018/2019	51	6	19
2019/2020	57	47	55
Total	352	115	136

We had to disregard a fair number of images, not only due to jittering of the webcam, cloud or fog covering the FOV, and maintenance issues, but most importantly due to the performance of the snow classification algorithms. Hence, we considered 352 valuable snow classified images for the algorithm of Salvatori et al. (2011); 115 for the algorithm

of Härer et al. (2013); and 136 for the algorithm of Härer et al. (2016). Table 4.1 gives an overview and lists the number of correctly classified images for each investigated winter season. The small sample size of correctly classified images by Härer et al. (2013, 2016) implies that their approaches had difficulties in correctly detecting fSCA at the Dorfberg site in many cases.

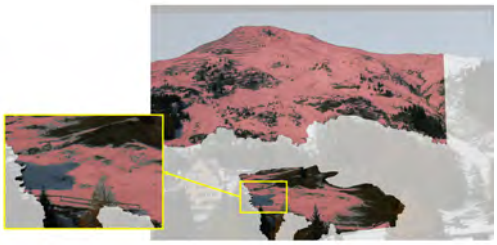

(A) Snow classification algorithm: Salvatori et al. (2011).

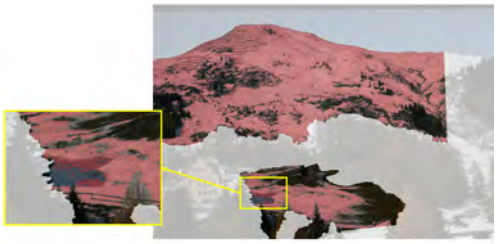

(B) Snow classification algorithm: Härer et al. (2013).

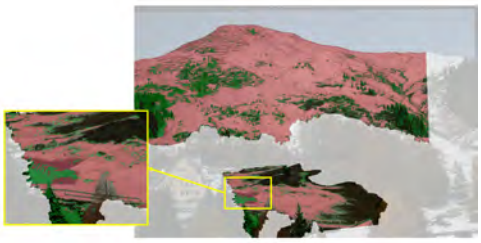

(C) Snow classification algorithm: Härer et al. (2016).

FIGURE 4.1: Snow classified webcam image on 14 November 2019 with the three algorithms (A to C). The pixels are classified as snow-covered area (red), not snow-covered area (transparent), and masked-out area (white). The yellow boxes with the zoomed-in insertions indicate where the snow classification algorithms differ the most. In Figure 4.1c, the green coloured area represent sunlit rocks.

Assessing the snow classified images visually, gives a good first overview of the performance for the three applied snow classification algorithms. An exemplary snow-classified composite webcam image taken on 14 November 2019 is shown in Figure 4.1. The red coloured areas represent the fSCA calculated with the snow classification algorithms; the white-greyish area represents the masked-out area (sum of the *inputMask*, *alignmentMask* and *silhouetteMask*), whereas the uncoloured layer represents snow-free pixels (i.e. vegetation or avalanche barriers). Additionally, the algorithm of Härer et al. (2016) detects sunlit rocks, shown with green colour (Figure 4.1c). Focusing on the yellow boxes, we saw that all algorithms had difficulties in correctly classifying shaded and poorly illuminated snow: The blue band algorithm of Salvatori et al. (2011) misclassified the shaded snow in the vicinity of building as snow-free (Figure 4.1a). We noticed that the misclassified pixels were confined within the boundary of the shadow. Also, both PCA algorithms of Härer et al. (2013, 2016) showed misclassifications for shaded snow (Figure 4.1b). However, there were generally fewer misclassifications of the shadowed pixels than with the blue band algorithm.

Other examples of webcam images revealed that, the algorithms of Härer et al. (2013, 2016) showed more misclassifications for pixels located at the left and right margin of the FOV and close to the horizon. Thus, as shown in Table 4.1, we had to disregard much more images classified with the Härer et al. (2013, 2016) algorithms compared to the algorithm of Salvatori et al. (2011).
Overall, the algorithms performed well as they classified the majority of all true snow-covered pixels as snow-covered. However, misclassifications may occur, for instance, when obstacles produce shade on the snow. In this case each algorithm behaved differently as they followed different approaches. In order to assess the performance of the algorithms qualitatively, we conducted a validation analysis (Section 4.1.2).

From the snow classified 2D-images (Figure 4.1), we generated daily georeferenced snow maps in GEOTIFF-format. Figure 4.2 shows the resulting snow map with a spatial resolution of $4m^2$ for each pixel on the webcam, calculated with the algorithm of Salvatori et al. (2011) and dated on 14 November 2019. The blue coloured pixels indicate the snow-covered area, red pixels refer to the snow-free area, white pixels show the masked-out area, and black pixels refer to the terrain not seen from the camera location. Finally, the fSCA-data is obtained by dividing the number of snow-covered pixels through the sum of all non-masked pixels. For instance, on 14 November 2019 the fSCA was 0.686 (= 68.6%).

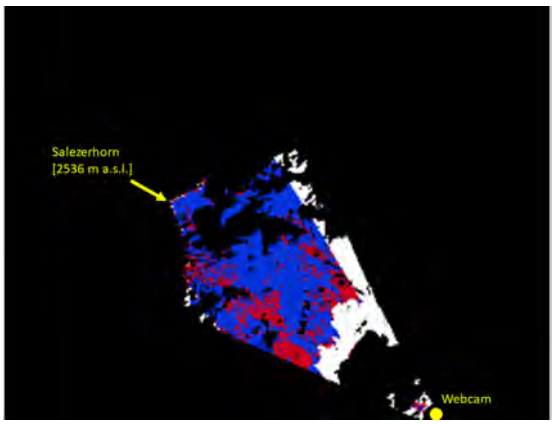

FIGURE 4.2: Georeferenced snow map on 14 November 2019 for the blue band algorithm (Salvatori et al., 2011) at the Dorfberg site. Pixels are classified as snow-covered (blue), snow-free (red), masked-out area (white) and terrain not seen from the webcam location (black). The webcam location and the Salezerhorn are marked in yellow colour for better orientation.

4.1.2 Validation

To the best of our knowledge, no study has provided a quantitative validation analysis between the algorithms of Salvatori et al. (2011) and Härer et al. (2013, 2016). We therefore quantitatively assessed how well the three algorithms performed in order to identify the most suitable algorithm for the Dorfberg site. We validated thirteen composite images in winter season 2013/2014, each containing the same 117 randomly distributed validation points within the FOV (Section 3.2). In Table 4.2 we state additional information about the weather condition and accuracy for each of the validated

images. The probability of false detection (POFD) and probability of detection (POD) and were averaged for each algorithm. All the quality metrics are separated by the three investigated algorithms, Salvatori et al. (2011) and Härer et al. (2013, 2016).

TABLE 4.2: Overview of the quality metrics and indication about the weather condition for thirteen validated webcam images in winter season 2013/2014 for the Dorfberg site. Accuracy is given for every validated image, while the probability of false detection (POFD) and probability of detection (POD) were averaged for every snow classification algorithm separately. The values are rounded to two decimals.

		Salvatori et al. (2011)	Härer et al. (2013)	Härer et al. (2016)
Date	Weather	$Accuracy_{salv}$	$Accuracy_{haer}$	$Accuracy_{haer-rock}$
18.11.2013	sunny	0.85	0.88	0.87
29.11.2013	sunny	0.92	0.94	0.94
29.12.2013	sunny	0.97	0.94	0.93
21.01.2014	cloudy/foggy	0.56	0.69	0.74
29.01.2014	sunny	0.97	0.92	0.92
20.02.2014	sunny	0.94	0.94	0.93
05.03.2014	cloudy/foggy	0.97	0.95	0.94
07.03.2014	sunny	0.97	0.96	0.95
09.03.2014	sunny	0.93	0.88	0.88
14.03.2014	sunny	0.96	0.93	0.89
24.03.2014	cloudy/foggy	0.89	0.89	0.89
25.03.2014	sunny	0.92	0.92	0.93
02.04.2014	sunny	0.94	0.68	0.67
Mean accuracy		0.91	0.89	0.88
Mean POFD		0.08	0.17	0.22
Mean POD		0.87	0.85	0.86

The highest mean accuracy (0.91) was for the blue band algorithm of Salvatori et al. (2011) (Table 4.2). With 0.89 and 0.88, the mean accuracy was slightly lower when applying the algorithms of Härer et al. (2013, 2016). For images with cloudy/foggy weather conditions, no conclusive statement regarding the accuracy can be made: For instance, for the validation image taken on 21 January 2014, the algorithm of Salvatori et al. (2011) performed worst and the algorithm of Härer et al. (2016) best. In contrast, on 5 March 2014 Salvatori et al. (2011) performed better than Härer et al. (2013, 2016), while on 24 March 2014 all algorithms showed identical accuracy.
Looking at other metrics, the mean POD of the blue band algorithm equals 0.87 and is clearly higher than its mean POFD of 0.08. In other words, 87% of the snow-covered pixels were correctly classified by the blue band algorithm, while only 8% of the snow-free pixels were misclassified as snow-covered. Comparing these values with those of the algorithms of Härer et al. (2013, 2016), it becomes apparent that their POD is lower and their POFD is higher. Accordingly, both algorithms of Härer et al. (2013, 2016) classified fewer snow-covered pixels correctly, and misclassified more snow-free pixels as snow-covered compared to the algorithm of Salvatori et al. (2011).
Hence, as fewer pixels were classified correctly with the algorithms of Härer et al. (2013, 2016) we had to disregard more classified webcam images which corresponds to a lower sample size. Thus, according to the validation analysis, the algorithm of Salvatori et al. (2011) performed better at the Dorfberg site in almost every assessed quality metric compared to the other two classification algorithms Härer et al. (2013, 2016).

4.2 Comparison between JIM_OSHD Model and Snow Parameters

In this Section webcam fSCA-data is compared with JIM_OSHD fSCA-data. A particular focus was set on the two winter seasons 2016/2017 and 2017/2018 as well as the elevation dependency of fSCA (Section 4.2.2). As JIM_OSHD-data has only been available since 2015 in its current version, we investigated a winter season below average snow depth (2016/2017) and one winter with average to above snow depth (2017/2018) in more detail. Furthermore, we evaluated the performance of modelled HS-data by comparing JIM_OSHD HS with UAV HS-data (Section 4.2.3).

4.2.1 Comparison between JIM_OSHD fSCA-data and Webcam fSCA-data

Figure 4.3 displays JIM_OSHD fSCA-data and webcam fSCA-data for winter seasons 2016/2017 and 2017/2018 within tile p12. Figures of all investigated winter seasons 2015/2016 to 2019/2020 and other tiles p6, p7, p11, p12 and p13 are shown in the Appendix (Figures A.2 to A.6). Webcam fSCA-data, obtained by the different snow classification algorithms are shown with coloured points, whereas JIM_OSHD fSCA-data is represented by a solid blue line.

Figure 4.3 reveals some minor and major gaps where webcam fSCA-data were missing. Especially for the algorithms of Härer et al. (2013, 2016) we only obtained very few valid images (Table 4.1). These data gaps were caused by the manual elimination of images during periods of high cloud and fog coverage, misalignments and mostly misclassifications. In contrast, JIM_OSHD obviously provides continuous fSCA values on a daily basis.
Focusing on the curve shape of the webcam fSCA-data and JIM_OSHD fSCA-data, we note that the curves are similar, especially those calculated with the algorithm of Salvatori et al. (2011) (green points). However, while there were only minimal variations in JIM_OSHD fSCA-data during peak winter months (January to March), the webcam fSCA showed higher variations at smaller temporal scale. Focusing on the early winter 2016/2017, we see that the snowfall event in November 2016 was captured well by both the webcam fSCA-data and the JIM_OSHD fSCA-data. Also, short-term melt-out patterns towards the end of December 2016 are similarly recognized by the JIM_OSHD fSCA-data and the webcam algorithms, Salvatori et al. (2011) and Härer et al. (2013). However, the melt-out patterns were more pronounced for the webcam fSCA-data, as webcam fSCA became almost zero during this time, while JIM_OSHD fSCA remained around 0.35. During peak winter, both the webcam fSCA and JIM_OSHD fSCA reached their maximum values, which were more or less consistently greater than 0.9 over several months. Then, during late winter or in early spring, the curve indicated the beginning of melt-out processes. Although the shape is similar for both webcam and JIM_OSHD fSCA-data, the webcam fSCA-data indicated earlier melt-out, compared to the JIM_OSHD fSCA-data.

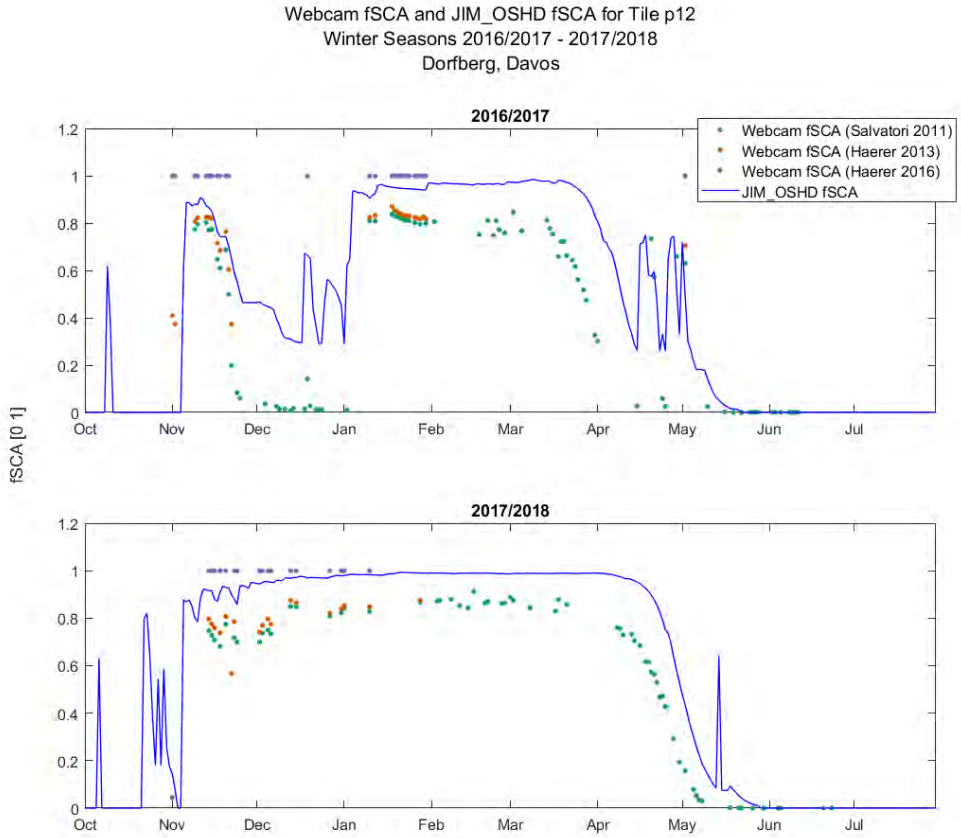

FIGURE 4.3: Comparison between JIM_OSHD fSCA-data and webcam fSCA-data for tile p12 in winter seasons 2016/2017 and 2017/2018. Webcam fSCA-data was calculated with the snow classification algorithms Härer et al. (2013, 2016) and Salvatori et al. (2011) and is shown with different colours (points). The blue solid line represents the JIM_OSHD fSCA-data for the same tile p12.

Overall, a consistent pattern can be observed for the algorithm of Salvatori et al. (2011) and Härer et al. (2013): Apart from some exceptions, webcam fSCA was lower than the JIM_OSHD fSCA for the Dorfberg site, independent of the season or fSCA magnitude. Hence, there is a more or less constant offset between webcam fSCA and JIM_OSHD fSCA-data. However, for the PCA algorithm with rock thresholding of Härer et al. (2016) this was not the case: Figure 4.3 shows that during peak winter the webcam fSCA retrieved with the algorithm of Härer et al. (2016) (purple points) showed constant values equal or even greater than JIM_OSHD fSCA-data. This algorithm was especially wrong at the start of the melt-out season in the late winter stage or early spring stage. During this time of the year, the algorithm still detected high webcam fSCA values (fSCA ~1) compared to the then already decreasing JIM_OSHD fSCA or decreasing values with the other algorithms.

TABLE 4.3: Pearson's correlation coefficients for webcam fSCA and JIM_OSHD fSCA-data, rounded to two decimals. The correlation coefficients are calculated for all algorithms, investigated tiles and winter seasons 2015/2016 to 2019/2020. The sample size n of each algorithm is given in parentheses. The sample size of the JIM_OSHD model is n = 1523. Significant correlation coefficients with p-value < 0.05 are marked in bold.

	Tile	2015/2016	2016/2017	2017/2018	2018/2019	2019/2020
Salvatori (2011) (n = 352)	p6	**0.25**	**0.25**	0.17	0.1214	0.02
	p7	**0.99**	**0.99**	**0.98**	**0.64**	**0.66**
	p11	**0.71**	**0.86**	**0.95**	**0.64**	**0.77**
	p12	**0.67**	**0.75**	**0.88**	**0.80**	**0.89**
	p13	**0.33**	**0.41**	**0.50**	**0.30**	**0.36**
Haerer (2013) (n = 115)	p6	-0.04	-0.34	0.46	0.37	**0.39**
	p7	**0.96**	**0.57**	**0.55**	**0.83**	**0.30**
	p11	0.50	**0.63**	0.08	0.60	0.27
	p12	**0.85**	**0.74**	**0.67**	**0.91**	**0.60**
	p13	0.29	**0.75**	**0.81**	**0.75**	0.28
Haerer (2016) (n = 136)	p6	0.03	-0.37	0.33	-0.40	0.03
	p7	∼0	∼0	∼0	∼0	∼0
	p11	∼0	∼0	∼0	∼0	∼0
	p12	∼0	∼0	∼0	∼0	∼0
	p13	∼0	∼0	∼0	∼0	∼0

We also performed a Pearson's correlation analysis between the three webcam algorithms and the JIM_OSHD model. A correlation coefficient with value +1 indicates the highest positive correlation, -1 the lowest negative correlation, and 0 indicates no correlation (Kazmier, 2003). Table 4.3 reports the Pearson's correlation coefficients between webcam fSCA and JIM_OSHD fSCA-data in all assessed winter seasons. Statistically significant correlation coefficients have a p-value < 0.05 and are marked in bold. The correlation coefficients were rounded to two decimals for better readability.

The correlation analysis revealed that the highest and most consistent correlation coefficients were achieved between the JIM_OSHD model and the algorithm of Salvatori et al. (2011). Also, with p-values lower than 0.05 for almost all tiles and years, their coefficients were statistically significant. Only in winter season 2018/2019 the correlation coefficients between the JIM_OSHD model and the PCA algorithm of Härer et al. (2013) showed higher values for some tiles. Still, these values were less significant compared to the correlation coefficients of the JIM_OSHD model and the webcam fSCA retrieved by the algorithm of Salvatori et al. (2011).
Overall, the highest correlation coefficient (0.9889) of all tiles and winter seasons was achieved during winter season 2016/2017 in tile p7 for the JIM_OSHD model and the algorithm of Salvatori et al. (2011). The lowest correlation values with values of nearly zero (∼0) were found for the correlation between the JIM_OSHD model and the fSCA-data calculated with the algorithm of Härer et al. (2016). It is likely that the number of correctly classified images (Table 4.1) is related to the correlation results. Hence, while the JIM_OSHD fSCA had an unchanged sample size of n = 1523, the sample size of the webcam algorithms differed. For the algorithm of Salvatori et al. (2011) there was a sample size of n = 352. Smaller sample sizes result in lower correlation coefficients (Bujang et al., 2016). Thus, the small sample size of Härer et al. (2013) (n = 115) and Härer et al. (2016) (n=136), in combination with the large sample size of the JIM_OSHD model, contributed to their lower and less significant correlation coefficients. Although the sample size of Härer et al. (2016) was larger than the sample size of Härer et al. (2013), the correlation values of Härer et al. (2016) with the JIM_OSHD

were much lower. This may be due to the fact that fSCA-data retrieved by Härer et al. (2016) remained almost constant (~1) throughout the entire winter season (Figure 4.3), whereas fSCA-data obtained by Härer et al. (2013) detected reasonable variation over time, resulting in higher correlation coefficients.

To sum up, the correlation coefficients between the JIM_OSHD model and the algorithm of Salvatori et al. (2011) were most significant. Thus, for comparison and validation analyses between the JIM_OSHD model and webcam fSCA-data, the algorithm of Salvatori et al. (2011) is considered to be the most appropriate.

4.2.2 Elevation Dependence

In early winter, snow accumulation first starts at higher elevation and later propagates to lower elevation. The opposite happens during spring, when the snow cover first starts melting at lower elevation, before the fSCA also starts to decrease at higher elevation (Grünewald et al., 2014). Figure 4.4 illustrates this characteristic, showing webcam (points) and JIM_OSHD (lines) retrieved fSCA for all tiles in different elevations in winter season 2016/2017 at the Dorfberg site. The elevation dependence of fSCA-data for winter seasons 2015/2016, 2018/2019 and 2019/2020 are shown in the Appendix in Figures A.7, A.8, A.9 and A.10. Li et al. (2019) defined the melt-out date as the day when the pixels were no longer covered by snow, i.e. fSCA = 0. In this study we defined the melt-out date as a day after 1st of March, when fSCA $\leq$ 0.1, because snow patches caused by terrain irregularities or shading, might have remained even though fSCA was close to zero.

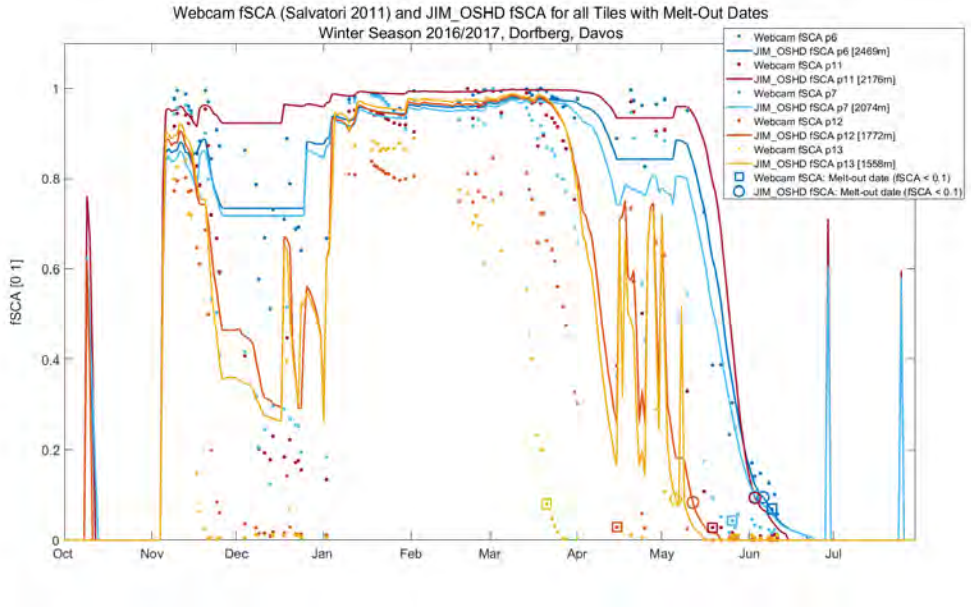

FIGURE 4.4: Comparison between data of webcam fSCA (points) and JIM_OSHD fSCA (solid lines) for winter season 2016/2017 coloured according to their altitude. A melt-out date is defined if fSCA $\leq$ 0.1 is met and marked with a circle for webcam fSCA-data and a square for JIM_OSHD fSCA-data.

Figure 4.4 shows that the JIM_OSHD model recorded a first snowfall event in October 2016, when no valid webcam fSCA-data was available. Then, in early November 2016 a second snowfall event occurred, causing a rapid increase of fSCA for all elevation ranges, observed in both the webcam and the JIM_OSHD fSCA-data. Then, in December 2016 fSCA decreased to around 0.1 to 0.4 again at lower elevations (p12 and p13), while fSCA at higher elevations (p6, p7, and p11) remained constant between 0.75 and 0.95. The decrease was more pronounced for webcam fSCA as it temporarily reached zero. In contrast, JIM_OSHD fSCA fluctuated around 0.3 to 0.7 during that period.

In early January 2017, snow accumulated again, and has led to a strong relative increase in fSCA at lower elevations, and a less pronounced increase at higher elevations, as the ground there was already partly covered with snow. This pattern is similar for both fSCA retrieval methods. During peak winter (January to March) webcam and JIM_OSHD fSCA reached their maximal values and did not vary much. This is because fSCA stays unaltered once the surface (except trees, buildings, avalanche barriers) is snow-covered, even though SWE or HS may increase due to snowfall. Comparing Figure 4.4 to the other seasons displayed in the Appendix (Figures A.7, A.8, A.9 and A.10) we see that the length of peak winter varied from one season to the other and was also elevation dependent. For instance, the duration of peak winter for 2017/2018 (Figure A.8) was more pronounced compared to the winter season 2016/2017.

In spring, the beginning of the elevation dependent melt-out season, i.e. when fSCA starts to decrease, can be shown. First, fSCA started to decrease at lower elevation (p12 and p13), soon followed by a decrease in fSCA at higher elevation (p7, p11 and p6). Focusing on fSCA at lower elevation, the offset in fSCA between webcam retrieved fSCA and JIM_OSHD fSCA was substantial. We see the beginning of the melting season was first recorded in the webcam retrieved fSCA, prior to the JIM_OSHD fSCA. A similar pattern can be observed at higher elevation, where the temporal offsets between the webcam fSCA and JIM_OSHD fSCA-data were smaller however. Hence, depending on the elevation, there was a time lag between JIM_OSHD fSCA-data and webcam fSCA-data that was most pronounced for early and late winter.
Later, during the melting season, where fSCA has already decreased, fSCA increased again due to a snowfall in April. Between mid-April and early May, fSCA at lower elevation (p12 and p13) showed high variability over time. Similarly, at higher elevation (p7, p11 and p6), the beginning of the melting season was interrupted by this snowfall event in April. However, fSCA remained almost at a constant high level until early May, as the decrease in fSCA has not progressed far enough yet.

Table 4.4 gives an overview of the melt-out dates for the tiles p13 and p6 at lowest and highest elevation, respectively. Again, a melt-out date is defined by fSCA ≤ 0.1 after 1 March. The complete table for all tiles and winter seasons is shown in the Appendix (Table A.1). Between March and June 2017 the melt-out dates of webcam and JIM_OSHD fSCA took place. First at lower elevation (p12, p13) and later at higher elevation (p7, p11, p6). We note, that the webcam fSCA-data in general showed earlier melt-out dates (circles in Figure 4.2.2), up to two months for p13 in year 2015/2016, compared to JIM_OSHD fSCA melt-out dates (squares in Figure 4.2.2). We want to point out, that the discrepancies were larger in lower elevations (e.g. p13) compared to higher elevations (e.g. p6).

TABLE 4.4: Melt-out date for webcam fSCA (Salvatori et al., 2011) at tile p13 and p6 and JIM_OSHD fSCA in winter seasons 2015/2016 to 2019/2020. A melt-out date is defined if fSCA ≤ 0.1 is met after 1 March. In parentheses the values corresponding to the first fSCA value that has met fSCA ≤ 0.1 are given.

	webcam fSCA p13 [1558 m a.s.l.]	JIM_OSHD fSCA p13 [1558 m a.s.l.]	webcam fSCA p6 [2469 m a.s.l.]	JIM_OSHD fSCA p6 [2469 m a.s.l.]
2015/2016	30.03.2016 (0.0680)	21.05.2016 (0.0821)	24.06.2016 (0.0811)	25.06.2016 (0.0957)
2016/2017	21.03.2017 (0.0805)	06.05.2017 (0.898)	09.06.2017 (0.0686)	06.06.2017 (0.0943)
2017/2018	10.04.2018 (0.0536)	03.05.2018 (0.0858)	04.06.2018 (0.0911)	04.06.2018 (0.0997)
2018/2019	03.04.2019 (0.0757)	04.06.2019 (0.0886)	after 11 June 2019	03.07.2019 (0.0986)
2019/2020	26.03.2020 (0.7570)	23.04.2020 (0.0883)	after 11 May 2020	29.05.2020 (0.0958)

4.2.3 Comparison between JIM_OSHD HS and UAV HS

Figure 4.5 illustrates the results of the comparison between JIM_OSHD HS and the HS-data from the UAV flight in the Dischma area. The results are sorted by the mean altitude of the corresponding JIM_OSHD tile. Both data sets were obtained for 7 April 2018 with snow heights between 1 m and 2 m. The blue points refer to the HS values of the JIM_OSHD model, the purple crosses show the mean UAV HS-data over the area of the corresponding OSHD tile (p1, p2, p3, p7 and p8, Table 2.3). The vertical purple and orange bars indicate one, respectively two standard deviations of the UAV HS values. On the x-axis the altitude at the central point of the tile is shown, with the corresponding tile in parentheses.

With snow heights between 0.9 m and 1.9 m UAV HS showed noticeably lower values compared to the HS calculated by the JIM_OSHD model with values between 1.3 m and 2 m. The rather high standard deviation of UAV HS indicated, that the UAV HS with its spatial resolution of 0.3 m had substantial variations within the considered tiles of $1km^2$. Only at p3 and p8 the JIM_OSHD HS-data lies within 1σ of the UAV HS. The differences between UAV HS and JIM_OSHD HS were most pronounced for tile p1 with a value of 0.95 m. Similarly, tiles p2 and p7 display a difference of about 0.87 m. On the other hand, the discrepancy between UAV HS and JIM_OSHD HS equalled only 0.02 m for tile p3 and 0.08 m for tile p8. No UAV HS-data was obtained at elevation zones 2100 m a.s.l. and 2200 m a.s.l., as the UAV covered only a restricted area in the Dischma valley.

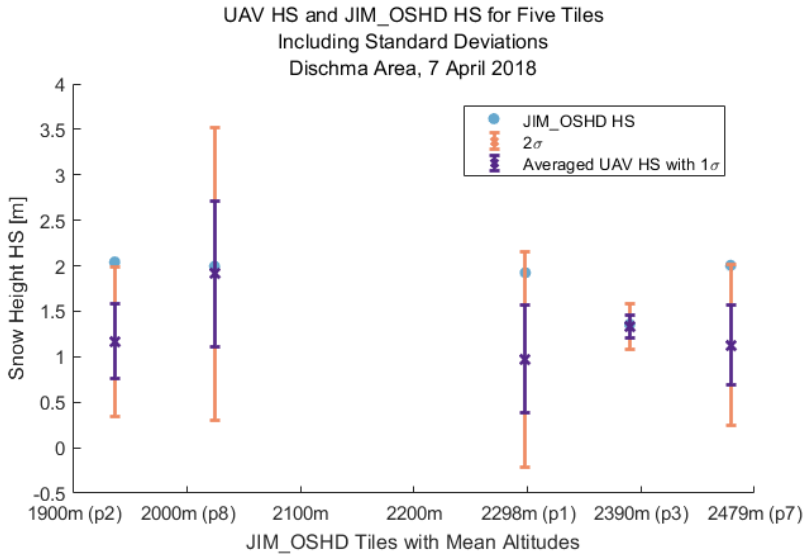

FIGURE 4.5: JIM_OSHD HS-data (blue points) and UAV HS-data (purple crosses) of the Dischma area with their standard deviations for five tiles of the JIM_OSHD model, sorted by their altitudes. The purple whiskers indicate one standard deviation (1σ) and the orange whiskers show two standard deviations (2σ) of the UAV HS. Both HS-data sources refer to 7 April 2018.

4.3 Link between fSCA, SWE and Wet-Snow Avalanches

Linking seasonal dynamics of fSCA and SWE with wet-snow avalanche activity result in so called snow cover depletion (SCD) curves (Fassnacht et al., 2016; Grünewald et al., 2014). SCD curves are a widely-used tool for visualizing such links, especially as the curves can be divided into accumulation and ablation stages. The ablation stages can give more information about the winter seasons, i.e. HS and SWE at the peak of winter and melt rates.

In Figures 4.6 and 4.7 we show SCD curves for winter seasons 2016/2017 and 2017/2018, each starting in October and ending in early July. Each data point is coloured corresponding to a day of the year. Additionally, some data points were marked with a red triangle, to indicate a day of avalanching (DOA). According to the avalanche data for the Dorfberg site, the elevation zone in which almost all wet-snow avalanches released was at about 2100 m a.s.l.. With a mean altitude of 2176 m a.s.l. tile p11 best represents this elevation. Thus, most of the previous and subsequent analyses were done with this tile. Note that the amount of SWE differed from one season to the other: While SWE reached its maximum value of about 420 mm in the winter season of 2016/2017, the winter season of 2017/2018 showed SWE values up to 750 mm. Figures A.11 and A.12 in the Appendix display the SCD curves for all the investigated winter seasons 2015/2016 to 2019/2020.

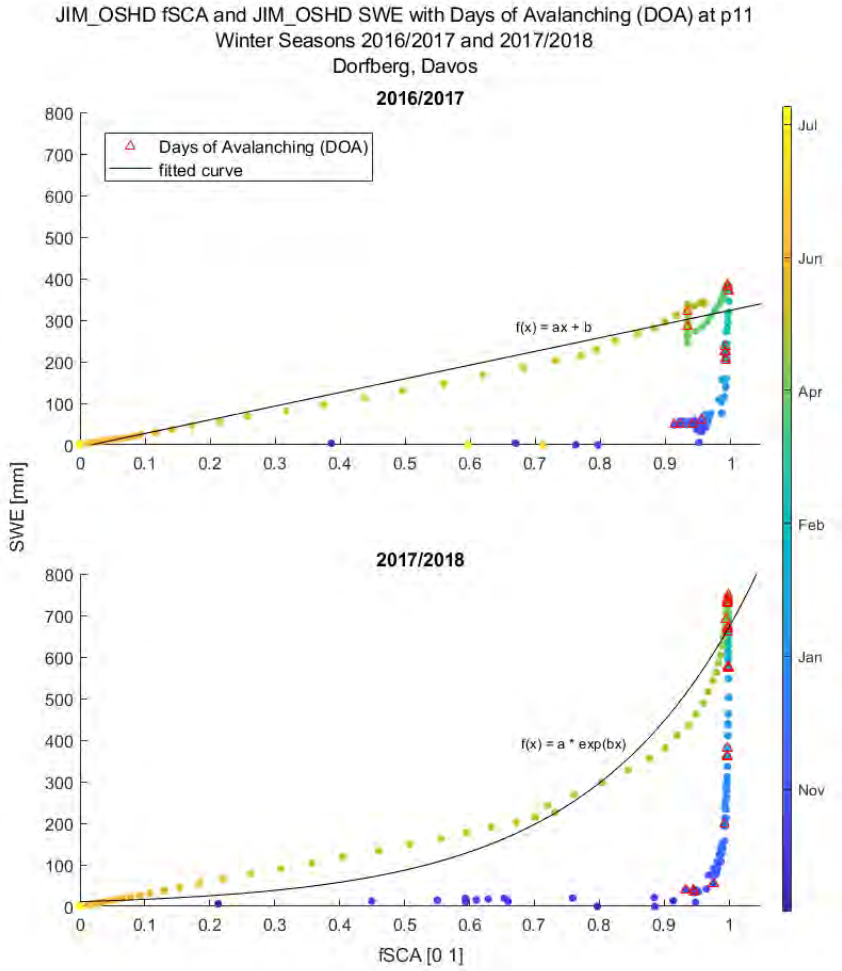

FIGURE 4.6: JIM_OSHD fSCA [0 1] with JIM_OSHD SWE [mm] at tile p11 for winter seasons 2016/2017 and 2017/2018. Each coloured data point refers to a day of the year, while the days of avalanches (DOA) are marked with red triangles. The solid black curves show a linear curve for 2016/2017, and an exponential curve for 2017/2018 fitted through the ablation stages of the fSCA-SWE link.

Figure 4.6 displays JIM_OSHD fSCA on the x-axis and JIM_OSHD SWE on the y-axis for two winter seasons 2016/2017 and 2017/2018, including fitted curves for the ablation stage. For both years, the early season SWE equalled almost zero, while fSCA increased steadily (accumulation stage). At the point where fSCA reached its maximum value of about 0.98, SWE started to increase sharply. Some of the wet-snow avalanche events were triggered during the pronounced increase in SWE. Another cluster of wet-snow avalanches occurred at the maximum values of both fSCA and SWE. At this point the wet-snow avalanches released over several consecutive days. After this point in time, no more avalanches were recorded. Then, fSCA and SWE started to decrease (ablation stage) until they reached their initial point of zero again. As the ablation stages vary from year to year, functions (black solid curves) were fitted through the data. Our qualitative analyses revealed that either linear functions or exponential functions fitted best. For the winter season 2016/2017, after reaching a maximum SWE of 384.75 mm, a linear polynomial curve, $f(x) = a \times x + b$, with $a = 329.4$ and $b = -5.57$ was fitted to the data. On the other hand, for winter season 2017/2018, after reaching a maximum

SWE of 749.58 mm, an exponential function, $f(x) = a \times exp^{b \times x}$, with $a = 11.25$ and $b = 4.09$ was fitted to the data.

Furthermore, there were characteristic patterns between fSCA and SWE: Mid of April 2017, shortly after the beginning of the melting season, i.e. when fSCA and SWE already start to decrease, SWE suddenly increases again, indicating that mass, originated either from rain or snowfall, is added (Figure 4.6 top). This was also revealed in Figure 4.2.2, where fSCA at higher elevation remained unaltered during that time, even though a snowfall event occurred. Then, fSCA increases too for a few days, before both SWE and fSCA follow their almost linear decreasing path again. It is interesting, that two avalanches released during this pronounced increase of SWE and almost constant fSCA. This behaviour could indicate a relation between wet-snow avalanche activity and high fSCA and SWE.

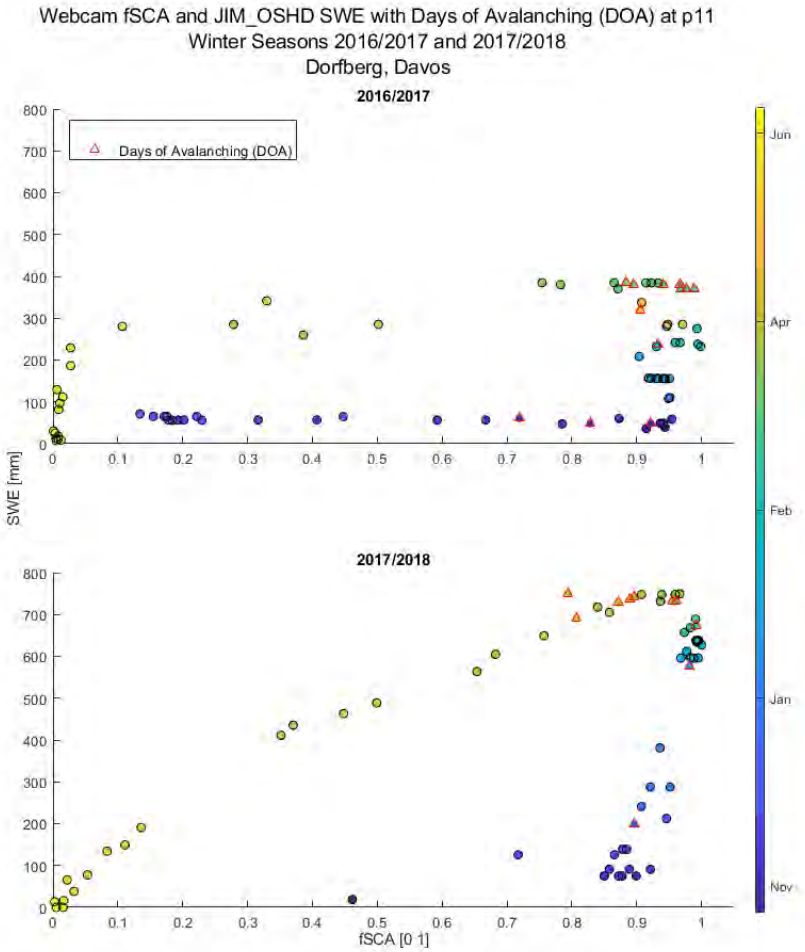

FIGURE 4.7: Webcam fSCA [0 1] with JIM_OSHD SWE [mm] at tile p11 for winter seasons 2016/2017 and 2017/2018. The webcam fSCA is calculated with the blue band algorithm of Salvatori et al. (2011). Each coloured data point refers to a day of the year, while the days of avalanches (DOA) are marked with red triangles.

In Figure 4.7 JIM_OSHD SWE and avalanche data of the Dorfberg site for the two winter seasons 2016/2017 and 2017/2018 together with webcam fSCA-data (algorithm of Salvatori et al. (2011)) from the Dorfberg are shown. At first glance, it was difficult to identify a typical SCD curve for winter season 2016/2017, as the webcam fSCA-data was rather scattered. In contrast, the winter season 2017/2018 revealed a characteristic SCD curve pattern of the webcam fSCA-SWE relation. Still, most wet-snow avalanches occurred after fSCA and SWE have reached their maximum value. However, the days of avalanches were less clustered at maximum webcam fSCA and JIM_OSHD SWE compared to the JIM_OSHD fSCA and SWE relationship shown in Figure 4.6.

4.3.1 Modelling the Onset of Wet-Snow Avalanche Activity Cycles

For the Dorfberg site we established a simple model with the aim to detect and model the Onset of Wet-Snow Avalanche Activity Cycles ($OWSAAC$) with data from the JIM_OSHD model. For the evaluation we calculated confusion matrices and considered the following quality metrics: false alarm ratio (FAR), probability of detection (POD), probability of false detection (POFD), Accuracy (Acc), and Hanssen Kuipers Score (HK).

TABLE 4.5: Combinations of $range_{sca}$ and $range_{swe}$ with best quality metrics and score for the Dorfberg site. The metrics and score include False Alarm Ratio (FAR), Probability of Detection (POD), Probability Of False Detection (POFD), Hanssen Kuipers Score (HK) and Accuracy (Acc). In total the simulation model was run with 9211 combinations for $range_{sca}$ and $range_{swe}$.

$range_{sca}$	$range_{swe}$	FAR	POD	POFD_rate	HK	acc
0.0006	0.0250	0.6250	0.6522	0.0167	0.6355	0.9783
0.0006	0.0260	0.6250	0.6522	0.0167	0.6355	0.9783
0.0006	0.0270	0.6250	0.6522	0.0167	0.6355	0.9783
0.0006	0.0280	0.6000	0.6400	0.0160	0.6240	0.9783
0.0006	0.0290	0.6000	0.6400	0.0160	0.6240	0.9783

Out of the 9211 possible $range_{sca}$-$range_{swe}$ combinations, all aiming to capture the $OWSAAC$, we identified five range combinations that performed best. These $range_{sca}$-$range_{swe}$ combinations are depicted in the first two rows in Table 4.5. For a better illustration of these results, let us imagine a bounding box drawn around the maximum values of fSCA and SWE-data for $range_{sca}$ = 0.0006 and $range_{swe}$ = 0.028. The $range_{sca}$ and $range_{swe}$ can be understood as width (x-axis) and height (y-axis) of the bounding box (see Figure 3.7 for illustration). For that combination, the bounding box included all data points with normalized fSCA values higher than 1 - 0.0006 = 0.9994 and normalized SWE values higher than 1 - 0.028 = 0.972. This was done in every year separately. Thus, all the data points located within this bounding box were modelled as an $OWSAAC_{sim}$. Then, we compared the obtained $OWSAAC_{sim}$ with the $OWSAAC_{true}$ by generating confusion matrices and calculating quality metrics for each of the 9211 combinations. For $range_{sca}$ = 0.0006 and $range_{swe}$ = 0.025 to 0.029 we received best quality metrics. Furthermore, the Receiver Operating Characteristic (ROC) curve identified this combination as the most appropriate one, with an Area Under Curve (AUC) of 0.8178. The ROC curve with all simulation combinations is shown in the Appendix (Figure A.13). For the five best combinations, we received identical accuracies)0.9783),

while the other metrics vary slightly. We obtained a fair POD (0.6522), a low POFD (0.0167), and a Hanssen Kuipers score of 0.6355 for the $range_{sca}$ = 0.0006, combined with the $range_{swe}$ = 0.025 to 0.027. Compared to the combinations 0.0006 ($range_{sca}$), and 0.028 to 0.029 ($range_{swe}$), POD (0.64) and HK (0.624) were lower. However, these combinations displayed a slightly higher POFD rate (0.0167).

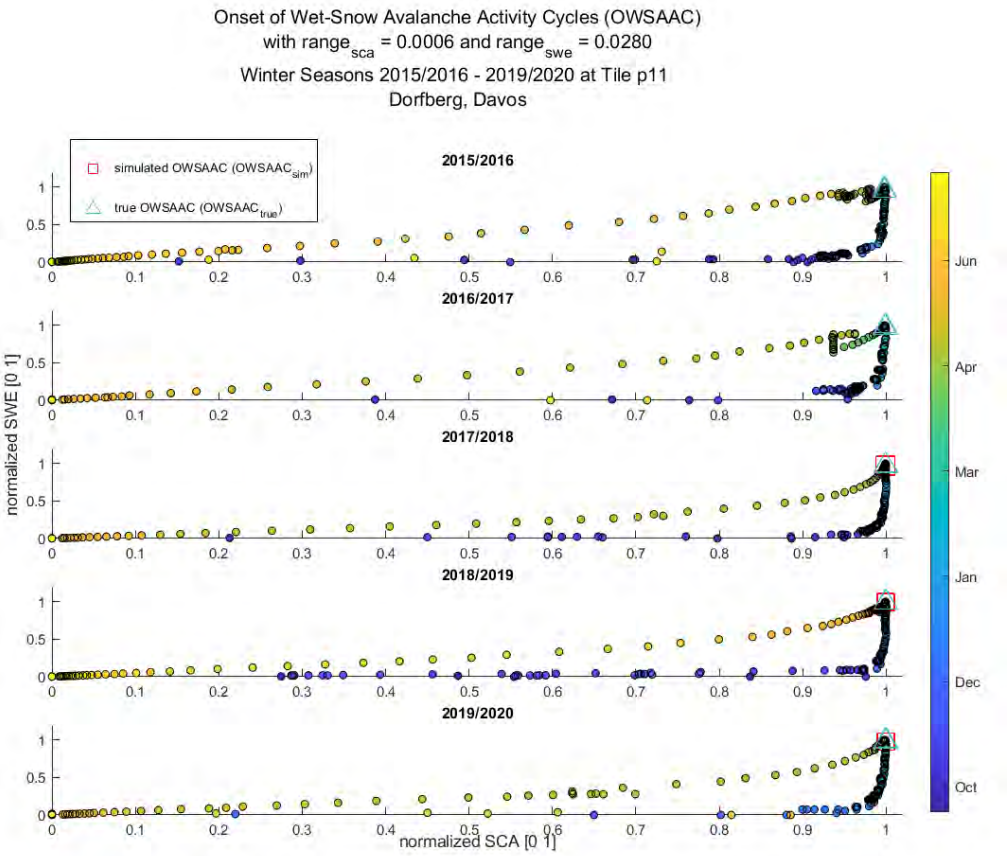

FIGURE 4.8: Simulation run with $range_{sca}$ = 0.0006 and $range_{swe}$ = 0.028 for tile p11 at the Dorfberg site. The coloured data points correspond to the normalized fSCA and SWE values obtained for every day within the investigated winter seasons 2015/2016 to 2019/2020. The blue triangles mark the true onset of wet-snow avalanche activity cycle $OWSAAC_{true}$, and the red squares refer to the modelled onset of wet-snow avalanche activity cycle $OWSAAC_{sim}$.

Figure 4.8 applies the range combinations with $range_{sca}$ = 0.0006 and $range_{swe}$ = 0.028 on the past winter seasons. The coloured data points correspond to the normalized fSCA and SWE values, obtained for every day within the investigated winter seasons. The blue triangles mark the true onset of wet-snow avalanche activity cycle $OWSAAC_{true}$, and the red squares shows the modelled onset of wet-snow avalanche activity cycle $OWSAAC_{sim}$. For winter seasons 2017/2018 to 2019/2020 the modelled $OWSAAC$ coincided well with the true $OWSAAC$. This was not the case for winter seasons 2015/2016 and 2016/2017. During these years the conditions set in Section 3.5 for defining the $OWSAAC_{sim}$ were not met by both the normalized fSCA values and SWE values. Thus, there were no dates where the values for the fSCA condition and SWE

condition have intersected and thereby, according to our definition, the model could not detect an $OWSAAC_{sim}$.

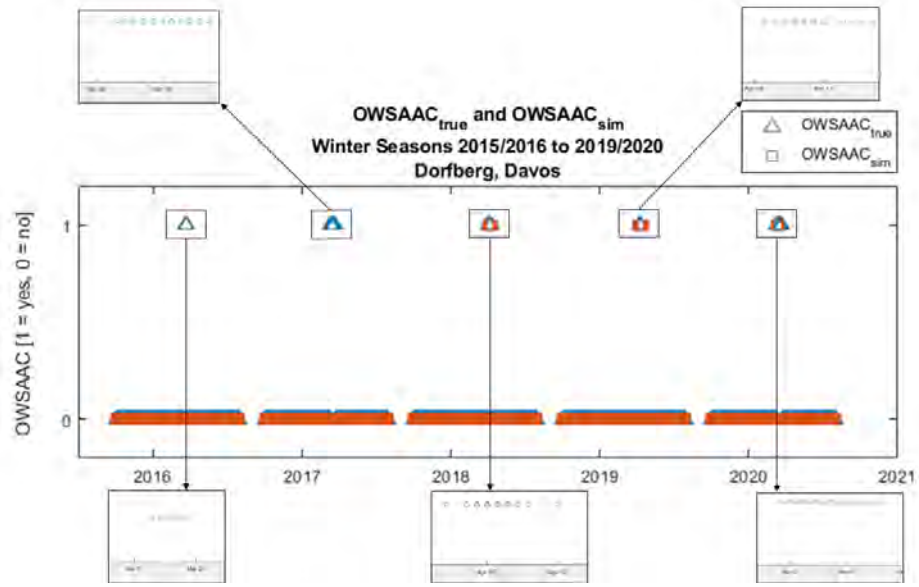

FIGURE 4.9: $OWSAAC_{true}$ (blue triangles) and $OWSAAC_{sim}$ (red squares) shown for winter seasons 2015/2016 to 2019/2020 at the Dorfberg site. $OWSAAC_{sim}$ was calculated with $range_{sca}$ = 0.0006 and $range_{swe}$ = 0.028. The insertions show the zoomed-in $OWSAAC$s for every winter season.

In more detail the true and modelled $OWSAAC$ over the investigated winter seasons 2015/2016 to 2019/2020 are shown in Figure 4.9. Again, $OWSAAC_{true}$ are marked as blue triangles and $OWSAAC_{sim}$ as red squares. The insertions show the zoomed-in $OWSAAC$ period for every season. The duration of these periods varied from one year to another, with lengths between five and fourteen consecutive days.
Our model failed to detect the $OWSAAC$ in winter seasons 2015/2016 and 2016/2017, but successfully detected the $OWSAAC$ in winter seasons 2017/2018 to 2019/2020. Focusing on the insertions, we see that $OWSAAC_{sim}$ correctly identified the first day of the true avalanche cycle for winter seasons 2018/2019 and 2019/2020. Also, in the winter season of 2017/2018 the $OWSAAC_{sim}$ was detected, even though the model displayed the $OWSAAC_{sim}$ three days earlier than in reality. Nonetheless, for operational use, a premature detection of avalanche cycles is more valuable, than a belated one.

TABLE 4.6: Simple model run with $range_{sca}$ = 0.0006 and $range_{swe}$ = 0.028 that performed best (i.e. the highest POD, HK and Accuracy, and lowest POFD) for the Dorfberg site, applied on the webcam fSCA-data of tile p11.

Tile	$range_{sca}$	$range_{swe}$	FAR	POD	POFD	HK	Acc
p11	0.0006	0.028	0.9545	0.5	0.06	0.44	0.9375

To test the best combinations of $range_{sca}$ and $range_{swe}$ trained for the JIM_OSHD parameters at the Dorfberg site, we ran the simple model with $range_{sca}$ = 0.0006 and $range_{swe}$ = 0.028 for the webcam fSCA at the same site. Table 4.6 displays the evaluation of the simple model performance, when working with the same ranges but with the webcam fSCA-data instead of the JIM_OSHD fSCA-data. POD (0.5) was not better than chance, also the HK score (0.44) was low. However, POFD (0.06) indicated that the model was rather conservative, as it rather underestimated than overestimated the $OWSAAC$.

TABLE 4.7: Best combination of $range_{sca}$ = 0.0006 and $range_{swe}$ = 0.028 trained for the Dorfberg and applied on all 36 tiles of the Dischma area. Eight tiles for which the combination achieved the highest quality metrics are shown. The metrics and score include the False Alarm Ratio (FAR), Probability of Detection (POD), Probability Of False Detection (POFD), Hanssen Kuipers Score (HK) and Accuracy (Acc).

Tile	$range_{sca}$	$range_{swe}$	FAR	POD	POFD	HK	Acc
p20	0.0006	0.028	0.9565	0.6667	0.0485	0.6182	0.9501
p12	0.0006	0.028	0.9565	0.6000	0.0470	0.5530	0.9501
p5	0.0006	0.028	0.9565	0.5000	0.0486	0.4514	0.9484
p14	0.0006	0.028	0.9565	0.5000	0.0501	0.4499	0.9484
p18	0.0006	0.028	0.9565	0.4000	0.0487	0.3513	0.9468
p26	0.0006	0.028	0.9565	0.4000	0.0487	0.3513	0.9468
p10	0.0006	0.028	0.9565	0.3750	0.0472	0.3278	0.9451
p33	0.0006	0.028	0.9565	0.3750	0.0472	0.3278	0.9451

Additionally, we applied the simple model with $range_{sca}$ = 0.0006 and $range_{swe}$ = 0.028 to the JIM_OSHD-data from the Dischma area to investigate model performance in another area, where altitude, topography, and aspect of the slopes are different. Table 4.7 depicts the model performance at the Dischma area for the eight tiles with the highest quality metrics. Overall, the quality metrics revealed high accuracies and moderate POD. However, the POFD and HK showed that the simple model performed rather poor at the Dischma area. Also, the FAR (0.9565) indicated the limited reliability when applying the simple model to other areas. The best quality metrics were achieved for tile p20, with 0.6667 (POD), 0.0485 (POFD), 0.6182 (HK). This means out of all 36 investigated tiles in the Dischma area, $OWSAAC_{sim}$ matched best with $OWSAAC_{true}$ in tile p20.

Chapter 5

Discussion

This Chapter is structured within the framework of the three main research objectives: First, we discuss webcam fSCA retrieval and the performance of the applied snow classification algorithms of Salvatori et al. (2011), Härer et al. (2013) and Härer et al. (2016). Then, we examine the comparison and correlation analysis between webcam fSCA and JIM_OSHD fSCA, and UAV HS and JIM_OSHD HS. Last, we address the link between fSCA, SWE and wet-snow avalanche activity and discuss the performance and limitations of the established simple model to detect the onset of wet-snow avalanche activity cycles.

5.1 Snow Cover Classification of Webcam Images

According to our validation analysis and the evaluated quality metrics (Table 4.2) the algorithm of Salvatori et al. (2011) performed best and thus is considered to be the most reliable algorithm for the Dorfberg site. Still, we identified misclassification problems similar to other studies (Dizerens, 2015; Fedorov et al., 2015; Härer et al., 2013, 2016; Portenier et al., 2019; Salvatori et al., 2011; Salzano et al., 2019). Misclassifications occurred predominately during poor weather conditions causing cloudy and foggy scenes with low illumination. Additionally, the webcam algorithms faced some problems when detecting shaded snow near buildings, infrastructure or close to irregularities in terrain (rock, trees, shrubs) (Figure 4.1). Similar to the findings of Portenier et al. (2019), we observed that this resulted in an underestimation of fSCA when applying the algorithm of Salvatori et al. (2011). Furthermore, likewise to Portenier et al. (2019) we demonstrated that the PCA algorithm of Härer et al. (2013) performed well, too. However, for the algorithm of Härer et al. (2013) many misclassifications towards the margin of the FOV have led to a reduced sample size of correctly classified webcam images (Table 4.1). Forested areas at the left and right margin of the FOV might have caused less distinct PC analyses. Similar to Dizerens (2015) we observed that the PCA algorithms had difficulties to detect fSCA in areas further afar from the webcam installation.
Nevertheless, the offset was smaller between the absolute fSCA values retrieved by PCA algorithm and the JIM_OSHD fSCA, compared to the offset between the fSCA retrieved by the algorithm of Salvatori et al. (2011) and JIM_OSHD fSCA. In contrast, the PCA algorithm with rock thresholding (Härer et al., 2016) performed rather poor for the Dorfberg site. This is inconsistent with Härer et al. (2016), who tested their algorithm at the Schneefernerkopf near Zugspitzplatt catchment in Austria. At this site the PCA algorithm with rock thresholding was able to separate sunny and shaded snow from other surfaces with a similarly high accuracy as the blue band algorithm of Salvatori et al. (2011). A reason for the poor performance might be, that the topography and land surfaces at the testing site of Härer et al. (2016) was very different from the Dorfberg

site. With a maximum altitude of 2875 m a.s.l., the Schneefernerkopf is abounded with rocks without any vegetation present. The Dorfberg site on the other hand includes altitudes between 1558 m a.s.l. to 2469 m a.s.l., with some partly forested areas. The poor performance of the rock thresholding algorithm emerged also in the correlation analysis. Since we had to disregard many misclassified images retrieved with the algorithms of Härer et al. (2013, 2016) resulting in data gaps, we suggest enhancing the image quality and the classification routine by further image pre-processing strategies.

5.1.1 Summary

We demonstrated that the technique of image composites as a part of image pre-processing strategies was a simple and easy-to-handle technique to avoid misclassifications. We argued that having one image per day composited of eight images, could result in positive impacts on the snow classification performance, since fog, cloud, and illumination issues were minimized (Figure 3.4 and 3.5). However, shadowed snow caused by the presence of buildings, infrastructure, and irregularities in terrain, were likely to remain and resulted in less correctly snow classified pixels (Figure 4.1. Thus, additional image processing techniques would further increase the correct snow classification rate. There are various such approaches which are either applied prior to the classification process or as a part of the classification process itself.
Along with image composites, other pre-classification approaches, for instance image editing processes, exist. These include the application of different colour spaces (e.g. YUV) (Dizerens, 2015), or adjustments of the brightness or tone in image editing programs (Kepski et al., 2017). Future work will be needed in order to find the couplings between image improvement methods and image composites, which yield optimal classification results.
During the image classification process other snow classification algorithms could be implemented and tested in future research. Promising methods include NDSI indexing (Dozier, 1989; Hall et al., 2001) or machine learning algorithms that are trained for image classification (Das, 2017). Moreover, other supervised methods, and unsupervised classification methods (Kepski et al., 2017), e.g. the spectral similarity algorithm of Salzano et al. (2019), could be used.
Regardless of the chosen algorithm, we suggest to review and remove the misclassified images originating from low illuminated composited images, images with cloud or fog covering the scenery, or images where snow cover was falsely classified. Although this is a time-consuming task, disregarding images in our opinion is the most reliable technique to assure reliable webcam fSCA-data retrieval. Furthermore, algorithm performance is very likely site specific, thus applying only a single algorithm for a large investigated area may result in poor webcam fSCA retrieval. In our future work we will apply the algorithm of Salzano et al. (2019) at the Dorfberg site and other areas and compare the resulting webcam fSCA-data with the other three algorithms. Therefore, we state that working with different approaches and algorithms may be crucial for retrieving an optimal snow classified optical webcam image.

5.2 Comparison between JIM_OSHD Model and Snow Parameters

By comparing and validating JIM_OSHD modelled fSCA and HS data with webcam fSCA and UAV HS-data, we address our second research objective. Overall, the JIM_OSHD model had the tendency to model higher fSCA and HS values, compared to webcam fSCA and UAV HS. First, we focus on the comparison with UAV HS.

We consider the UAV HS-data to represent approximately the ground truth, as the data was very accurate with its high spatial resolution of 0.3 m (Eberhard et al., 2020). Hence, the JIM_OSHD model rather overestimated HS (Figure 4.2.3). For several tiles, the offset between UAV HS and JIM_OSHD HS was substantial, moreover, the JIM_OSHD HS values lay outside one standard deviation of the UAV HS. These differences might decrease if more data of different UAV flights over larger investigated areas were available. This would allow the HS-data to be compared at different points in time and over a larger area, which could give a better picture of the JIM_OSHD model performance. But since UAV flights are expensive in time and cost, data of only few days were available from which just one in April 2017 was used in this study (Eberhard et al., 2020). Furthermore, the UAV covered only a restricted area, due to technical and legal limitations (Eberhard et al., 2020). As the data were recorded in spring, when the radiation is already increasing, HS can vary according to the exposure of the hill slopes. Therefore, further investigations and comparisons with UAV data at different days during the winter season and for different elevation zones could provide an added value to the further development and validation of the HS parameter in the JIM_OSHD model.

For the following the webcam fSCA is considered to represent approximately the ground truth fSCA, even though this technique had also limitations (Section 5.1.1). When comparing JIM_OSHD fSCA-data with webcam fSCA-data, an offset between the fSCA values was visible (Figure 4.3). JIM_OSHD fSCA displayed higher values than webcam fSCA during almost all the seasons and tiles and thus rather overestimated fSCA. Even though the offsets were highest for webcam fSCA calculated with the algorithm of Salvatori et al. (2011), our correlation analyses showed highest and statistically significant correlation values for the blue band algorithm of Salvatori et al. (2011) as there were the least data gaps caused by pixel misclassifications. We demonstrated that this offset was especially pronounced for lower elevation zones of the FOV (p12, p13), and during the beginning and end of the season (Figure 4.4). At lower elevation, the webcam technique has partly underestimated snow cover, as trees have created shadows an thus the snow-covered pixels were not correctly classified as snow-covered. Still, we argued, that during the beginning and end of season the JIM_OSHD model overestimated fSCA-data and thus, also the melt-out dates lagged in time (Table 4.4). Additionally, the different spatial resolutions may have had an impact on the offset, too: With its coarse resolution of $1km^2$ the JIM_OSHD model seemed to be less suitable for detecting dynamics of snow parameters in a high spatial resolution. On the other hand, if the webcam snow classification succeeded, it was able to detect fSCA even at small spatial scale but with more missing data. Hence, it was a challenge to validate the JIM_OSHD model with the webcam fSCA cut to the tiles, as their spatial coverage of the investigated area were not the same. Furthermore, we have to keep in mind that the webcam technique is also only an approximation to ground truth fSCA-data. Thus, we suggest that for validating JIM_OSHD fSCA-data with webcam fSCA-data, the location

and FOV of the webcam should be well-chosen in order to assure maximum coverage of the investigated area.

Missing webcam data was an issue, especially when JIM_OSHD fSCA was correlated with webcam fSCA (Table 4.3). For the images classified with the algorithms of Härer et al. (2013, 2016), we had to disregard many images, leading to small sample sizes. According to Bujang et al. (2016) a small sample size results in lower correlation coefficients. Moreover, regarding the correlation coefficients, the rock thresholding algorithm of Härer et al. (2016) performed even worse than the PCA algorithm of Härer et al. (2013), as their webcam fSCA values were unreasonable high and remained unaltered over time (Figure 4.3). In addition to the small sample size of Härer et al. (2016), misclassifications in forested areas probably also had an influence on the correlation coefficients. We noticed that at tile p6, where no vegetation is present, the algorithm of Härer et al. (2016) performed better (Figure A.2). On the other hand, for tile p12, where 33% of the area is forested, the algorithm of Härer et al. (2016) differed noticeably from the other algorithms, as it failed to detect seasonal patterns in fSCA. For this tile p12, fSCA is 1 almost always, without any variation in time (Figure A.5). The correlation coefficients (Table 4.3) also showed this tendency: Although still low, p6 showed higher correlation coefficients between webcam fSCA of Härer et al. (2016) and JIM_OSHD fSCA, while the other correlation coefficients for tile p7, p11, p12 and p13 showed values close to zero.

Summary

Overall, we showed that webcam fSCA and UAV HS were a valid tool for comparing and validating snow parameters of the JIM_OSHD and both can be considered as ground truth. We argued that webcam fSCA-data better depicted short-term events, e.g. snowfalls and melt-out dates, due to their high spatial resolution. However, the JIM_OSHD fSCA show these events as well, but less precise and with some delay, especially for lower elevations. Our analysis showed, that the fSCA values over the winter seasons showed similar courses, regardless whether the fSCA-data was retrieved by the webcam approach with the algorithm of Salvatori et al. (2011) or the JIM_OSHD model. Concerning the other algorithms (Härer et al., 2013, 2016), forested areas may be a reason why the PCA algorithms performed less well at the Dorfberg site, resulting in large data gaps. Thus, for the Dorfberg site we suggest applying the snow classification algorithm of Salvatori et al. (2011), as it performed best for every tile at every elevation zone with any kind of land surface type, both forested or rocky. Moreover, we had to disregard the fewest number of images, giving us a nearly continuous fSCA data set. However, shaded snow caused a substantial offset in fSCA, which has to be taken into account when interpreting and working with the data. Also, it is likely that for other sites, bare of vegetation, the PCA algorithms of Härer et al. (2013, 2016) may perform just as good as the algorithm of Salvatori et al. (2011) and thus be a reasonable choice. We claimed that UAV HS-data and webcam fSCA-data were valid parameters to validate the snow cover model JIM_OSHD with. Nevertheless, for a comprehensive validation and in order to reduce uncertainty of the parameters fSCA, SWE and HS of the JIM_OSHD model, it would be crucial to validate the model with additional data sources. For instance, with *in-situ* measurements (Eberhard et al., 2020; Johnson et al., 2011; Morin et al., 2012) or non-invasive remote sensing techniques, i.e. TLS, radar or satellite imagery (Dietz et al., 2012; Grünewald et al., 2015; Helbig et al., 2017; Hüsler et al., 2012; Machguth et al., 2006).

We argued that for the investigation of larger areas (>1km^2) the JIM_OSHD modelled fSCA-data should be preferred. Also, when investigating seasonally changing patterns over several years, JIM_OSHD fSCA may be the better and more reliable choice for data retrieval, as it has fewer data gaps. When it comes to the investigation of short-term events at specific slopes with areas $\leq 1km^2$, we claimed that webcam fSCA was a more powerful alternative and may complement snow cover models. Nonetheless, we have to keep in mind, that filtering webcam fSCA-data was time-consuming and resulted in large data gaps, which appeared to be inappropriate for investigating seasonal changing patterns.

5.3 Link between fSCA, SWE and Wet-Snow Avalanches

The third research objective addressed the link between fSCA and SWE of the JIM_OSHD model and wet-snow avalanche activity. First, we established a link between fSCA, SWE and the days of avalanches (DOA) (Section 4.3), and second, we developed a simple model with the aim to determine the onset of wet-snow avalanche activity (Section 4.3.1). For this we required data at daily resolution. From the preceding analyses we concluded that the JIM_OSHD model fulfilled these requirements better, thus we decided to work with JIM_OSHD modelled parameters instead of webcam fSCA.

The link between fSCA-SWE shown as a SCD curve in Figure 4.6, revealed clear seasonal changes in snow cover dynamics. Avalanche days (DOA) were often located at similar points in time, i.e. in the upper right part of the SCD curve, where both fSCA and SWE were maximal, prior to the linear or exponential decrease (ablation stage) of SWE. These variations within the SCD curve implied the existence of a hysteresis curve, which is defined as a curve that starts and ends at the same point, whereas the path in between is not identical (Fassnacht et al., 2016; Luce et al., 1999; Magand et al., 2014). Furthermore, we revealed that the ablation stage either came along with a linear and thus faster decrease in fSCA, or an exponential and thus slower decrease in fSCA. Relating this observation with the findings of Rango et al., 1982, where they showed that a fast decrease in fSCA reflected either a shallow snow cover or high melt rates, whereas a slow decrease in fSCA resulted either from a deep snow cover or slow melt rates, inferences about the winter seasons can be drawn, by only analysing SCD curves with two parameters. Thus, we argue that a linear decrease could be an indicator for a season below average snow depth (2016/2017), while an exponential curve shape of the ablation stage could be characteristic for a winter with average or above average snow depth (2017/2018).

For the detection of the $OWSAAC$ the Hanssen Kuipers score (0.635) and the accuracy (0.97) were rather high (Table 4.5). However, this might be misleading as for the accuracy the events (onset) and non-events (no onset) are treated equally. Thus, the accuracy of the simple model has limited explanatory power, since it is dominated by the high number of correctly detected non-events, compared to the small number of possible $OWSAAC$ days. With a POD of 65.22%, more than two-thirds of all $OWSAAC_{true}$ events during the winter seasons 2015/2016 to 2019/2020 were correctly detected. Furthermore, the POFD (0.0167) was rather low, showing very few false detected events. On the contrary, we calculated a high FAR (0.625). Having high POD values and low POFD values on the expense of high FAR values is a common challenge that is often faced in avalanche research (Bellaire et al., 2017). We claimed that the FAR

could be reduced by specifying the dates of the true $OWSAAC$, or by considering only winters with average or above average snow depth.
The simple model did not detect an $OWSAAC$ in winter seasons 2015/2016 and 2016/2017. As previously discussed, these winter seasons were very short and below average snow depth (Zweifel et al., 2017, 2016), which could have been one of the reasons why the simple model performed less well. Hence, we suggest to further investigate the JIM_OSHD model with particular focus on fSCA and SWE-data for below average winters.

The results of the quality metrics have shown that the established simple model was not better than chance (POD 0.5) when detecting the $OWSAAC$ for the webcam fSCA-data at the Dorfberg site. The quality metrics indicated poorer results (POD 0.37 to 0.66) for the Dischma area even for the eight best performing tiles when compared to the Dorfberg site. Thus, the applicability of the simple model to other areas is limited and comes with high uncertainties. However, the similar aspect in p20 (Dischma) and p11 (Dorfberg) could have been a reason for the good performance (POD 0.66 and POFD 0.0167) of the simple model for this tile in the Dischma area. Applying and evaluating the simple model for other similarly exposed hill slopes could be addressed in future studies in order to show if there is a relation between aspects and performance of the model. Furthermore, future work could train the simple model for other slopes with different aspects where avalanche activity is well documented.

Our simple model was established and trained on the basis of fSCA and SWE-data from the JIM_OSHD model in order to detect past $OWSAAC$. Hence, the simple model underlay a *hindcasting* technique, as the JIM_OSHD model only provides historic data (Section 1.2.1). The conditions set for fSCA and SWE-data and best combinations of $range_{sca}$ and $range_{swe}$ were identified in order to detect $OWSAAC$ in the past. Thus, our simple model can be used for hindcasting, i.e. identify past $OWSAAC$ events, but cannot be used for forecasting, i.e. predict future $OWSAAC$ events. However, to forecast the $OWSAAC$ we could use lower elevation tiles to predict wet-snow avalanches at higher elevations: During the melt season in spring, snow cover first to decrease at lower elevation, before fSCA starts to decrease at higher elevation (Section 4.2.2). Thus, the decreasing fSCA triggers wet-snow avalanches to occur first at lower elevation before wet-snow avalanches are triggered at higher elevation, evoking an $OWSAAC$- cascade from lower to higher elevation. Thus, detecting the $OWSAAC$ for JIM_OSHD tiles at lower elevation could assist avalanche forecasters to predict the $OWSAAC$ also at higher elevations.
However, at the Dorfberg site almost all wet-snow avalanches released at the same elevation zone around 2100 m a.s.l. (Section 4.3). Consequently, the detection of the aforementioned $OWSAAC$- cascades were not possible, as all the wet-snow avalanches released in tile p11. Thus, it would be important to investigate other areas where wet-snow avalanches release at different elevation zones.

Summary

We have shown that the link between fSCA, SWE and wet-snow avalanches underlay seasonal patterns within the SCD curve as wet-snow avalanches were likely to occur when the fSCA and SWE-data reached their maximal values. Furthermore, the ablation stage can give more information about the state of the snow cover and melt rates and thus give indications about the winter seasons. Additionally, we presented a simple model based on JIM_OSHD modelled data and trained for the Dorfberg site, that can

be considered as a valuable tool for detecting and defining the onset of wet-snow avalanche activity cycles for past winter seasons. Although, the simple model came with limitations as it only included fSCA and SWE-data, we suggested applying the model to sites with an aspect similar to the trained site, in order to find possible links. Furthermore, adding new parameters, i.e. air temperature or precipitation could refine the simple model. Such refinements may improve the detection of historic $OWSAAC$, and together with identifying $OWSAAC$- cascades from lower to higher elevation zones, it could assist avalanche forecasters to predict wet-snow avalanche activity.

Chapter 6

Conclusion

In this study we showed the possibilities and limitations of using snow classification algorithms for webcam images as an alternative approach to retrieve fSCA-data. We compared and validated the commonly used JIM_OSHD snow cover model with the webcam fSCA. For that we utilised three pixel-based snow classification algorithms for webcam images (Salvatori et al. (2011), Härer et al. (2013, 2016)) and evaluated their performance at the Dorfberg site. Furthermore, we analysed two parameters, fSCA and HS of the JIM_OSHD model and compared these with webcam fSCA and UAV HS-data. Then, by linking seasonal dynamics of JIM_OSHD fSCA and SWE to wet-snow avalanche activity, data showed that wet-snow avalanches occurred predominately at the point where both fSCA and SWE reach their maximal value, just before they start to decrease. Finally, in order to determine the onset of wet-snow avalanche activity cycles in the past, we presented a simple model and evaluated its performance also by applying the best percentile ranges of maximum fSCA and SWE to the Dischma area.

Out of the three snow classification algorithms, Salvatori et al. (2011) performed best. With high averaged accuracy (0.91), POD (0.87), and POFD (0.08), the algorithm of Salvatori et al. (2011) was the most reliable for all land surfaces with the least data gaps over the investigated winter seasons 2015/2016 to 2019/2020. Our qualitative analyses revealed that the webcam fSCA technique was most reliable during peak winter at high elevation zones, as there were less illumination issues as well as trees or other obstacles present causing shadows. Overall, the JIM_OSHD model overestimated fSCA as there was a substantial offset between JIM_OSHD fSCA and webcam fSCA. This offset was most pronounced during the beginning and end of season, with the result that the JIM_OSHD model showed delayed melt-out dates compared to the webcam retrieved fSCA values. We presented that webcam fSCA-data could be a reasonable technique to validate snow cover models or could even be an alternative to snow cover models when analysing seasonal trends where site specific and high spatial resolution is needed. However, when investigating larger areas and seasonally changing patterns, the JIM_OSHD model should be preferred as there are no data gaps.
Furthermore, as JIM_OSHD HS lay within two standard deviations of UAV HS-data, we argued that additional data of different flights covering larger areas would be required for a comprehensive assessment and improvement of modelled HS.
These findings in fSCA and HS provide a basis for the refinement of the JIM_OSHD model and could constitute the object of future studies.

The link between JIM_OSHD fSCA, SWE and avalanche activity casted a new light on the understanding of wet-snow avalanches. Analyses of the snow cover depletion curves for the Dorfberg site were consistent with the findings from other studies and demonstrated that the slope and type (linear or exponential fit) of the ablation curve allowed inferences about the state of the snow cover and melt rates. Furthermore, we have confirmed our hypothesis that wet-snow avalanches were likely to be triggered

when both fSCA and SWE have reached their maximal value prior to the ablation stage. On this basis, we established a simple model, with the aim to simulate the historic *OWSAAC* by defining a percentile range of maximum fSCA and SWE where wet-snow avalanches were likely to occur. By evaluating over 9000 range combinations, the best quality metrics were obtained for percentile ranges of 0.06% for maximum fSCA and 2.5 to 2.9% for maximum SWE values. With these percentile range combinations the *OWSAAC*s were well detected for extensive and winters with average or above average snow depth (2017/2018 to 2019/2020) and less well for short winters with snow depths below average. By applying the best range combination to the Dischma area, the simple model revealed that tiles with similar exposed hill slopes yielded the best performance results. Still, future research is needed in order to test these initial percentile ranges, to refine the simple model by including additional parameters for larger investigated areas and to identify *OWSAAC*- cascades from lower to higher elevation zones. This would contribute to a more precise detection of historic *OWSAAC* and could improve wet-snow avalanche forecasting.

Appendix A

Additional Figures and Tables

A.1 Methods

A.1.1 Working Process

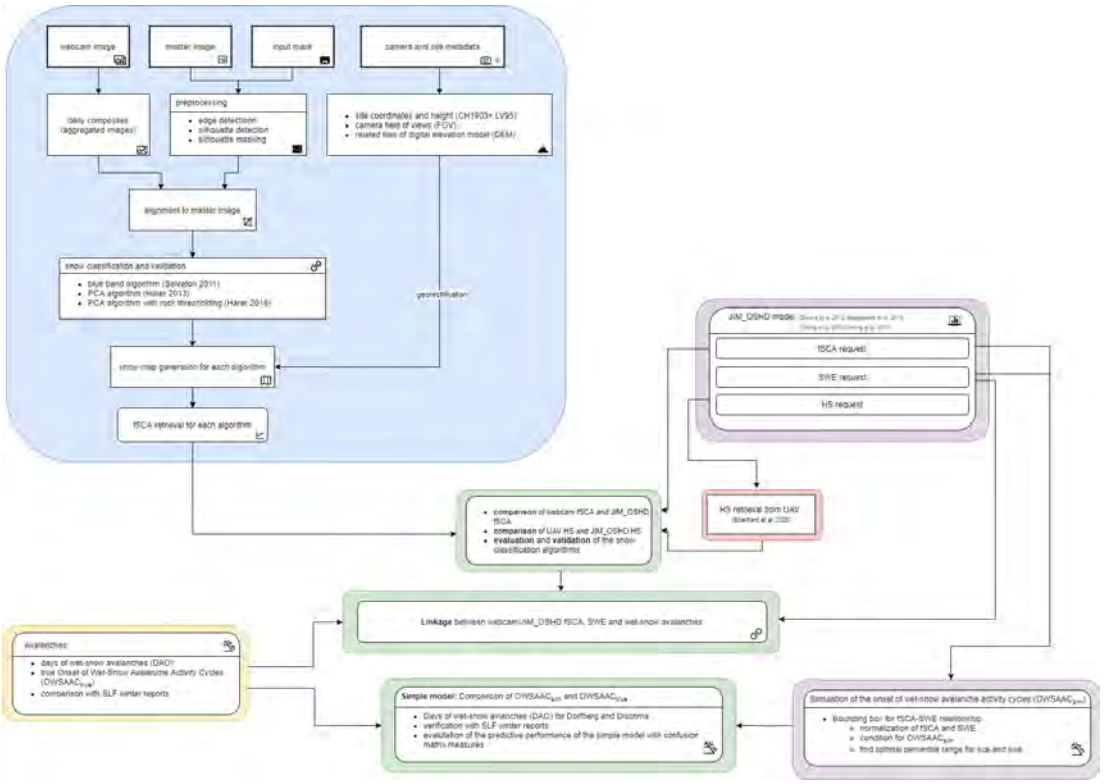

FIGURE A.1: Flowchart of the working process of this study. The green boxes refer to the research questions whereas the blue, purple, yellow and red boxes refer to the different Sections in Chapter 3.

A.2 Results

A.2.1 Comparison between Webcam fSCA and JIM_OSHD fSCA

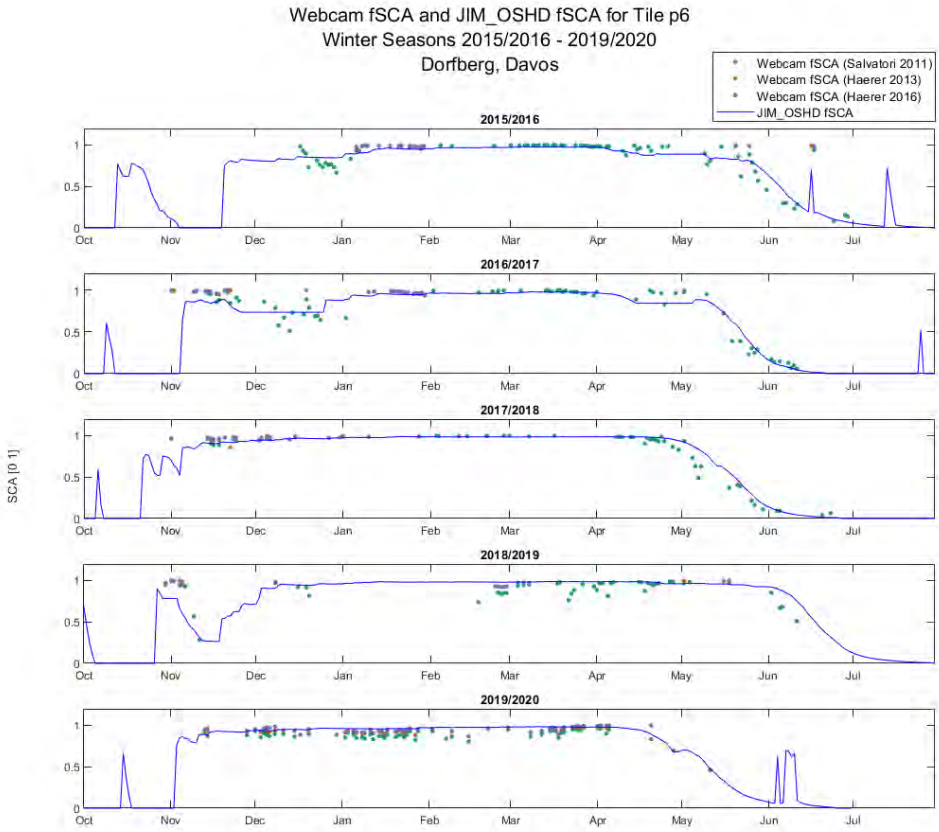

FIGURE A.2: Comparison of webcam fSCA and JIM_OSHD fSCA-data for tile p6 in winter seasons 2016/2017 and 2017/2018. Webcam fSCA-data was calculated with the snow classification algorithms Härer et al. (2013, 2016) and Salvatori et al. (2011) and is shown with different colours (points). The blue solid line represents the JIM_OSHD fSCA-data for the same tile p6.

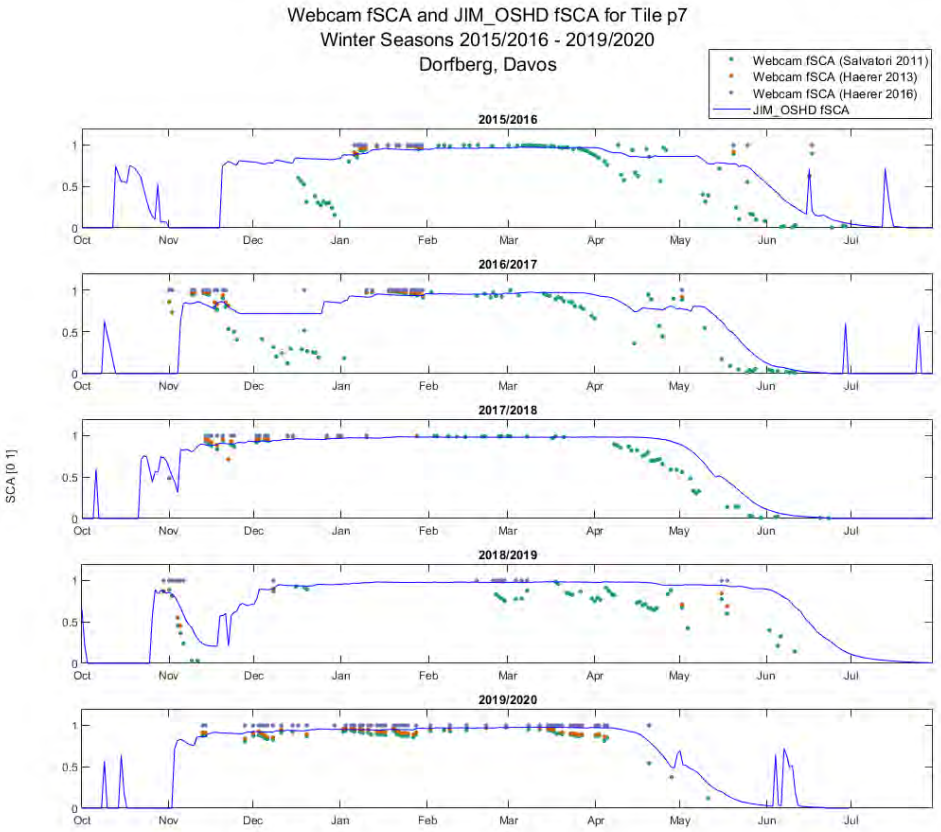

FIGURE A.3: Comparison of webcam fSCA and JIM_OSHD fSCA-data for tile p7 in winter seasons 2016/2017 and 2017/2018. Webcam fSCA-data was calculated with the snow classification algorithms Härer et al. (2013, 2016) and Salvatori et al. (2011) and is shown with different colours (points). The blue solid line represents the JIM_OSHD fSCA-data for the same tile p7.

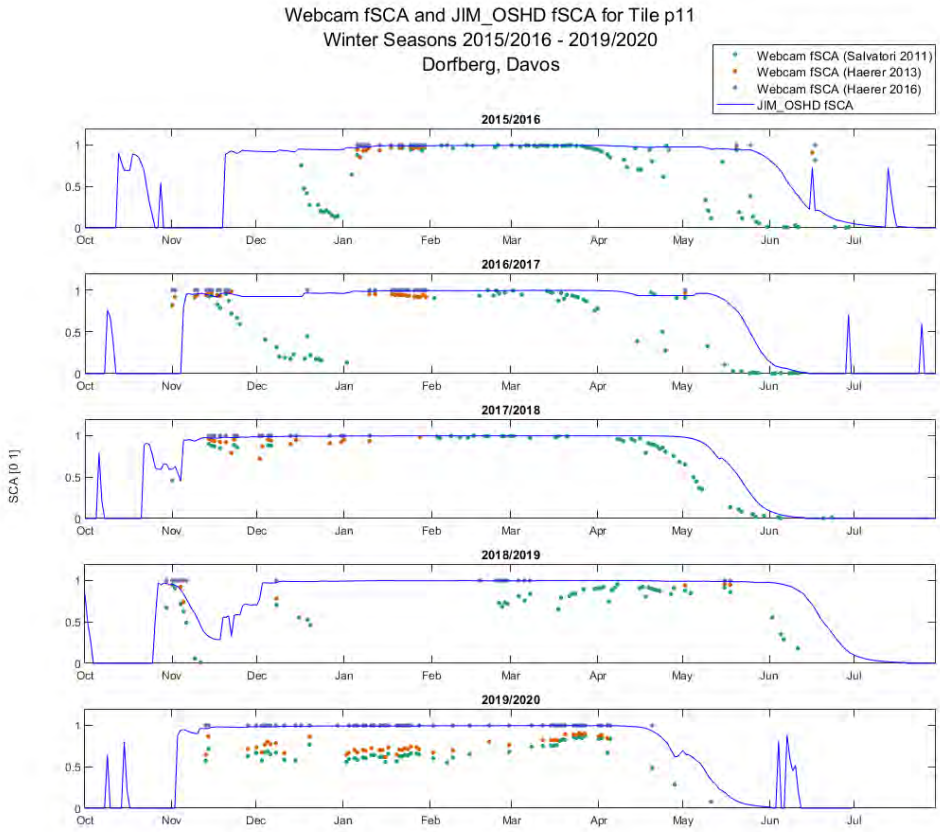

FIGURE A.4: Comparison of webcam fSCA and JIM_OSHD fSCA-data for tile p11 in winter seasons 2016/2017 and 2017/2018. Webcam fSCA-data was calculated with the snow classification algorithms Härer et al. (2013, 2016) and Salvatori et al. (2011) and is shown with different colours (points). The blue solid line represents the JIM_OSHD fSCA-data for the same tile p11.

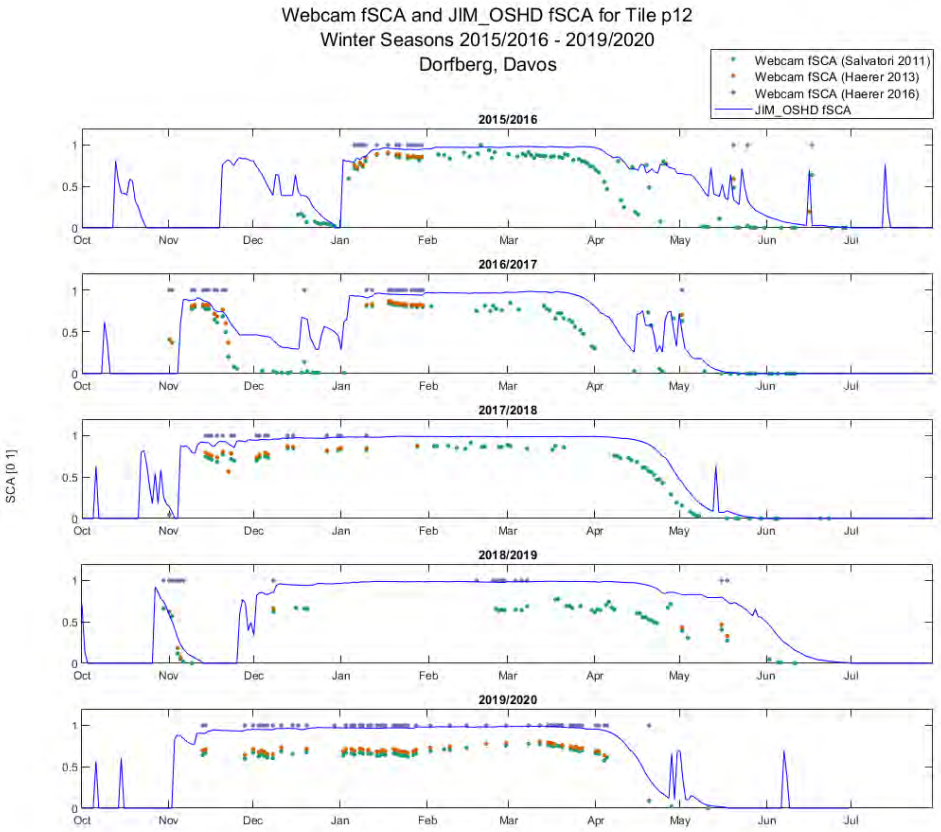

FIGURE A.5: Comparison of webcam fSCA and JIM_OSHD fSCA-data for tile p12 in winter seasons 2016/2017 and 2017/2018. Webcam fSCA-data was calculated with the snow classification algorithms Härer et al. (2013, 2016) and Salvatori et al. (2011) and is shown with different colours (points). The blue solid line represents the JIM_OSHD fSCA-data for the same tile p12.

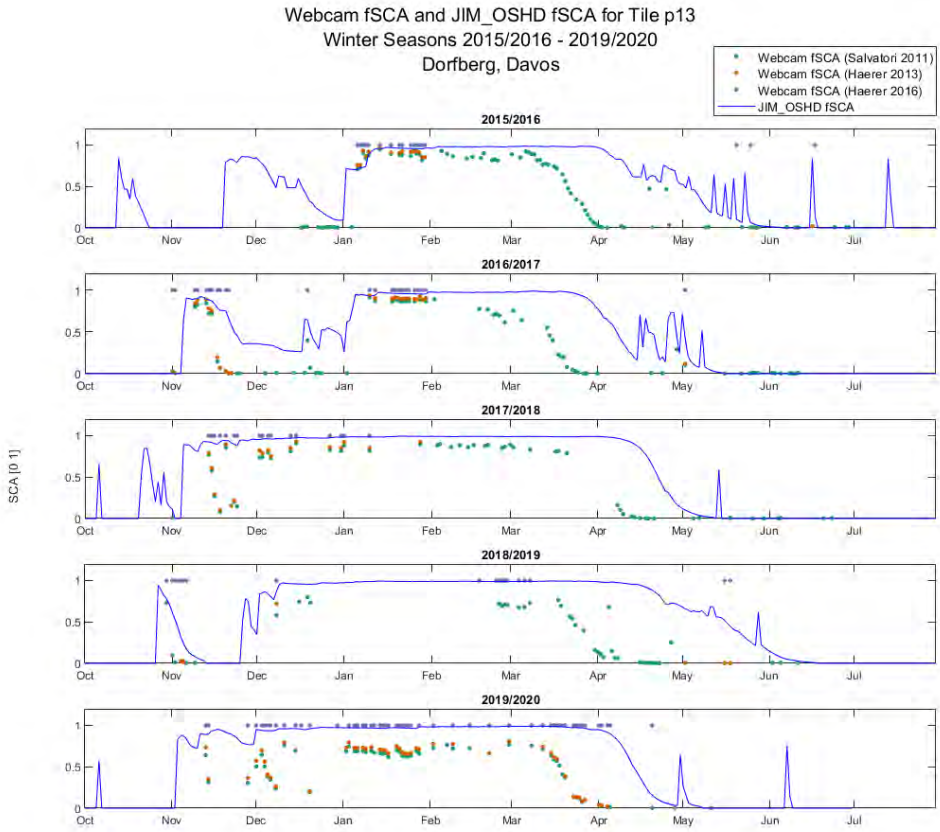

FIGURE A.6: Comparison of webcam fSCA and JIM_OSHD fSCA-data for tile p13 in winter seasons 2016/2017 and 2017/2018. Webcam fSCA-data was calculated with the snow classification algorithms Härer et al. (2013, 2016) and Salvatori et al. (2011) and is shown with different colours (points). The blue solid line represents the JIM_OSHD fSCA-data for the same tile p13.

A.2.2 Elevation Dependency

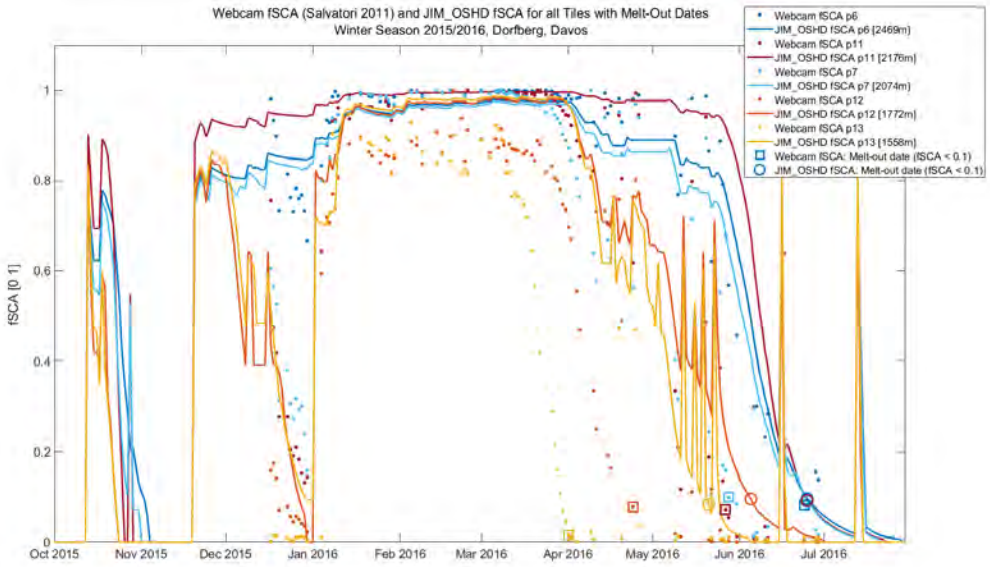

FIGURE A.7: Comparison between data of webcam fSCA (points) and JIM_OSHD fSCA (solid lines) for winter season 2015/2016 coloured according to their altitude. The melt-out date is defined if fSCA ≤ 0.1 is met and marked with a circle for webcam fSCA-data and a square for JIM_OSHD fSCA-data.

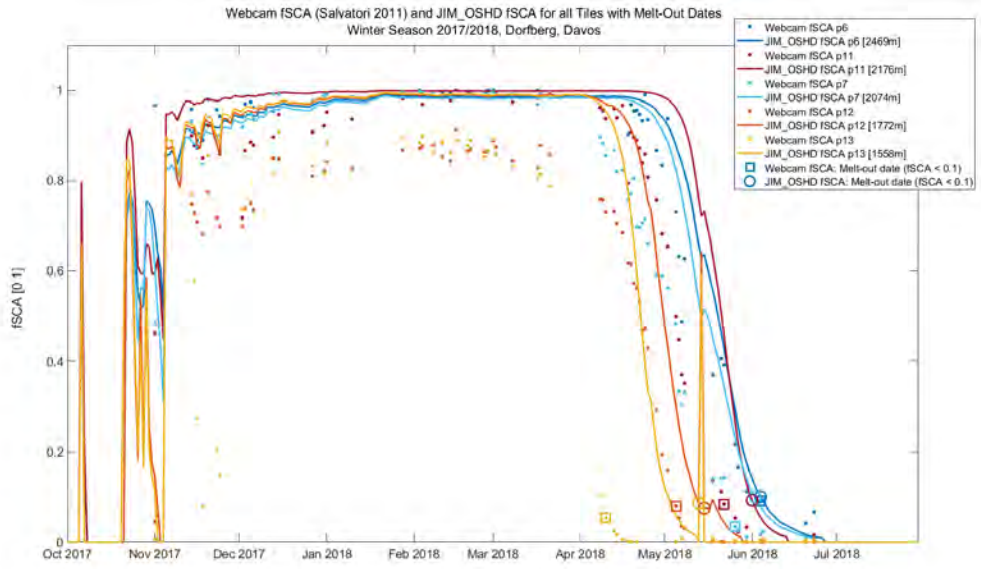

FIGURE A.8: Comparison between data of webcam fSCA (points) and JIM_OSHD fSCA (solid lines) for winter season 2017/2018 coloured according to their altitude. The melt-out date is defined if fSCA ≤ 0.1 is met and marked with a circle for webcam fSCA-data and a square for JIM_OSHD fSCA-data.

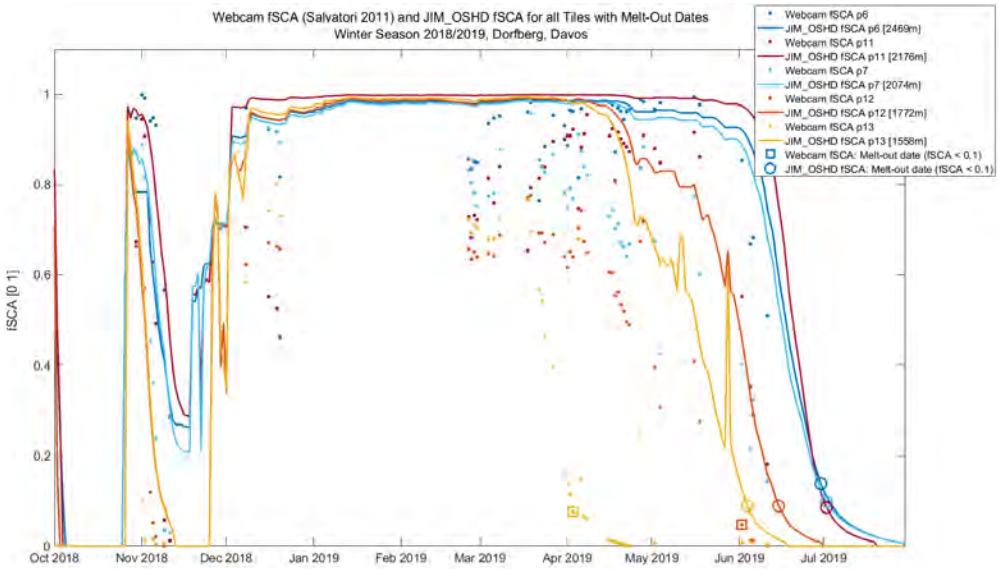

FIGURE A.9: Comparison between data of webcam fSCA (points) and JIM_OSHD fSCA (solid lines) for winter season 2018/2019 coloured according to their altitude. The melt-out date is defined if fSCA ≤ 0.1 is met and marked with a circle for webcam fSCA-data and a square for JIM_OSHD fSCA-data.

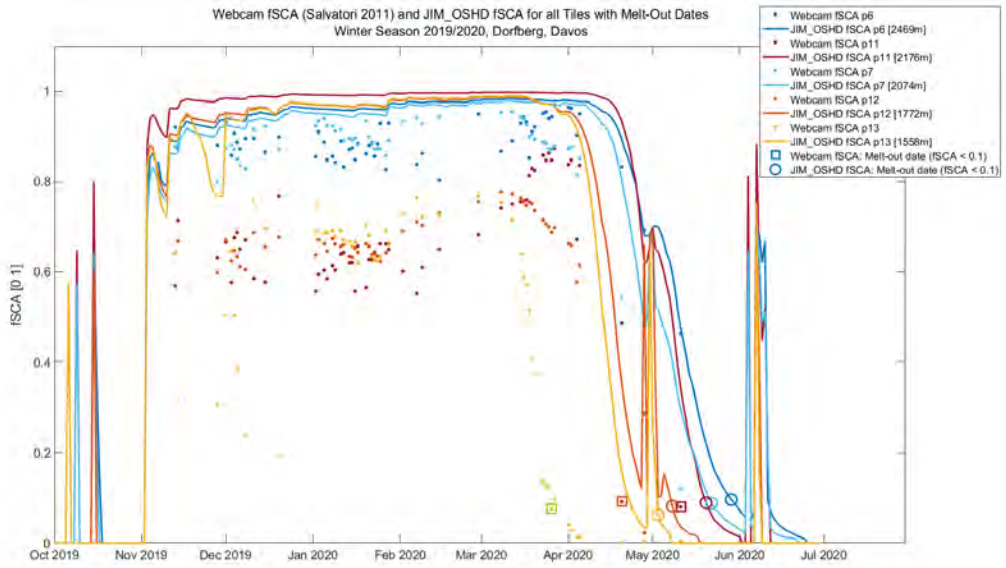

FIGURE A.10: Comparison between data of webcam fSCA (points) and JIM_OSHD fSCA (solid lines) for winter season 2019/2020 coloured according to their altitude. The melt-out date is defined if fSCA ≤ 0.1 is met and marked with a circle for webcam fSCA-data and a square for JIM_OSHD fSCA-data.

A.2.3 Melt-Out Dates for Webcam fSCA and JIM_OSHD fSCA

TABLE A.1: Melt-out dates for webcam fSCA and JIM_OSHD fSCA in winter seasons 2015/2016 to 2019/2020, starting from the tile with the lowest altitude (p13) to the tile with the highest altitude (p6). A melt-out date is defined by fSCA ≤ 0.1 after 1 March. In parentheses the values corresponding to the first fSCA value that has met fSCA ≤ 0.1 are given.

	webcam fSCA	JIM_OSHD fSCA	webcam fSCA	JIM_OSHD fSCA	webcam fSCA	JIM_OSHD fSCA	webcam fSCA	JIM_OSHD fSCA	webcam fSCA	JIM_OSHD fSCA
	p13 [1558 m a.s.l.]	p13 [1558 m a.s.l.]	p12 [1772 m a.s.l.]	p12 [1772 m a.s.l.]	p7 [2074 m a.s.l]	p7 [2074 m a.s.l]	p11 [2176 m a.s.l.]	p11 [2176 m a.s.l.]	p6 [2469 m a.s.l.]	p6 [2469 m a.s.l.]
2015/2016	30.03.2016 (0.0680)	21.05.2016 (0.0821)	24.04.2016 (0.0781)	05.06.2016 (0.0949)	28.05.2016 (0.0985)	25.06.2016 (0.0894)	27.05.2016 (0.0716)	25.06.2016 (0.0917)	24.06.2016 (0.0811)	25.06.2016 (0.0957)
2016/2017	21.03.2017 (0.0805)	06.05.2017 (0.898)	15.04.2017 (0.0279)	12.05.2017 (0.0831)	19.05.2017 (0.0930)	03.06.2017 (0.0955)	19.05.2017 (0.0271)	03.06.2017 (0.0928)	09.06.2017 (0.0686)	06.06.2017 (0.0943)
2017/2018	10.04.2018 (0.0536)	03.05.2018 (0.0858)	05.05.2018 (0.0793)	13.05.2018 (0.0853)	26.05.2018 (0.0338)	02.06.2018 (0.0995)	22.05.2018 (0.0834)	01.06.2018 (0.0919)	04.06.2018 (0.0911)	04.06.2018 (0.0997)
2018/2019	03.04.2019 (0.0757)	04.06.2019 (0.0886)	02.06.2019 (0.0470)	15.06.2019 (0.8840)	after 11 June 2019	02.07.2019 (0.0979)	after 11 June 2019	02.07.2019 (0.0852)	after 11 June 2019	03.07.2019 (0.0986)
2019/2020	26.03.2020 (0.7570)	23.04.2020 (0.0883)	20.04.2020 (0.0914)	08.05.2020 (0.0817)	after 11 May 2020	22.05.2020 (0.0880)	11.05.2020 (0.0797)	20.05.2020 (0.0890)	after 11 May 2020	29.05.2020 (0.0958)

A.2.4 Link between fSCA and SWE

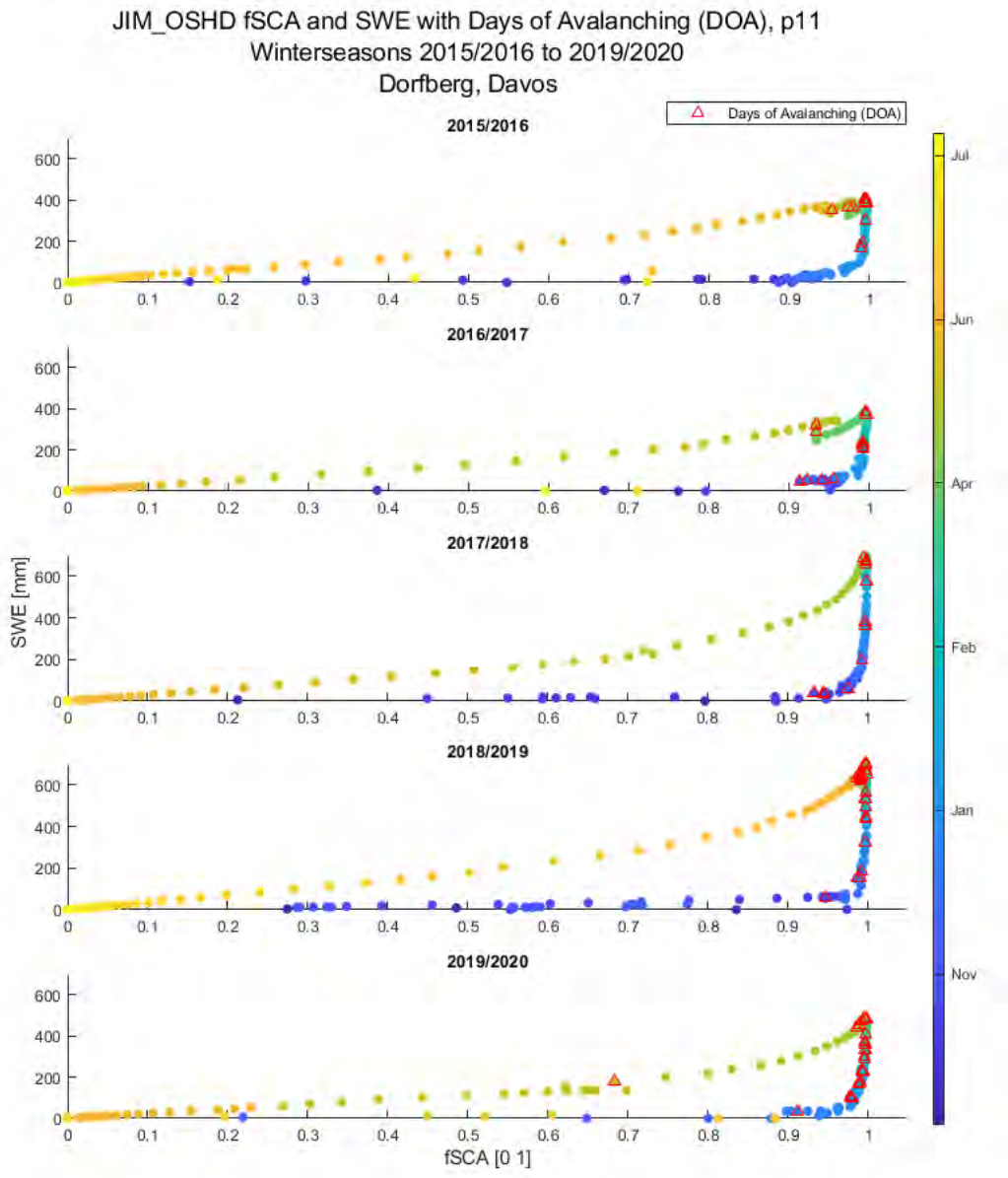

FIGURE A.11: JIM_OSHD fSCA [0 1] with JIM_OSHD SWE [mm] of tile p11 for winter seasons 2015/2016 to 2019/2020. Each colored data point refers to a day of year, while the days of avalanches (DOA) are marked with red triangles.

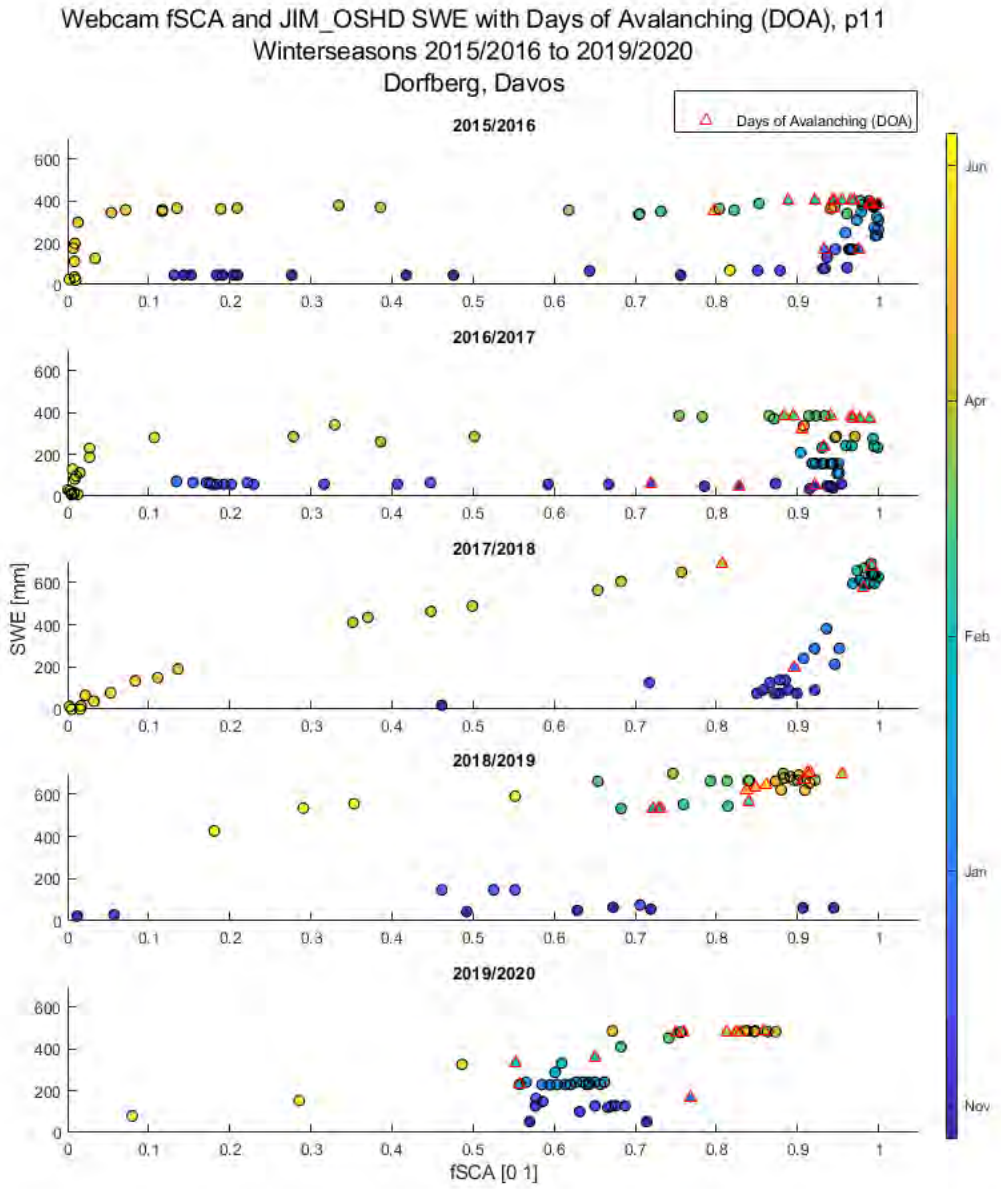

FIGURE A.12: Webcam fSCA [0 1] with JIM_OSHD SWE [mm] of tile p11 for winter seasons 2015/2016 to 2019/2020. The webcam fSCA is calculated with the blue band algorithm of Salvatori et al. (2011). Each colored data point refers to a day of year, while the days of avalanches (DOA) are marked with red triangles.

A.2.5 Best Runs for Simulating the *OWSAAC*

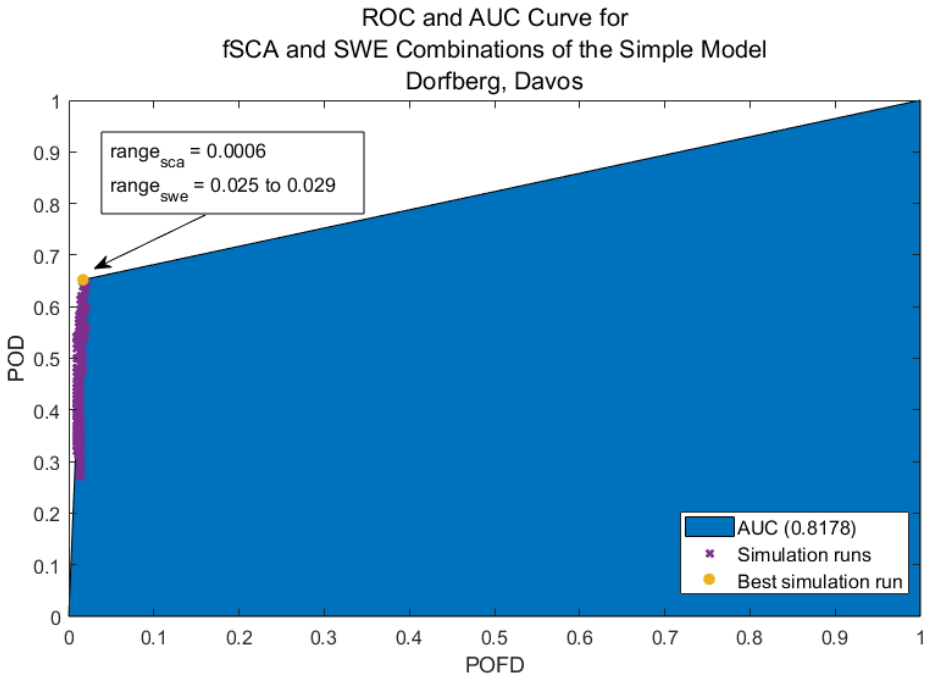

FIGURE A.13: ROC curve and AUC for all simulated runs for the Dorfberg site. The simulated runs are marked with purple crosses, the best run with $range_{sca}$ = 0.0006 and $range_{swe}$ = 0.025 to 0.029 is marked as an orange point. The AUC (blue colored area) with value 0.8178 displays the integral from 0 to the best run to 1 for both POFD and POD.

Bibliography

Ahn, Y. and J. E. Box (2010). "Glacier velocities from time-lapse photos: technique development and first results from the Extreme Ice Survey (EIS) in Greenland". In: *Journal of Glaciology* 56.198, 723–734.

Armstrong, R. (1976). "Wet snow avalanches. Avalanche release and snow characteristics". In: *San Juan Mountains, Colorado. Sun Juan Avalanche Project, Final Report 1971-1975, Occasional Paper No. 19, R. Armstrong and J. Ives, Eds., Institute of Arctic and Alpine Research, University of Colorado, Boulder CO, U.S.A., 67–82.*

Aschenwald, J., K. Leichter, E. Tasser, and U. Tappeiner (2001). "Spatio-temporal landscape analysis in mountainous terrain by means of small format photography: a methodological approach". In: *IEEE Transactions on Geoscience and Remote Sensing* 39.4, pp. 885–893. ISSN: 1558-0644.

Avanzi, F. et al. (2017). "Measuring the snowpack depth with Unmanned Aerial System photogrammetry: comparison with manual probing and a 3D laser scanning over a sample plot". In: *The Cryosphere Discussions* 2017, pp. 1–19.

Baggi, S. and J. Schweizer (2009). "Characteristics of wet-snow avalanche activity: 20 years of observations from a high alpine valley (Dischma, Switzerland)." In: *Nat Hazards* 50, 97–108.

Bartelt, P. and M. Lehning (2002). "A physical SNOWPACK model for the Swiss avalanche warning: Part I: numerical model". In: *Cold Regions Science and Technology* 35.3, pp. 123 –145. ISSN: 0165-232X.

Bellaire, S., A. van Herwijnen, C. Mitterer, and J. Schweizer (2017). "On forecasting wet-snow avalanche activity using simulated snow cover data". In: *Cold Regions Science and Technology* 144. International Snow Science Workshop 2016 Breckenridge, pp. 28 –38. ISSN: 0165-232X.

Beniston, M. (2003). "Climatic Change in Mountain Regions: A Review of Possible Impacts". In: *Climatic Change* 59, pp. 5–31.

Bernard, J. Friedt, F. Tolle, M. Griselin, G. Martin, D. Laffly, and C. Marlin (2013). "Monitoring seasonal snow dynamics using ground based high resolution photography (Austre Lovénbreen, Svalbard, 79°N)". In: *ISPRS Journal of Photogrammetry and Remote Sensing* 75, pp. 92 –100. ISSN: 0924-2716.

Bertle, F. A. (1966). "Effect of snow compaction on runoff from rain on snow". In: *U.S. Govt. Print. Off.* 35, pp. 1–56.

Bozzini, C., M. Conedera, and P. Krebs (2012). "A New Monoplotting Tool to Extract Georeferenced Vector Data and Orthorectified Raster Data from Oblique Non-Metric Photographs". In: *International Journal of Heritage in the Digital Era* 1, pp. 499–518.

Broll, G. and B. Keplin (2005). "Mountain ecosystems : studies in treeline ecology / Gabriele Broll, Beate Keplin, (eds)". In: *SERBIULA (sistema Librum 2.0)*.

Brun, E., P. David, M. Sudul, and G. Brunot (1992). "A numerical model to simulate snow-cover stratigraphy for operational avalanche forecasting". In: *Journal of Glaciology* 38.128, 13–22.

Brun, E., Martin, V. Simon, C. Gendre, and C. Coleou (1989). "An Energy and Mass Model of Snow Cover Suitable for Operational Avalanche Forecasting". In: *Journal of Glaciology* 35.121, 333–342.

Bühler, Y., M. Marty, L. Egli, J. Veitinger, T. Jonas, P. Thee, and C. Ginzler (2015). "Snow depth mapping in high-alpine catchments using digital photogrammetry". In: *The Cryosphere* 9.1, pp. 229–243.

Bujang, M. A. and N. Baharum (2016). "Sample Size Guideline for Correlation Analysis". In: *World Journal of Social Science Research* 3, p. 37.

Cianfarra, P., F. Salvini, and M. Valt (2009). "Monitoring the spatio-temporal evolution of the snow cover in the eastern Alps from MODIS data". In: *EGU General Assembly 2009* 11.

Corripio, J. G. (2004). "Snow surface albedo estimation using terrestrial photography". In: *International Journal of Remote Sensing* 25.24, pp. 5705–5729.

Das, T. (2017). "Machine Learning algorithms for Image Classification of hand digits and face recognition dataset". In: *International Research Journal of Engineering and Technology (IRJET)* 04.12, pp. 640 –649.

Dechant, C. and H. Moradkhani (2011). "Radiance data assimilation for operational snow and streamflow forecasting". In: *Advances in Water Resources* 34.3, pp. 351 –364. ISSN: 0309-1708.

Derksen, C. and E. LeDrew (2000). "Variability and change in terrestrial snow cover: Data acquisition and links to the atmosphere". In: *Progress in Physical Geography - PROG PHYS GEOG* 24, pp. 469–498.

Dietz, A. J., C. Kuenzer, U. Gessner, and S. Dech (2012). "Remote sensing of snow – a review of available methods". In: *International Journal of Remote Sensing* 33.13, pp. 4094–4134.

Dizerens, C. (2015). "Georectification and snow classification of webcam images: potential for complementing satellite-derived snow maps over Switzerland". MA thesis. University of Bern.

Dozier, J. (1989). "Spectral signature of alpine snow cover from the Landsat Thematic Mapper". In: *Remote Sensing of Environment* 28.

Durand, Y., G. Giraud, E. Brun, L. Mérindol, and E. Martin (1999). "A computer-based system simulating snowpack structures as a tool for regional avalanche forecasting". In: *Journal of Glaciology* 45.151, 469–484.

Eberhard, L. A., P. Sirguey, A. Miller, M. Marty, K. Schindler, A. Stoffel, and Y. Bühler (2020). "Intercomparison of photogrammetric platforms for spatially continuous snow depth mapping". In: *The Cryosphere Discussions* 2020, pp. 1–40.

Essery, R., S. Morin, Y. Lejeune, and C. B Ménard (2013a). "A comparison of 1701 snow models using observations from an alpine site". In: *Advances in Water Resources* 55. Snow–Atmosphere Interactions and Hydrological Consequences, pp. 131 –148. ISSN: 0309-1708.

Essery, R., S. Morin, Y. Lejeune, and C. Menard (2013b). "A comparison of 1701 snow models using observations from an alpine site". In: *Advances in Water Resources* 55, pp. 131–148.

Farinotti, D., J. Magnusson, M. Huss, and A. Bauder (2010). "Snow accumulation distribution inferred from time-lapse photography and simple modelling". In: *Hydrological Processes* 24.15, pp. 2087–2097.

Fassnacht, S. R., G. A. Sexstone, A. H. Kashipazha, J. I. López-Moreno, M. F. Jasinski, S. K. Kampf, and B. C. Von Thaden (2016). "Deriving snow-cover depletion curves for different spatial scales from remote sensing and snow telemetry data". In: *Hydrological Processes* 30.11, pp. 1708–1717.

Fedorov, R., A. Camerada, P. Fraternali, and M. Tagliasacchi (2015). "Estimating Snow Cover From Publicly Available Images". In: *IEEE Transactions on Multimedia* 18.

Feick, S., C. Mitterer, L. Dreier, S. Harvey, and J. Schweizer (2012). "Automated detection and monitoring of glide-snow events using satellite based optical remote sensing

and terrestrial photography". In: *ISSW 2012, international snow science workshop*, pp. 603–609.

Fierz, C., R. Armstrong, Y. Durand, P. Etchevers, E. Greene, D. McClung, K. Nishimura, P. Satyawali, and S. Sokratov (2009). "The International classification for seasonal snow on the ground". In: *IHP-VII Technical Documents in Hydrology N°83, IACS Contribution N°1, UNESCO-IHP, Paris*.

Finger, D., M. Vis, M. Huss, and J. Seibert (2015). "The value of multiple data set calibration versus model complexity for improving the performance of hydrological models in mountain catchments". In: *Water Resources Research* 51.4, pp. 1939–1958.

Foppa, N., S. Wunderle, D. Oesch, and F. Kuchen (2004). "Operational sub-pixel snow mapping over the Alps with NOAA AVHRR data". In: *Annals of Glaciology* 38, 245–252.

GCOS (2020). *Snow: Essential Climate Variable*. URL: https://gcos.wmo.int/en/essential-climate-variables/snow.

geo.admin.ch (2020). *Maps of geo.admin.ch*. Swiss Federal Institute of Topography swisstopo. URL: https://www.geo.admin.ch/en/home/meta/responsabilities-and-contacts.html.

Giorgi, F. (2006). "Regional climate modeling: Status and perspectives". In: *J. Phys. IV France* 139, pp. 101–118.

Griessinger, N., M. Schirmer, N. Helbig, A. Winstral, A. Michel, and T. Jonas (2019). "Implications of observation-enhanced energy-balance snowmelt simulations for runoff modeling of Alpine catchments". In: *Advances in Water Resources* 133, p. 103410. ISSN: 0309-1708.

Griessinger, N., J. Seibert, J. Magnusson, and T. Jonas (2016). "Assessing the benefit of snow data assimilation
for runoff modeling in Alpine catchments". In: *Hydrology and Earth System Sciences* 20.9, pp. 3895–3905.

Grünewald, T., Y. Bühler, and M. Lehning (2014). "Elevation dependency of mountain snow depth". In: *The Cryosphere* 8.6, pp. 2381–2394.

Grünewald, T. and M. Lehning (2015). "Are flat-field snow depth measurements representative? A comparison of selected index sites with areal snow depth measurements at the small catchment scale". In: *Hydrological Processes* 29.7, pp. 1717–1728.

Hall, A. (2004). "The Role of Surface Albedo Feedback in Climate". In: *Journal of Climate - J CLIMATE* 17, pp. 1550–1568.

Hall, D., G. Riggs, and V. Salomonson (2001). "Algorithm theoretical basis document(ATBD) for the MODIS snow- and sea ice-mapping algorithms". In: *MODIS and VIIRS Snow and Ice Global Mapping Project*.

Hall, D. K., G. A. Riggs, N. E. D. Girolamo, and M. O. Romàn (2019). "Evaluation of MODIS and VIIRS cloud-gap-filled snow-cover products for production of an Earth science data record". In: *Hydrology and Earth System Sciences* 23.12, pp. 5227–5241.

Hao, C., L. Dongze, and G. Shenghua (2018). "Evaluating Capability of Deep Neural Networksfor Image Classification via Information Plane". In: *ECCV*.

Harrison, W., K. Echelmeyer, D. Cosgrove, and C. F. Raymond (1992). "The determination of glacier speed by time-lapse photography under unfavorable conditions". In: *Journal of Glaciology* 38.129, 257–265.

Hedrick, A. and H.-P. Marshall (2014). "Automated Snow Depth Measurements in Avalanche Terrain Using Time-Lapse Photography". In: *2014 International Snow Science, Banff, AB, Canada*.

Helbig, N., M. Ehrler, M. Schirmer, and T. Jonas (2018). "Where is the snow: validating a fractional-snow covered area parameterization for snow melt forecasting with

satellite measurements". In: *International snow science workshop proceedings 2018*, pp. 357–360.

Helbig, N. and A. van Herwijnen (2017). "Subgrid parameterization for snow depth over mountainous terrain from flat field snow depth". In: *Water Resources Research* 53.2, pp. 1444–1456.

Helbig, N., A. van Herwijnen, J. Magnusson, and T. Jonas (2015a). "Fractional snow-covered area parameterization over complex topography". In: *Hydrology and Earth System Sciences* 19.3, pp. 1339–1351.

Helbig, N., A. van Herwijnen, and T. Jonas (2015b). "Forecasting wet-snow avalanche probability in mountainous terrain". In: *Cold Regions Science and Technology* 120, pp. 219–226.

Herwijnen, A. van, J. Failletaz, N. Berhod, and C. Mitterer (2013a). "Investigating glide snow avalanche release using seismic monitoring in combination with time-lapse photography". In: *EGU General Assembly Conference Abstracts*. EGU General Assembly Conference Abstracts, p. 14045.

Herwijnen, A. van, N. Berthod, R. Simenhois, and C. Mitterer (2013b). "Using time-lapse photography in avalanche research". In: *International Snow Science Workshop Grenoble – Chamonix Mont-Blanc - 2013*, pp. 1–6.

Herwijnen, A. van and R. Simenhois (2012). "Monitoring glide avalanches using time-lapse photography". In: *ISSW 2012, international snow science workshop*, pp. 899–903.

Hinkler, J., S. B. Pedersen, M. Rasch, and B. U. Hansen (2002). "Automatic snow cover monitoring at high temporal and spatial resolution, using images taken by a standard digital camera". In: *International Journal of Remote Sensing* 23.21, pp. 4669–4682.

Hirashima, H., S. Yamaguchi, and T. Katsushima (2014). "A multi-dimensional water transport model to reproduce preferential flow in the snowpack". In: *Cold Regions Science and Technology* 108, pp. 80 –90. ISSN: 0165-232X.

Huss, M., D. Farinotti, A. Bauder, and M. Funk (2008). "Modelling runoff from highly glacierized alpine drainage basins in a changing climate". In: *Hydrological Processes* 22.19, pp. 3888–3902.

Härer, S., M. Bernhardt, J. G. Corripio, and K. Schulz (2013). "PRACTISE – Photo Rectification And ClassificaTIon SoftwarE (V.1.0)". In: *Geoscientific Model Development* 6.3, pp. 837–848.

Härer, S., M. Bernhardt, and K. Schulz (2016). "PRACTISE - Photo Rectification And ClassificaTIon SoftwarE (V.2.1)". In: *Geoscientific Model Development* 9.1, pp. 307–321.

Hüsler, F., T. Jonas, M. Riffler, J. Musial, and S. Wunderle (2014). "A satellite-based snow cover climatology (1985–2011) for the European Alps derived from AVHRR data". In: *The Cryosphere* 8, pp. 73–90.

Hüsler, F., T. Jonas, S. Wunderle, and S. Albrecht (2012). "Validation of a modified snow cover retrieval algorithm from historical 1-km AVHRR data over the European Alps". In: *Remote Sensing of Environment* 121, 497–515.

Johnson, F. and A. Sharma (2011). "Accounting for interannual variability: A comparison of options for water resources climate change impact assessments". In: *Water Resources Research* 47.4.

Jomelli, V., C. Delval, D. Grancher, S. Escande, D. Brunstein, B. Hetu, L. Filion, and P. Pech (2007). "Probabilistic analysis of recent snow avalanche activity and weather in the French Alps". In: *Cold Regions Science and Technology* 47.1. A Selection of papers presented at the International Snow Science Workshop, Jackson Hole, Wyoming, September 19-24, 2004, pp. 180 –192. ISSN: 0165-232X.

Jonas, T., C. Marty, and J. Magnusson (2009). "Estimating the snow water equivalent from snow depth measurements in the Swiss Alps". In: *Journal of Hydrology* 378.1, pp. 161 –167. ISSN: 0022-1694.

Jörg-Hess, S., N. Griessinger, and M. Zappa (2015). "Probabilistic Forecasts of Snow Water Equivalent and Runoff in Mountainous Areas*". In: *Journal of Hydrometeorology* 16.5, pp. 2169–2186. ISSN: 1525-755X.

Kattelmann, R. (1985). "Wet slab instability". In: *Proceedings of the International Snow Science Workshop, Aspen, Colorado, U.S.A.*, pp. 102–108.

Kazmier, L. (2003). *Business statistics : based on Schaum's outline of theory and problems of business statistics, third edition*. Vol. 13. New York, McGraw-Hill, pp. 1–179.

Kepski, D., B. Luks, K. Migala, T. Wawrzyniak, S. Westermann, and B. Wojtuń (2017). "Terrestrial Remote Sensing of Snowmelt in a Diverse High-Arctic Tundra Environment Using Time-Lapse Imagery". In: *Remote Sensing* 9.

Klein, G., Y. Vitasse, C. Rixen, C. Marty, and M. Rebetez (2016). "Shorter snow cover duration since 1970 in the Swiss Alps due to earlier snowmelt more than to later snow onset". In: *Climatic Change*.

Kurtz, W. et al. (2017). "Integrating hydrological modelling, data assimilation and cloud computing for real-time management of water resources". In: *Environmental Modelling & Software* 93, pp. 418 –435. ISSN: 1364-8152.

Lafaysse, M., S. Morin, D. Serca, F. Besson, J.-M. Willemet, G. Giraud, and Y. Durand (2013). "Towards a New Chain of Models for Avalanche Hazard Forecasting in French Mountain Ranges, Including Low Altitude Mountains". In: *International Snow Science Workshop Grenoble – Chamonix Mont-Blanc - October 07-11, 2013*.

Laternser, M. and M. Schneebeli (2003). "Long-term snow climate trends of the Swiss Alps (1931-99)". In: *International Journal of Climatology* 23, pp. 733 –750.

Lehning, M., P. Bartelt, B. Brown, C. Fierz, and P. Satyawali (2002). "A physical SNOWPACK model for the Swiss avalanche warning Part II: Snow microstructure". In: *Cold Regions Science and Technology* 35, pp. 147–167.

Li, X., Y. Jing, H. Shen, and L. Zhang (2019). "The recent developments in cloud removal approaches of MODIS snow cover product". In: *Hydrology and Earth System Sciences* 23.5, pp. 2401–2416.

Lowe, D. G. (1999). "Object Recognition from Local Scale-Invariant Features". In: *Proc. of the International Conference on Computer Vision, Corfu*, pp. 1–8.

Luce, C. H., D. G. Tarboton, and K. R. Cooley (1999). "Sub-grid parameterization of snow distribution for an energy and mass balance snow cover model". In: *Hydrological Processes* 13.12-13, pp. 1921–1933.

Machguth, H., O. Eisen, F. Paul, and M. Hoelzle (2006). "Strong spatial variability of snow accumulation observed with helicopter-borne GPR on two adjacent Alpine glaciers". In: *Geophysical Research Letters* 33.13.

Magand, C., A. Ducharne, N. Le Moine, and S. Gascoin (2014). "Introducing Hysteresis in Snow Depletion Curves to Improve the Water Budget of a Land Surface Model in an Alpine Catchment". In: *Journal of Hydrometeorology* 15.2, pp. 631–649. ISSN: 1525-755X.

Magnusson, J., N. Wever, R. Essery, N. Helbig, A. Winstral, and T. Jonas (2015). "Evaluating snow models with varying process representations for hydrological applications". In: *Water Resources Research* 51.4, pp. 2707–2723.

Marty, C. (2008). "Regime shift of snow days in Switzerland". In: *Geophysical Research Letters* 35.

McClung, D. and P. A. Schaerer (2006). *The Avalanche Handbook*. The Mountaineers Books, Seattle WA, U.S.A.

Mitterer, C. and J. Schweizer (2014). "Comparing Models of Different Levels of Complexity for the Prediction of Wet-Snow Avalanches". In: *Proceedings, International Snow Science Workshop, Banff, 2014*.

Mitterer, C. (2012). "Formation of wet-snow avalanches". PhD thesis. ETH Zurich.

Mitterer, C. and J. Schweizer (2013). "Analysis of the snow-atmosphere energy balance during wet-snow instabilities and implications for avalanche prediction". In: *The Cryosphere* 7.1, pp. 205–216.

Moeser, D., G. Mazzotti, N. Helbig, and T. Jonas (2016). "Representing spatial variability of forest snow: Implementation of a new interception model". In: *Water Resources Research* 52.2, pp. 1208–1226.

Morin, S., Y. Lejeune, B. Lesaffre, J.-M. Panel, D. Poncet, P. David, and M. Sudul (2012). "An 18-yr long (1993–2011) snow and meteorological dataset from a mid-altitude mountain site (Col de Porte, France, 1325 m alt.) for driving and evaluating snowpack models". In: *Earth System Science Data* 4.1, pp. 13–21.

Parajka, J. and G. Blöschl (2008). "Spatio-temporal combination of MODIS images – Potential for snow cover mapping". In: *Water Resources Research - WATER RESOUR RES* 440.

Parajka, J., P. Haas, R. Kirnbauer, J. Jansa, and G. Blöschl (2012). "Potential of time-lapse photography of snow for hydrological purposes at the small catchment scale". In: *Hydrological Processes* 26.22, pp. 3327–3337.

Parajka, J., M. Pepe, A. Rampini, S. Rossi, and G. Blöschl (2010). "A regional snow-line method for estimating snow cover from MODIS during cloud cover". In: *Journal of Hydrology* 381, pp. 203–212.

Peitzsch, E., J. Hendrikx, D. Fagre, and B. Reardon (2012). "Examining spring wet slab and glide avalanche occurrence along the Going-to-the-Sun Road corridor, Glacier National Park, Montana, USA". In: *Cold Regions Science and Technology* 78, 73–81.

Pielmeier, C., F. Techel, C. Marty, and T. Stucki (2013). "Wet snow avalanche activity in the Swiss Alps –trend analysis for mid-winter season". In: *International Snow Science Workshop Grenoble – Chamonix Mont-Blanc - 2013*.

Portenier, C., F. Hüsler, S. Härer, and S. Wunderle (2019). "Towards a webcam-based snow cover monitoring network: methodology and evaluation". In: *The Cryosphere Discussions*, pp. 1–20.

QGIS.org (2020). *QGIS Geographic Information System. Open Source Geospatial Foundation Project.* URL: https://www.qgis.org/.

Qu, X. and A. Hall (2007). "What Controls the Strength of Snow-Albedo Feedback?" In: *Journal of Climate* 20, pp. 3971–3981.

Rango, A and J. Martinec (1982). *Snow accumulation derived from modified depletion curves of snow coverage*.

Rixen, C., M. Teich, C. Lardelli, D. Gallati, M. Pohl, M. Pütz, and P. Bebi (2011). "Winter Tourism and Climate Change in the Alps: An Assessment of Resource Consumption, Snow Reliability, and Future Snowmaking Potential". In: *Mountain Research and Development* 31.3, pp. 229 –236.

Romig, J. M., S. Custer, K. Birkeland, and W. Locke (2004). "March Wet Avalanche Prediction at Bridger Bowl Ski Area, Montana". In: *Proceedings of the 2004 International Snow Science Workshop, Jackson Hole, Wyoming*.

Salvatori, R., P. Plini, M. Giusto, M. Valt, R. Salzano, M. Montagnoli, A. Cagnati, G. Crepaz, and D. Sigismondi (2011). "Snow cover monitoring with images from digital camera systems". In: *Italian Journal of Remote Sensing* 43.

Salzano, R., R. Salvatori, and F. Dominé (2008). "Investigation on the relation between physical and radiometrical properties of snow covers". In: *In EARSel eProceedings* 7.

Salzano, R., R. Salvatori, M Valt, G. Giuliani, B. Chatenoux, and L. Ioppi (2019). "Automated Classification of Terrestrial Images: The Contribution to the Remote Sensing of Snow Cover". In: *Geosciences (Switzerland)* 9, p. 97.

Scherrer, S., C. Appenzeller, and M. Laternser (2004). "Trends in Swiss Alpine snow days: The role of local- and large-scale climate variability". In: *Geophysical Research Letters* 31, pp. 13215–.

Schweizer, J., C. Mitterer, F. Techel, A. Stoffel, and B. Reuter (2020). "On the relation between avalanche occurrence and avalanche danger level". In: *The Cryosphere* 14.2, pp. 737–750.

Schweizer, J., P. Bartelt, and A. van Herwijnen (2015). "Chapter 12 - Snow Avalanches". In: *Snow and Ice-Related Hazards, Risks and Disasters*. Ed. by J. F. Shroder, W. Haeberli, and C. Whiteman. Boston: Academic Press, pp. 395 –436. ISBN: 978-0-12-394849-6.

Schweizer, J., J. Bruce, and M. Schneebeli (2003). "Snow avalanche formation". In: *Reviews of Geophysics* 41.4.

Schweizer, J. and M. Lütschg (2001). "Characteristics of human-triggered avalanches". In: *Cold Regions Science and Technology* 33.2. ISSW 2000:International Snow Science Workshop, pp. 147 –162. ISSN: 0165-232X.

Schweizer, J., C. Mitterer, and L. Stoffel (2009). "On forecasting large and infrequent snow avalanches". In: *Cold Regions Science and Technology* 59.2. International Snow Science Workshop (ISSW) 2008, pp. 234 –241. ISSN: 0165-232X.

Slater, A. and M. Clark (2006). "Snow Data Assimilation via an Ensemble Kalman Filter". In: *Journal of Hydrometeorology* 7.3, pp. 478–493.

Solberg, R., B. Wangensteen, and O. Rudjord (2012). "Glob Snow Snow Extent Product Guide Product Version1.2". In: *European Space Agency Study Contract Report ESRI Contract 21703/08/I-EC*.

Solomon, S., D. Qin, M. Manning, M. Marquis, K. Averyt, M. Tignor, H. L. Miller, and Z. Chen (2007). "Climate Change 2007 - The Physical Science Basis– . Contribution of Working Group I to the Fourth Assessment Report of the IPCC". In: *Intergovernmental Panel on Climate Change*.

Spisni, A. et al. (2011). "Snow cover analysis in Emilia-Romagna". In: *Italian Journal of Remote Sensing* 43, pp. 59–73.

swisstopo (2018). *swissALTI3D Das hoch aufgelöste Terrainmodell der Schweiz*. Federal Office of Topography swisstopo. URL: https://shop.swisstopo.admin.ch/de/products/height_models/alti3D.

Takala, M., K. Luojus, J. Pulliainen, C. Derksen, J. Lemmetyinen, J.-P. Kärnä, J. Koskinen, and B. Bojkov (2011). "Implementing hemispherical snow water equivalent product assimilating weather station observations and spaceborne microwave data". In: pp. 3768–3771.

Techel, F. and C. Pielmeier (2009). "Wet snow diurnal evolution and stability assessment". In: *Schweizer, J., van Herwijnen, A. (Eds.), International Snow Science Workshop ISSW, Davos, Switzerland, 27 Septembere 2 October 2009, WSL.*, pp. 256 –261.

Thackeray, C. and C. Fletcher (2016). "Snow albedo feedback: Current knowledge, importance, outstanding issues and future directions". In: *Progress in Physical Geography* 40.

Trachsel, J. and M. Heggli (2020). "Winterbericht 2019/2020. Winterflash". In: *WSL Berichte*.

Vedaldi, A. and B. Fulkerson (2008). *VLFeat: An Open and Portable Library of Computer Vision Algorithms*. http://www.vlfeat.org/.

Watt, A. H. and M. Watt (1992). *Advanced Animation and Rendering Techniques: Theory and practice*. Tech. rep. New York: Addison Wesley.

Wever, N., L. Schmid, A. Heilig, O. Eisen, C. Fierz, and M. Lehning (2015). "Verification of the multi-layer SNOWPACK model with different water transport schemes". In: *The Cryosphere* 9.6, pp. 2271–2293.

Wever, N., C. Vera Valero, and C. Fierz (2016). "Assessing wet snow avalanche activity using detailed physics based snowpack simulations". In: *Geophysical Research Letters* 43.11, pp. 5732–5740.

Winkler, K., B. Zweifel, C. Marty, and F. Techel (2019). "Schnee und Lawinen in den Schweizer Alpen. Hydrologisches Jahr 2017/2018". In: *WSL Berichte* 77, pp. 1–135. ISSN: 2296-3456.

Zweifel, B., C. Lucas, E. Hafner, F. Techel, C. Marty, and T. Stucki (2019). "Schnee und Lawinen in den Schweizer Alpen. Hydrologisches Jahr 2018/2019". In: *WSL Berichte* 86, pp. 1–134. ISSN: 2296-3456.

Zweifel, B., C. Pielmeier, C. Marty, and F. Techel (2017). "Schnee und Lawinen in den Schweizer Alpen. Hydrologisches Jahr 2016/2017". In: *WSL Berichte* 61, pp. 1–79. ISSN: 2296-3456.

Zweifel, B., C. Pielmeier, C. Marty, F. Techel, L. Stoffel, M. Ruesch, and Y. Bühler (2016). "Schnee und Lawinen in den Schweizer Alpen. Hydrologisches Jahr 2015/2016". In: *WSL Berichte* 51, pp. 1–99. ISSN: 2296-3456.

Declaration of consent

on the basis of Article 30 of the RSL Phil.-nat. 18

Name/First Name: Mäder, Flavia

Registration Number: 15-704-893

Study program: MSc in Climate Science with special qualification in Atmospheric Science

Bachelor ☐ Master ☑ Dissertation ☐

Title of the thesis: Detecting Avalanches: Linking Seasonal Dynamics of Snow-Covered Area to Wet-Snow Avalanche Activity

Supervisor: PD. Dr. Stefan Wunderle
Dr. Alec van Herwijnen

I declare herewith that this thesis is my own work and that I have not used any sources other than those stated. I have indicated the adoption of quotations as well as thoughts taken from other authors as such in the thesis. I am aware that the Senate pursuant to Article 36 paragraph 1 litera r of the University Act of 5 September, 1996 is authorized to revoke the title awarded on the basis of this thesis.
For the purposes of evaluation and verification of compliance with the declaration of originality and the regulations governing plagiarism, I hereby grant the University of Bern the right to process my personal data and to perform the acts of use this requires, in particular, to reproduce the written thesis and to store it permanently in a database, and to use said database, or to make said database available, to enable comparison with future theses submitted by others.

Place/Date

Davos, 28.10.2020

F. Mäder

Signature